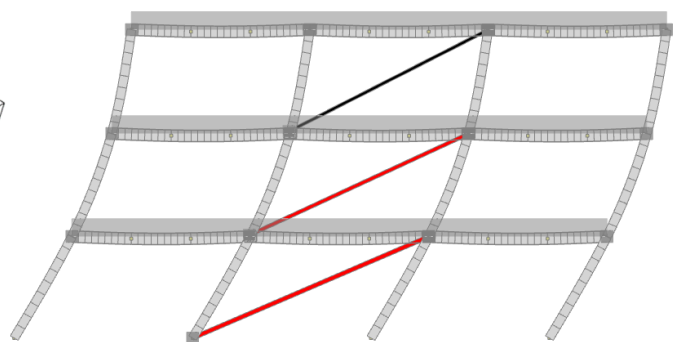
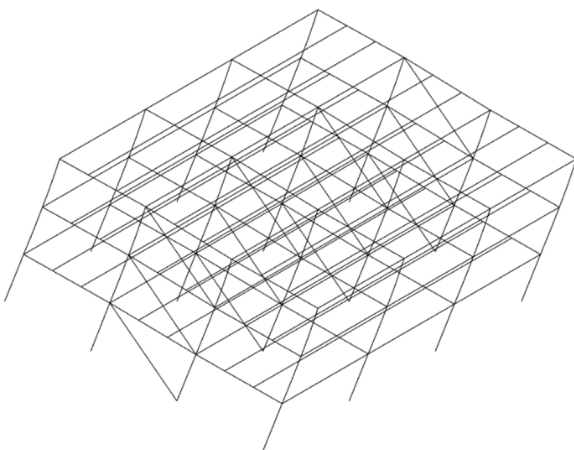
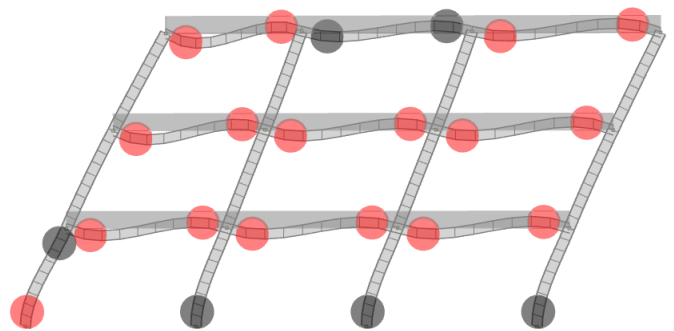
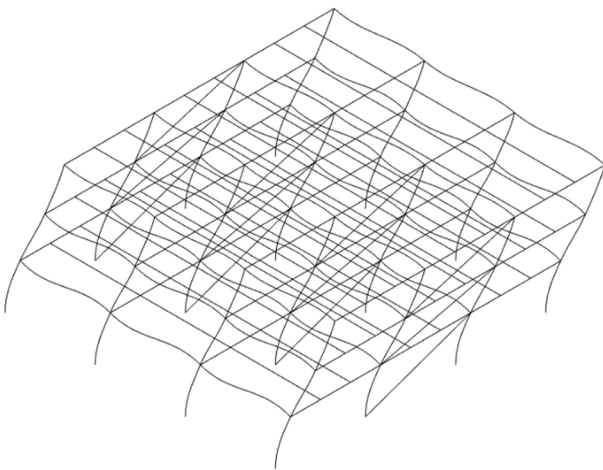


MASTER'S THESIS

Estimation of actuator parameters for a Reaction Wall through Pushover Analysis





Department of The Built Environment

Thomas Manns Vej 23

DK-9220 Aalborg Ø

www.build.aau.dk/

AALBORG UNIVERSITY

STUDENT REPORT

Title:

Master Thesis

Theme:

Seismic Analysis & Design

Thesis Period:

Spring Semester 2022

Author:

B.Eng., Boris Minkov

Supervisor, AAU:

Assoc. Prof. Lars Damkilde

Supervisor, External:

Assoc. Prof. Tzvetan Georgiev

Copies: 4

Pages: 163

Date of Completion:

09th of June 2022

Abstract:

A national seismic testing lab is to be built in Bulgaria. It will accommodate state of art seismic testing facilities one of which is a Reaction wall - Strong floor (RWSF). As a first step towards determining suitable actuators for it, an appropriate numerical simulation must be performed on a number of Prototypes made of different materials and composed of diverse lateral restraining systems (LRS).

As part of the Thesis, the Prototype is chosen as a steel structure composed of two different LRS in both orthogonal directions - Moment Resisting Frame (MRF) and Concentrically Braced Frame (CBF). A linear seismic analysis is then carried out using the Modal Response Spectrum Analysis (MRSA) on a spatial computational model in Autodesk Robot. A brief sensitivity study is performed for determining the most conservative response spectra based on EC8. Both LRS are designed following the Capacity Design concept. The obtained results are validated and discussed.

The SeismoStruct software is used to simulate a RWSF test by performing a planar non-linear static (Pushover) analysis on the MRF and CBF. The non-linear response is verified and the necessary parameters for choosing an actuator are provided. The results are discussed with focus on uncertainties and the steps that follow.

Preface

This report is created in relation to the final Master Thesis in the Master of Science program in Structural and Civil Engineering at Aalborg University (AAU). This is a short type of thesis which is worth 30 ECTS corresponding to 900 working hours distributed in the period between February 2022 and June 2022. The signed Thesis contract between all parties can be found in Appendix G.

Reading Guide

This document is formed of two parts:

- Report, the purpose of which is to guide the reader through the process of completing the project.
- Appendix, accompanying the Report and providing an in-depth explanation in form of additional description, formulae and supportive material.

An example of the way the Report (left) and Appendix (right) are structured is shown below:

I	Part		
1	Chapter	A	Chapter
1.1	Section	A.1	Section
1.1.1	Sub-section	A.1.1	Sub-section
Figure 1.1	Figure 1 in Section 1	Figure A.1	Figure 1 in Section A
Table 1.1	Table 1 in Section 1	Table A.1	Table 1 in Section A
(1.1)	Equation 1 in Section 1	(A.1)	Equation 1 in Section A

Each chapter begins with a small synopsis which summarizes its content. The references to the literature used in the report are provided using the Harvard-Method. If the project is wanted in paper form, it is recommended to print in color.



Boris Minkov
<bminko20@student.aau.dk>

Contents

Preface	5
Acknowledgment	5

I **Setting the scene**

1	Experimental seismic testing	11
1.1	Introduction	11
1.2	History	12
1.3	Facilities around the globe	12
1.4	Bulgaria's needs	14
1.5	Problem statement	14
2	Prototype	15
2.1	Introduction	15
2.2	Geometry	16
2.3	Sections and materials	18
2.4	Loads and actions	19
2.5	Load combinations	19
2.6	Structural systems and boundary conditions	20
2.6.1	Slab/diaphragm	21
2.6.2	Concentrically Braced Frame (CBF)	22
2.6.3	Moment Resisting Frame (MRF)	23

II **Preliminaries**

3	RWSF test methods	27
3.1	Introduction	27
3.2	Snap-back	28
3.3	Hybrid Testing	29
3.3.1	Pseudo dynamic (PsD)	29
3.3.2	Real time	30
3.3.3	Geographically distributed	30
3.4	Pushover	31

3.5	Conclusion	31
4	Seismic analysis & design methods	33
4.1	Introduction	33
4.2	Modal response spectrum (MRSa)	34
4.3	Pushover analysis (PA)	35
4.4	Earthquake design	36
4.4.1	Capacity design and influence of behaviour factor	37

III**Prototype Linear Analysis & Design**

5	Modal Response Spectrum Analysis	41
5.1	Introduction	41
5.2	Linear computational model	42
5.3	Modal analysis parameters	43
5.4	Response spectrum	44
5.4.1	Behaviour factor	44
5.4.2	Design ground acceleration	45
5.4.3	Sensitivity study: ground and spectra types	46
5.4.4	Conclusion	47
5.5	EC8 criteria and output quality assurance	48
5.5.1	Eigenperiods, mass participation and mode shapes	48
5.5.2	Torsional effects	50
5.5.3	Base shear	51
5.5.4	Displacements	52
5.5.5	Damage limitation	53
5.5.6	Second order effects	54
5.5.7	Buckling analysis of columns	55
6	Capacity design	57
6.1	CBF	57
6.1.1	Diagonals	58
6.1.2	Beams & columns	60
6.2	MRF	61
6.2.1	Beams	61
6.2.2	Columns & connections	65
7	Seismic design situation	71
7.1	Seismic load cases and combinations	71
7.1.1	Load cases	71
7.1.2	Load combinations: dissipative elements	72

7.1.3	Load combinations: non-dissipative elements	73
7.2	Member capacity check (ULS+SLS)	74
7.3	Conclusion	76

IV **Prototype response assessment through Pushover analysis**

8	Pushover analysis	79
8.1	Introduction	79
8.2	Non-linear computational models	80
8.2.1	Boundary conditions	81
8.2.2	Element types	82
8.2.3	Model verification	83
8.3	Constitutive model	84
8.4	Loads and mass	86
8.4.1	Mass definition	86
8.4.2	Vertical (gravity) load	87
8.4.3	Lateral (incremental) load	88
9	Non-linear response	89
9.1	Preliminaries	89
9.1.1	Choice of control node	89
9.1.2	Choice of criteria	90
9.1.3	Choice of lateral load distribution	91
9.2	MRF pushover curve	92
9.2.1	Yield stages	93
9.2.2	Fracture stages	94
9.3	CBF pushover curve	95
9.3.1	Yield and fracture stages	96
9.4	Conclusion	97
10	Discussion	101
	Bibliography	111

V **Appendix**

A	Prototype	115
A.1	Steel properties	115
A.1.1	Linear constitutive model	115
A.1.2	Non-linear constitutive model	115

A.2	Characteristic loads and actions	116
A.2.1	Trapezoidal sheet HI-BOND A55/P600	116
A.2.2	Permanent loads - kG	118
A.2.3	Imposed loads - kQ	120
A.2.4	Variable actions - kS1	121
B	Linear computational model	123
B.1	Member and node numbers	123
B.2	Member definition - design parameters	126
B.3	Load cases and combinations	128
B.4	Quality assurance (QA)	129
C	Non-linear computational model	135
C.1	Member and node numbers	135
C.2	Vertical (gravity) loads	137
C.2.1	MRF	137
C.2.2	CBF	137
C.3	Lateral (incremental) loads	138
C.3.1	MRF	138
C.3.2	CBF	139
C.4	Quality assurance (QA)	140
D	Modal Response Spectrum Analysis	141
D.1	Theory	141
D.1.1	Forming of a response spectrum	141
D.1.2	Modal combination rules	141
D.1.3	EN1998-1 [2004] response spectrum	143
D.2	Basic period check using the Rayleigh quotient	146
D.3	Sensitivity study: choice of response spectrum	147
D.4	Base shear quality assurance	149
D.5	Prototype sensitivity to second order effects	150
D.6	Prototype damage limitation	150
E	Pushover analysis	151
E.1	Theory	151
F	Prototype Capacity Design	155
F.1	CBF	155
F.1.1	General	155
F.1.2	Calculation	156
F.2	MRF	157
F.2.1	General	157

F.2.2	Beam plastic capacity	158
F.2.3	Beam segment lateral stability	159
F.2.4	SCWB concept	159
F.2.5	Column plastic shear capacity	159
F.2.6	Panel zone	160
F.2.7	Column verification	160
G	Thesis contract	161

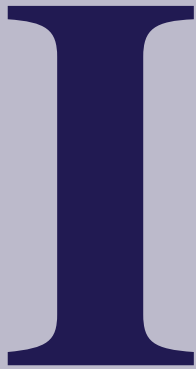
Acknowledgement

The preparation for my Master Thesis started more than a year ago during a practical placement in the Bulgarian consultancy company - Ircon where I built a strong foundation on Earthquake Engineering without which this work would not be possible. I would therefore want to thank once again the entire structural engineering department of Ircon for their time and contribution during my six months there.

I want to express my deep gratitude to Ircon's manager, Associate Professor in the Steel structures Division at UASG and company supervisor - Assoc. Prof. Tzvetan Georgiev. His guidance and support helped me move in the right direction and bring sense of the confusion I was sometimes in. I would also like to express my special gratitude to Assoc. Prof. Lars Damkilde for his committed supervision from AAU side during the last one year of my MSc degree. I believe that his unorthodox teaching methods and approach helped me improve significantly my research and learning style. I am very thankful to the responsible for ELSA Reaction Wall - PhD. Pierre Pegon for the short but very constructive and valuable conversations I had with him.

I wish to thank to my family and close friends for the support and motivation especially during the last 2 months of my Thesis.

Last but not least I would like to extend my acknowledgement to all my Professors and teachers who guided and helped me reach this consecrate point in my education. It is with great sense of appreciation I wish to specially thank Prof. Pauli Andreasen for his dedicated approach to Structural Engineering and the influence he had on me during my Bachelor's degree in VIAUC.



Setting the scene

1	Experimental seismic testing	11
1.1	Introduction	
1.2	History	
1.3	Facilities around the globe	
1.4	Bulgaria's needs	
1.5	Problem statement	
2	Prototype	15
2.1	Introduction	
2.2	Geometry	
2.3	Sections and materials	
2.4	Loads and actions	
2.5	Load combinations	
2.6	Structural systems and boundary conditions	

1 Experimental seismic testing

The content in this chapter is meant to introduce the reader to what the different facilities used for experimental seismic testing are and where the biggest of them are located worldwide. Bulgaria's need for such a facility is briefly discussed after which the Thesis's problem statement is formed.

1.1 Introduction

The main challenge with seismic testing (similar to other experimental studies) is the scaling factor which greatly impacts the structural response especially when dynamics are involved. Therefore, it is understandable that experimental testing facilities grow in size with an aim of accommodating as large as possible test specimens (prototypes). Furthermore, a growing amount of consulting companies prefer to experimentally verify their numerical results on complex infrastructures such as bridges. The two most common facility types used for experimental seismic testing are briefly described below:

- **Reaction Wall Strong Floor (RWSF)**

The reaction wall and strong floor are typically one structural system. The RWSF can be L shaped (figure 1.1), rectangular or modular (re-configurable). Actuators which are anchored to the wall gradually apply a load in very small increments on the prototype structure. This is why this facility is used mainly for pseudo-dynamic testing (more is discussed in Chapter 3). It however allows for testing of large structures without scaling them down.

- **Shake table**

A platform which is moved by actuators in up to its 6 DOF (see figure 1.2). This facility allows for a fully dynamic seismic testing, simulation of accelerogram in real time, etc. The main drawback of the shake tables is that the test specimens are very often scaled down.

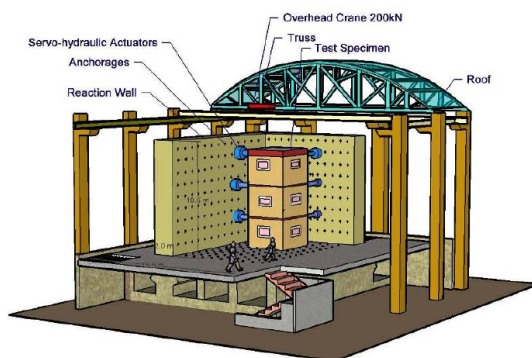


Figure 1.1: RWSF concept at IIT Kanpur, India [Rai et al., 2014]

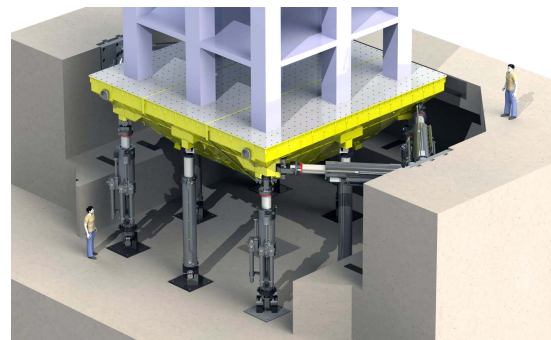


Figure 1.2: 6 DOF shaking table concept Illustration courtesy of MTS.

1.2 History

Earthquakes has always been one of the most destructive natural phenomenon known to humankind. Peru is known for being a highly seismic part of the world where people have adapted their structures to resist earthquakes through trial and error. The ancient Peruvian civilization has found that using dry-stone construction created more seismic resistant structure instead of using mortar. It is visible in figure 1.3 how the Incas cut the stones to perfection so that they can tightly fit and create what is known today as a shear wall.



Figure 1.3: Dry-stone walls of Machu Picchu, Peru

Today the seismic performance assessment in a laboratory has replaced (thank god) the ancient trial and error approach used by our ancestors. It is well established methodology to calibrate predictive models and analytical formulas from experimental data since numerical studies have their limitations. This methodology is used for developing of modern seismic codes such as EN1998-1 [2004]. Moreover, developing novel structural solutions require experimental validations in order to ensure their safety.

In the last decades considerable advances have been achieved in the Earthquake Engineering (EE) field. The research results have contributed to the preparation of modern design codes, to the identification of several problems in the existing structures and to innovative solutions for the structural assessment. [Marazzi et al., 2011]

1.3 Facilities around the globe

Some of the major labs for seismic performance assessment are shown in tables 1.1 and 1.2 on the following page with figures 1.4 and 1.5 illustrating the largest of them.

As seen in table 1.1 the capabilities of a shaking table are most often expressed using its dimensions, maximum acceleration and shaking frequency it can provide. Other parameters are the maximum velocity in the different DOF measured in mm/s, the available DOF and the maximum weight it can accommodate.

Table 1.1: Major shaking tables around the world

Country	Name	Dimensions [mxm]	Max. acceleration [g]	Max. frequency [Hz]
USA	University of Nevada at Reno	4.3 x 4.5	1.0	50
USA	University of California at San Diego	7.6 x 12.2	1.0	20
Japan	E-Defense	20.0 x 15.0	1.5	50
China	Tongji University in Shanghai	4.0 x 6.0	1.5	50
Portugal	LNEC	-	6.0	-

As seen in table 1.2, the two most important parameters for a RWSF facility are the maximum force it can apply on a prototype (actuator capacity) and the maximum distance it can push it (actuator stroke). Its shape (U, L, rectangular), dimensions (especially height), RW and SF capacity are also important factors.

Table 1.2: RWSF around the world

Country	Name	Max height [m]	Actuator capacity [kN]	Actuator stroke [m]
Japan	Building Research Institute (BRI)	25.0	1000	±0,5
Taiwan	NCREE	15.0	1000	±0,25 to ±0,5
Italy	ELSA	16.0	3000	±0,25 to ±0,5
US	NEES, Leigh University	15.2	2000	±0,5
India	IIT Kanpur	10.5	-	-
Greece	NTUA	6.0	500	-



Figure 1.4: ELSA RWSF in Italy [GA et al., 2014]



Figure 1.5: E-Defence shake table in Japan. Photo courtesy of Bosai.

1.4 Bulgaria's needs

Bulgaria is located on the Balkan Peninsula which is one of the most geodynamically active parts not only in Europe but the whole world. It is understandable why a lot of resources has been invested throughout the years for R&D in the Seismic Engineering field. The University of Architecture, Civil Engineering and Geodesy (UASG) in Sofia, Bulgaria has been a place where a big part of the R&D has taken place not only on national but also on international levels. An example of this is the EQUALJOINTS+ EU project with an aim of developing standardized seismically qualified joints according to EN1998-1 [2004] [Landolfo, 2022] (see also figure 1.6).

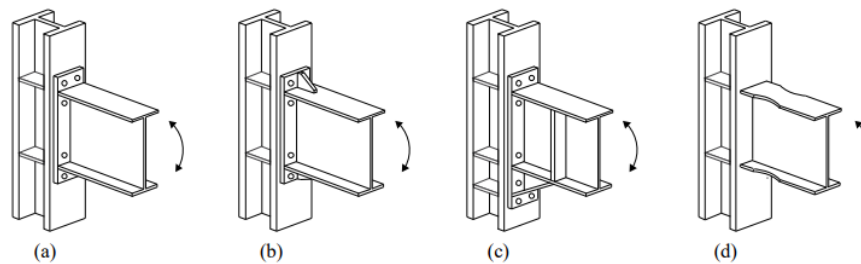


Figure 1.6: Beam-to-column joints prequalified in the framework of EQUALJOINTS project: a) Bolted hunched joint b) Bolted extended stiffened end-plate joint c) Bolted extended unstiffened end-plate joint d) Welded dog-bone joint [ECCS, 2018]

An advanced seismic testing facility in Bulgaria is not only a good idea but rather a necessity if the country wants to remain part of the international seismic R&D projects and community. Moreover, this would represent a substantial advantage for the Seismic Engineering students in UASG since it will impact the learning process by promoting and motivating the work in this field.

A project for seismic testing facility is currently being developed where both a large scale RWSF and a shaking table are planned. Once the facility is completed it will become the largest of its kind on the Balkan Peninsula. Currently the National Technical University of Athens hold this title (see table 1.2). For confidentiality purposes more information on the project (drawings, location, etc.) cannot be shared.

1.5 Problem statement

The following problem formulation is stated below:

Problem formulation

Choose, analyze & design an appropriate Prototype from steel. Perform a suitable numerical simulation and find the necessary actuator capacity and stroke to accommodate it in the new RWSF facility.

The following is not part of the problem formulation

- The choice of the actual actuators (product).
- The detail design of joints
- Investigation of soil-structure interaction
- Experimental validations and studies

2 Prototype

A prototype is defined as the structure which is analyzed, designed and assessed as part of answering the problem stated in section 1.5. The aim of this chapter is to introduce the reader to the chosen structure for the Prototype. The choice of structural systems, loads and materials are all discussed in details. Preliminary drawings/sketches of the structural joints are proposed.

2.1 Introduction

Before choosing the Prototype structure and its lateral restraining systems (LRS) a number of consultation were made with Phd. Pierre Pegon (responsible for the largest RWSF facility in Europe - ELSA) and Assoc. Prof. Tzvetan Georgiev (Company Supervisor and Professor in the Steel Structures Division at UASG).

"...you have to deal with various scenario...You do not want to overestimate your needs, but at the same time you would like to be prepared for the future!" -Pierre Pegon

Taking into consideration this feedback, it was decided to incorporate the two most common steel lateral restraining systems (LRS) in the Prototype structure or namely the Concentrically Braced Frame (CBF) and Moment Resisting Frame (MRF) - see figure 2.2. Having different LRS in each orthogonal direction will yield more diverse results as their load-deflection characteristics are different. It should be noted that the more scenarios for materials and LRS types are investigated - the more diverse results will be obtained which will help choosing a suitable actuator for the RWSF facility.

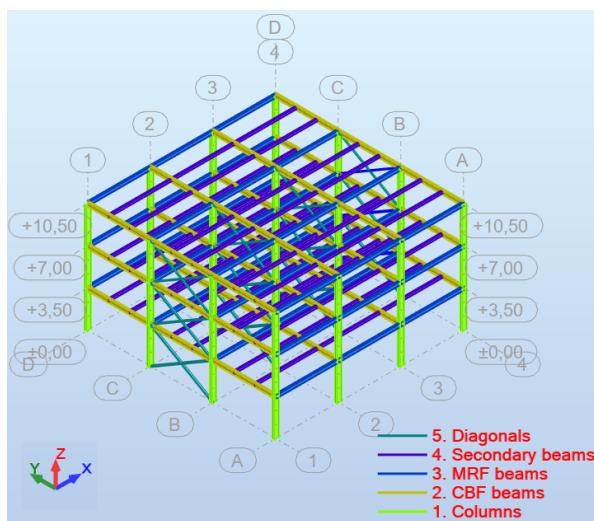


Figure 2.1: Members by type

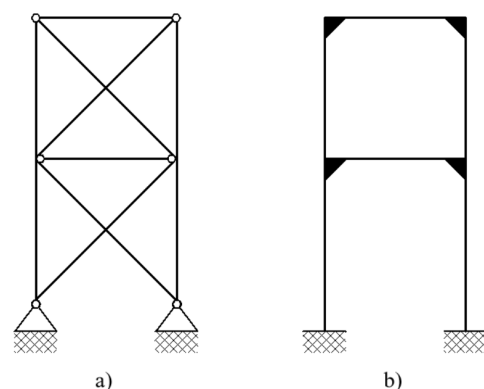


Figure 2.2: Investigated LRS: a) CBF b) MRF

2.2 Geometry

The prototype structure is chosen to be regular in height and elevation so as not to introduce torsional effects which would unnecessarily complicate a future experiment on it. It is part of a three storey 10.5 m high steel office building with an inter-storey height of 3.5 m. It is composed of three 6 m bays in both longitudinal x and transverse y directions as shown in figure 2.3 below.

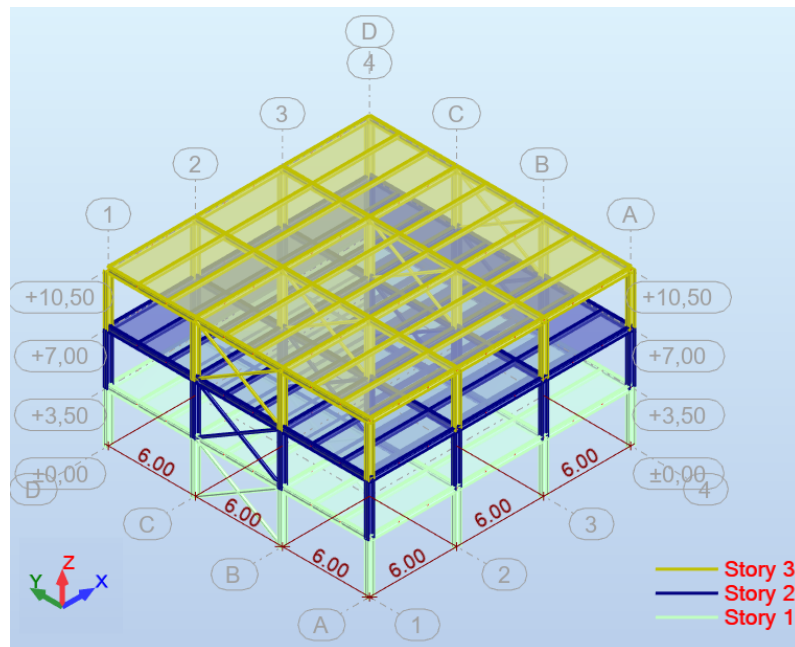


Figure 2.3: Stories and dimensions

The dimensions of the prototype structure are in accordance with the size of the future RWSF facility. The XZ and YZ elevation can be seen in figures 2.5 and 2.6. A plan view is provided in figure 2.4.

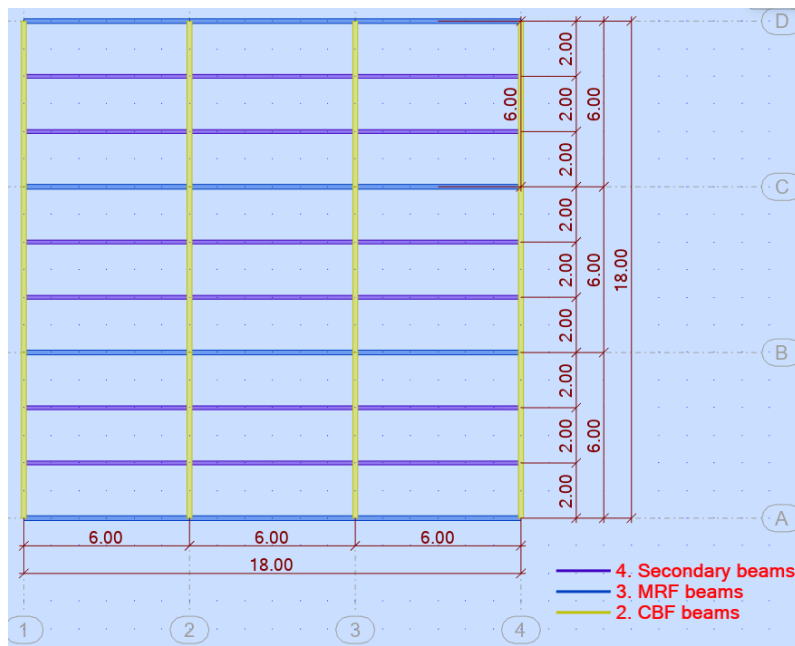


Figure 2.4: Plan in XY plane

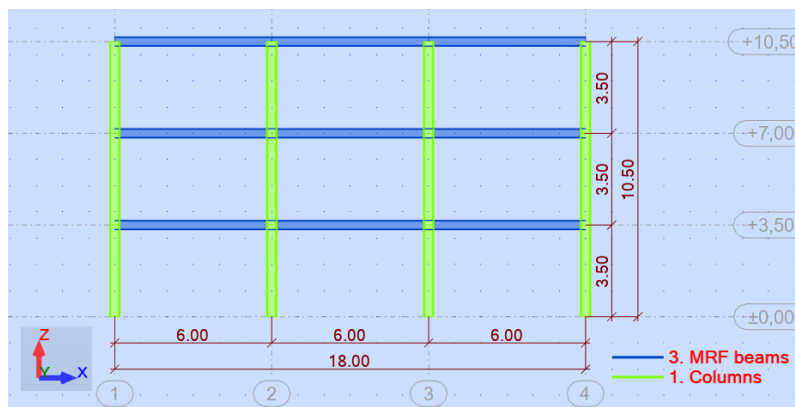


Figure 2.5: Elevation in XZ plane

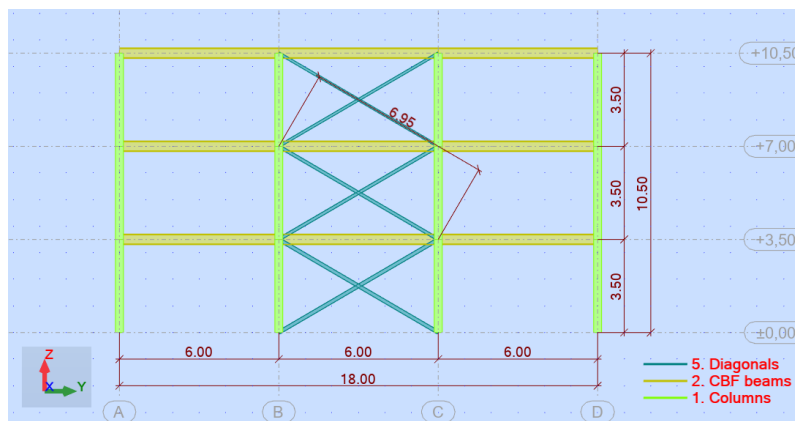


Figure 2.6: Elevation in YZ plane

2.3 Sections and materials

The materials and steel sections are shown in table 2.1 and figure 2.7 below. The corresponding steel properties can be seen in Appendix A.1. Please note that different properties are used for the linear and non-linear constitutive models (see later in section 8.3).

Table 2.1: Used sections and materials by member type

Member type	Section	Material according to EC
Columns	HEB 400	S460 N/NL
Diagonals (storey 3)	CF SHS 100x3	S235 JR
Diagonals (storey 2)	CF SHS 120x4	S235 JR
Diagonals (storey 1)	CF SHS 140x4	S235 JR
Secondary beams	IPE 270	S275 JR
MRF beams	IPE 360	S275 JR
CBF beams	IPE 400	S275 JR

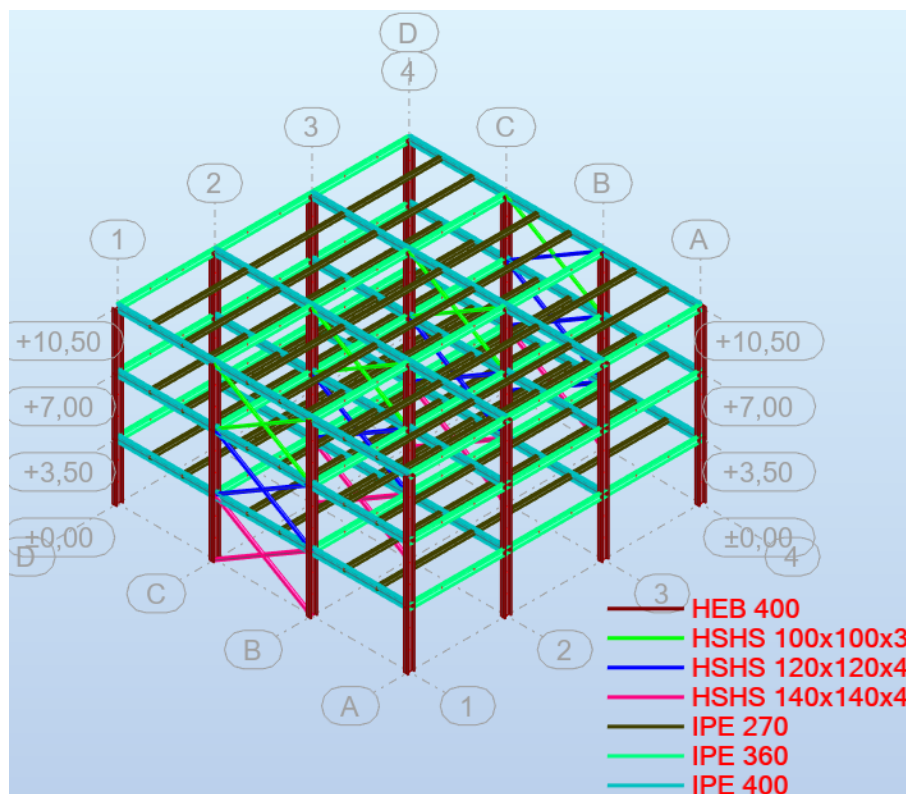


Figure 2.7: Used sections

The shown steel sections and materials are later verified with the linear analysis and design in part III of this report.

2.4 Loads and actions

The applied loads and actions are discussed in detail with the company supervisor. This includes conservative but realistic assumptions for their values and positioning. The non-seismic (vertical) load cases are defined in table 2.2 below with reference to the corresponding tables in Appendix A.2 where the values can be found.

Table 2.2: Non-seismic load cases as defined in Autodesk Robot [2021]

Number	Name	Load origin	Reference
1	kG1/struct/	steel elements and slab/diaphragm	tables A.3 and A.4
2	kG2/roof/	roof structure	table A.5
3	kG3/floor/	floor and ceiling structure	table A.6
4	kG4/wall/	external wall cladding	table A.7
21	kS1/snow/	snow on the roof	table A.10
22	kQ1/live/	imposed load on the roof	table A.8
23	kQ2/live/	imposed load on the floors	table A.9

- **Permanent loads kG** include the structural and non-structural elements.
- **Variable actions kS1** of which only snow is considered. Wind actions are neglected assuming that seismic actions are dominant.
- **Imposed loads kQ** for the corresponding building category chosen for the prototype - office,

The seismic actions are applied as equivalent static forces using the Modal Response Spectrum Method (MRSA) as described in section 4.2. This includes performing a sensitivity study in section 5.4 for finding the most conservative spectra for the Prototype structure. The derived seismic load cases are shown in subsection 7.1.1.

2.5 Load combinations

The SLS and ULS load combinations are defined according to EN1990 [2007] and can be seen in Appendix B.3. Please note that the seismic load combinations are shown separately in subsections 7.1.2 and 7.1.3. The SLS criteria for the different members are defined in table 2.3 below where L is their length/height.

Table 2.3: Defined SLS criteria for the members

Member	Criteria	
Beam/slab	Maximum vertical deformation (final)	$L/200$
Beam/slab	Maximum vertical deformation (imposed loads)	$L/250$
Column	Maximum nodal displacement	$L/150$

The maximum design vertical load on the slab used to choose a trapezoidal sheet product in subsection 2.6.1 is calculated in (2.1) below

$$q_d = 1.35kG1 + 1.35kG3 + 1.50kQ2 = 13.30 \text{ kN/m}^2 \quad (2.1)$$

2.6 Structural systems and boundary conditions

The Prototype's structural systems alongside with the boundary conditions (BC) are summarized in figure 2.8 below. The following subsections contain detailed description of each system and the design measurements undertaken to ensure the chosen BC for the three main structural systems:

- Slab/diaphragm - subsection 2.6.1
- Concentrically Braced Frame (CBF) - subsection 2.6.2
- Moment Resisting Frame (MRF) - subsection 2.6.3

Please note that the proposed design solutions are only supported with preliminary drawings/sketches since the detailed design is not part of the Thesis's delimitation.

The member definition parameters (example: buckling length) are shown in Appendix B.2 as defined in Autodesk Robot [2021]. Their definition is based on the boundary conditions and design choices discussed in the following sub sections.

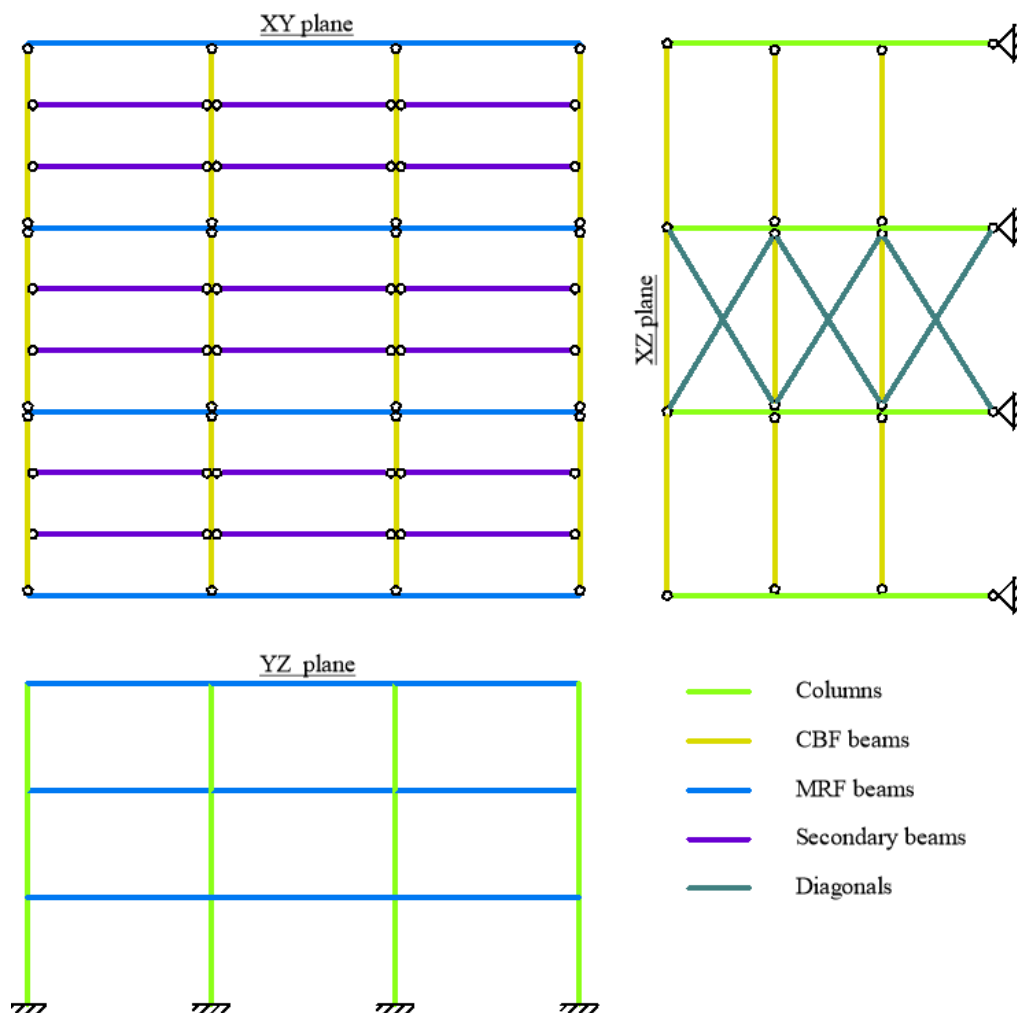


Figure 2.8: Structural systems in 2 elevations and 1 plan

2.6.1 Slab/diaphragm

The slab/diaphragm of the prototype is made of a composite deck formed from structural trapezoidal sheeting filled with reinforced concrete as shown in figure 2.9. This is a widely used solution for steel structures since it is cost effective, simple to execute and it provides excellent diaphragm behaviour in both orthogonal direction. Moreover, after a brief research it was found that a similar solution was used in an seismic experiment performed at ELSA's RWSF facility [GA et al., 2014]. The TYPE A55/P600 trapezoidal sheeting solution by METECNO [1961] is chosen. Its properties and load bearing capacity can be found in Appendix A.2.1.

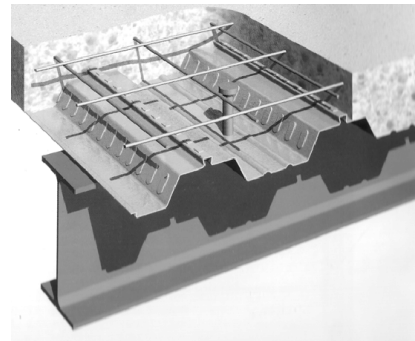


Figure 2.9: Composite slab made of trapezoidal sheeting and reinforced concrete [Ganesh et al., 2005]

A reinforced concrete slab of $t = 95$ mm made of C25/30 concrete is casted on top of the 55 mm high TYPE A55/P600 steel sheeting driving the total slab thickness of $t = 150$ mm as shown in figure 2.11. The maximum design vertical load on the trapezoidal sheet has been calculated to $q_d = 13.30 \text{ kN/m}^2$ in (2.1). TYPE A55/P600 with $t = 1.2$ mm is able to withstand a load of 13.54 kN/m^2 with a deflection less than $L/200$ (in agreement with table 2.3). The solution is illustrated in figure 2.11 and can be seen in details in Appendix A.2.1.

As seen from figures 2.11 and 2.10, the slab is spanning in one direction and supported on the secondary and MRF beams. The secondary beams are hinged to the CBF beams. In this way only $1/3$ of the vertical load is transferred to the MRF beams and the remaining $2/3$ go to the CBF beams. The load distribution is done in this way so as not to overload the dissipative MRF beams with vertical load but rather have a leading lateral (seismic) combination for their design which is a more economic solution.

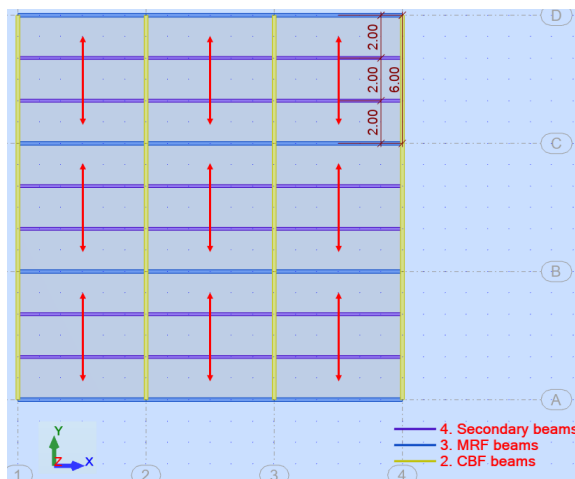


Figure 2.10: Floor plan with slab span

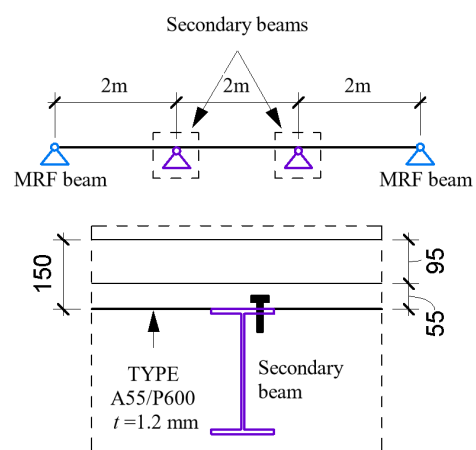


Figure 2.11: Chosen solution for supporting the slab on the prototype structure

2.6.2 Concentrically Braced Frame (CBF)

The lateral stabilizing system in y -direction is formed of four identical CBFs as shown in figure 2.12. An elevation view is provided in figure 2.13 where the connection details are visible. Please note that figure 2.14 is a preliminary sketch used for demonstrating the used connection concept - the joints design is not in the thesis's scope.

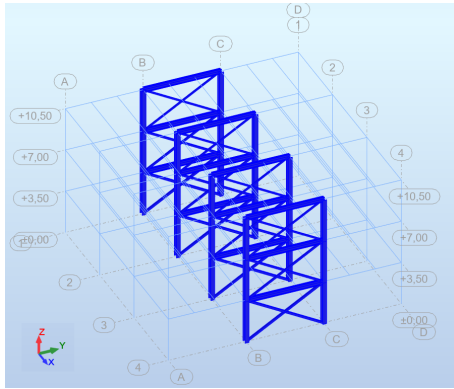


Figure 2.12: CBF in transverse y direction

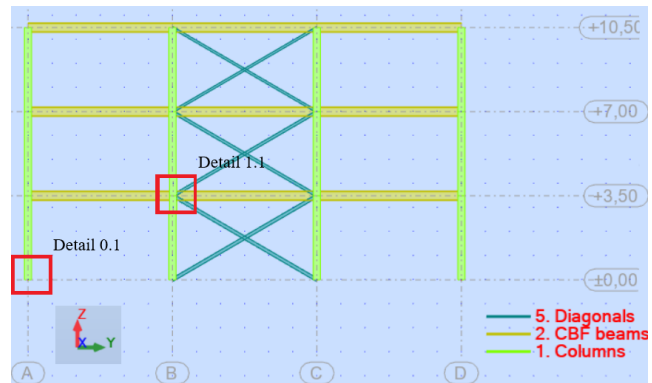


Figure 2.13: Elevation, YZ plane, structure axis 1

Each beam-column connection is hinged (moment released) leading to the CBF cores (marked in figure 2.12) becoming the stiffest system in the lateral y direction. This means that the largest amount of lateral force is accumulated in the diagonals which is desired as they are later designed as dissipative elements. Figure 2.14 illustrates a proposed connection design concept where a low rotational stiffness is provided by using a bolted joint between the CBF beam and column. A traditional gusset plate connection is used for connecting the diagonal struts and CBF beam to the column with an emphasis on the center-lines of all elements meeting in one point.

The base of the columns are moment released around x (released M_x) i.e. they are considered as pinned in the direction of the CBF. In this way the development of the plastic mechanism in the CBF is easier to control. In practice this is done by reducing the width of the base plate and keeping a minimal y distance between the bolts as shown in figure 2.14.

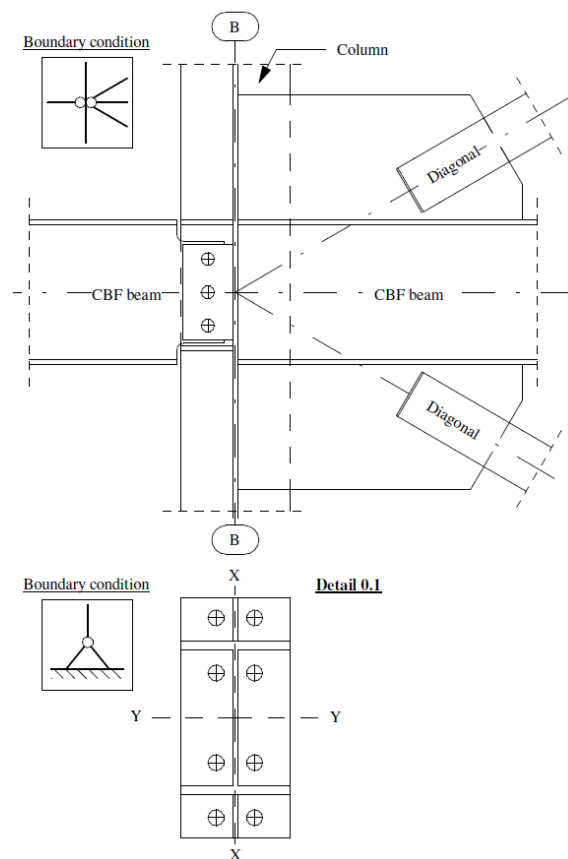


Figure 2.14: Connection concept for detail 1.1 and 0.1 with shown boundary conditions

2.6.3 Moment Resisting Frame (MRF)

The structure is stabilized laterally by the four MRF provided in the x -direction as shown in figure 2.15. An elevation view is provided in figure 2.16 where the connection details are visible. Please note that figure 2.17 is a preliminary sketch used for demonstrating the used connection concept - the joints design is not in the thesis's scope.

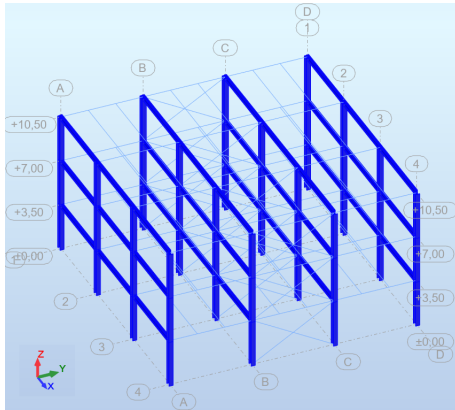


Figure 2.15: MRF in longitudinal x direction

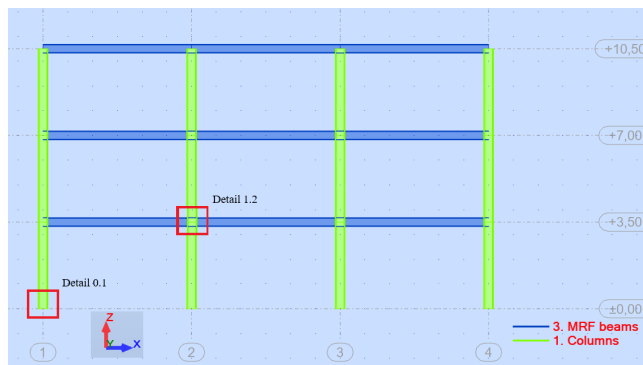


Figure 2.16: Elevation, XZ plane, structure axis A

As seen in figure 2.17, the MRF beams are fixed to the columns by means of a welded connection. A compressible material with a width of minimum 25 mm must be placed between the slab and column in order to avoid the contact point between steel and concrete. Moreover, shear connectors (struts) are provided between the slab and the top flange of the MRF beam which restrict the in-plane movement of the diaphragm. Note that this connection detail is further examined in subsection 6.2.1.

The base of the columns is provided with a fixed support (M_y moment is fixed). For this purpose the rotational stiffness around y is increased by adding a longitudinal stiffener at the base plate by naturally continuing the column's web.

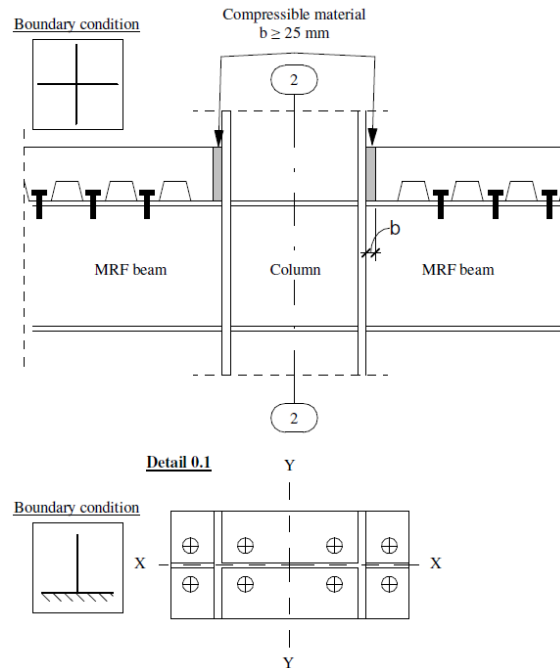


Figure 2.17: Connection concept for detail 1.2 and 0.1 with shown boundary conditions

II

Preliminaries

3	RWSF test methods	27
3.1	Introduction	
3.2	Snap-back	
3.3	Hybrid Testing	
3.4	Pushover	
3.5	Conclusion	
4	Seismic analysis & design methods	33
4.1	Introduction	
4.2	Modal response spectrum (MRSA)	
4.3	Pushover analysis (PA)	
4.4	Earthquake design	

3 RWSF test methods

The aim of this chapter is to present the most common test methods performed on a RWSF facility. Each of them is briefly discussed after which the chapter is concluded with the most suitable one that can be reproduced by a numerical simulation

3.1 Introduction

As previously mentioned, one of the substantial advantage of the RWSF facility is the possibility to test large specimens without scaling them down. This, combined with the flexibility and the wide range of test offered by a RWSF facility is often the reason for choosing it instead of a shake table.

To show the possibilities of a RWSF test simulation, the results from DUAREM: Full-scale experimental validation of **DUAL** eccentrically braced frame with **REMO**vable links performed at ELSA's RWSF facility (see table 1.2) are used as an example in the subsections to follow - see figure 3.1.



Figure 3.1: Cover page of DUAREM report [GA et al., 2014]

3.2 Snap-back

Almost all experimental studies on a RWSF begin with this type of test since it provides vital response parameters of a specimen such as its natural frequency.

Actuators pull, with an increasing force, a tension bar which is attached to the prototype structure. At a given point the bar fractures (snaps) which results in an instant release of energy causing the structure to freely vibrate. Example for the set up of a snap-back test is shown in figure 3.2 on the right where the tension bar can be seen marked with a red circle.

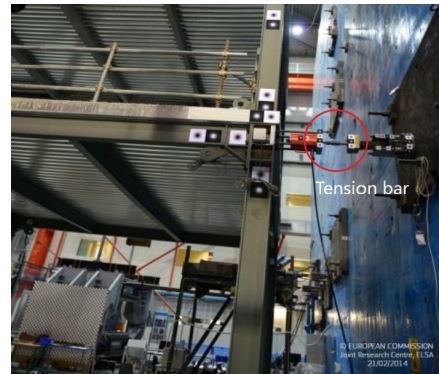


Figure 3.2: Snap-back test set up. Example from DUAREM [GA et al., 2014]

Figures 3.3 and 3.4 below illustrate the obtained output from DUAREM snap-back test (figure 3.2). The results provide a number of important response parameters of the specimen which can be used to obtain the damping of the structure, acquire the modal frequencies, identify the main vibration modes, etc. This test method can also be utilized to apply an appropriate range of force which will cause only the dissipative structural elements to yield.

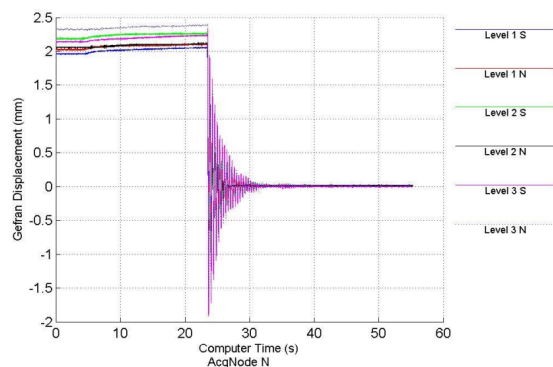


Figure 3.3: Displacement time-history of a snap-back test. Example from DUAREM [GA et al., 2014]

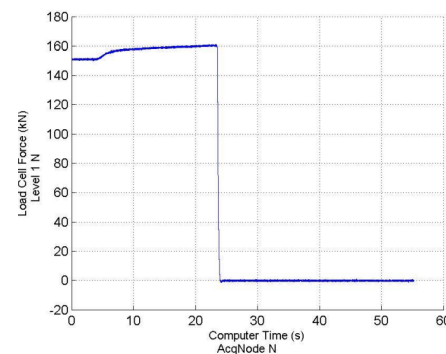


Figure 3.4: Load function time-history of a snap-back test. Example from DUAREM [GA et al., 2014]

3.3 Hybrid Testing

Hybrid testing (HT) is defined as one that uses a combination of numerical simulations and experimental results to obtain the structural response. The different HT methods possible on a RWSF facility depend on their execution time and location and are discussed in the following subsections.

According to Marazzi et al. [2011]: *Specimen can be limited to a small substructure (the part that is difficult to model numerically) and the remaining restoring and inertial forces can be simulated numerically in the equation of motion.* This means that for example, the part of a large bridge that is difficult to accurately simulate numerically can first be experimentally tested. The test results can then be used in a numerical model to simulate more precisely the non-linear behavior of the bridge structure.

3.3.1 Pseudo dynamic (PsD)

The PsD test is a hybrid method for which the forces are applied quasi-statically (very slow). Figure 3.5 shows an example of numerical integration of a discrete equation of motion containing a theoretical mass matrix M and seismic-equivalent external loads F but with a physical model for the restoring forces R . This is rather smart since R is hard to compute numerically when the structure is within its inelastic range and influenced by material non-linearity. The physical model can thus be reliably utilized to obtain the restoring force vector and fed back into the equation to solve it numerically. The steps for performing a PsD test (figure 3.5) are briefly discussed below.

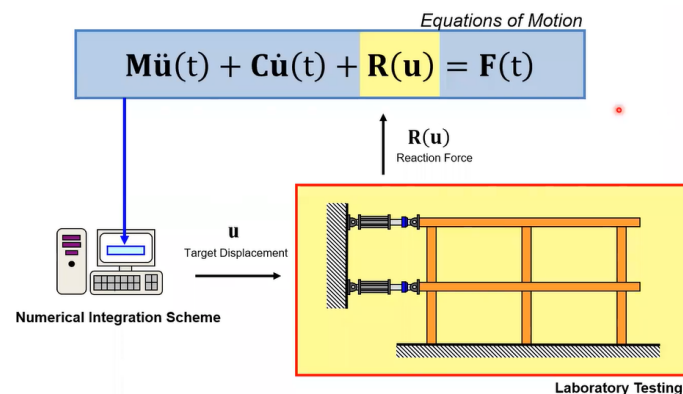


Figure 3.5: Hybrid testing principle: PsD MECHS [2018]

1. For each time-discrete state of an accelerogram, a target displacement u is computed from the numerical model and applied to the physical one by means of actuators.
2. Load cells are used to record the structural response (in form of $R(u)$) and fed back to the numerical model where the equation of motion can be solved since the inertial forces $F(t)$ are simulated numerically. In this way the non-linear and inelastic behaviour of the structure is captured more accurately.
3. The process is repeated for every time-discrete state of the chosen accelerogram. The time it takes to run the test depends on how the accelerogram is scaled and it may range from 1 to 5 hours until it has been completely simulated. Since the experiment is much longer than in real time, the simulation is controlled more accurately, non-desirable results are easily avoided and the necessary hydraulic power for the actuators can be reduced. The response is then plotted using the time of the original accelerogram as shown in figure 3.6.

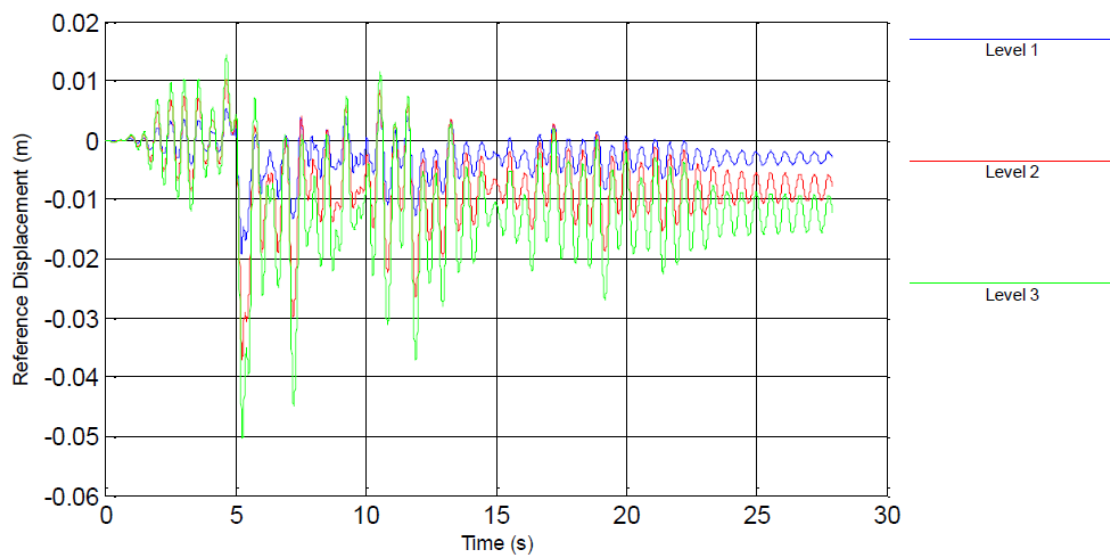


Figure 3.6: ULS equivalent PsD test - reference displacements at each storey plotted for the time of the original accelerogram. Example from DUAREM [GA et al., 2014]

3.3.2 Real time

The real time (also called fast) is a hybrid test during which an accelerogram is simulated in real time. It usually takes from a couple of seconds to minutes. According to Marazzi et al. [2011], this test is associated with many difficulties and are feasible only for relatively simple tests. Some of the problem include, amongst all:

- Time delay and response time of actuators
- Influence of measurement noise on the control action
- Short required computation time implying that numerical substructures with only a few degrees of freedom can be considered since the computation must be done in real time. Alternatively, special computational techniques should be adopted to increase computational efficiency.

3.3.3 Geographically distributed

This type of hybrid testing involves coupling of numerical or physical models in different laboratories while simultaneously performing an experiment. This testing technique is fairly new and used rarely but continuous research is being done on the topic. The main difficulties are connected with the high demand in networking technology and the lack of collaboration standards.

European seismic engineering research suffers from extreme fragmentation of research infrastructures (RI) between countries and limited access to them by the S/T community of earthquake engineering, especially that of Europe's most seismic regions. [SERIES, 2013]

The method has the potential to further develop the international collaboration and strengthen the relations between laboratories. Countries that cannot meet their testing needs with the experimental infrastructure they currently own would benefit the most out of this test type.

3.4 Pushover

The pushover is both a RWSF testing method and a non-linear static analysis type (section 4.3). Actuators push the test specimen with a certain speed most often measured in mm/min (i.e. displacement control) in order to avoid torsional effects that would otherwise alter the structural response. One of the main purposes of this type of experiment is to bring the prototype to its failure state and determine its plastic mechanism. Since the objective of the pushover analysis is precisely the same, numerical and experimental results can be easily compared - formation and location of plastic hinges, maximum roof displacements, damage limitations, capacity curves, etc. (see figure 3.7)

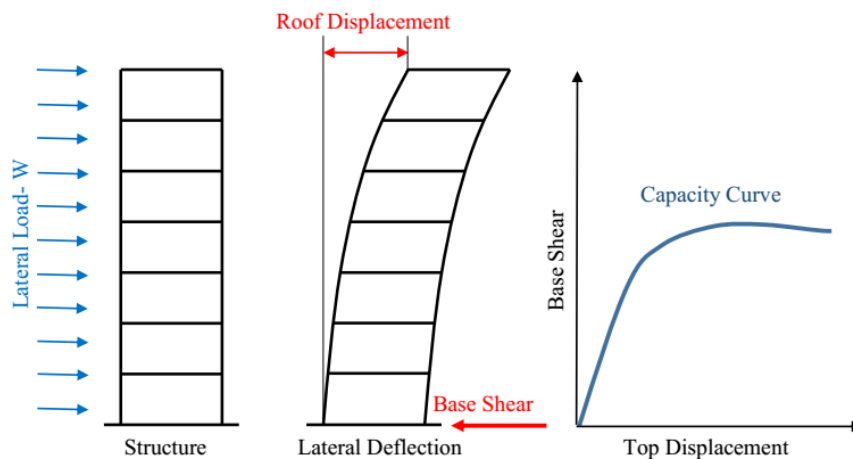


Figure 3.7: Pushover analysis: Capacity Curve [Marabi, 2016]

A test example is shown in figure 3.8 below. It can be seen that it takes different frame shear force (x -axis) for both frames to achieve similar frame drift displacement (y -axis). This shows the importance of performing the test in displacement control if the lateral stabilizing systems (S and N) have different properties (stiffness).

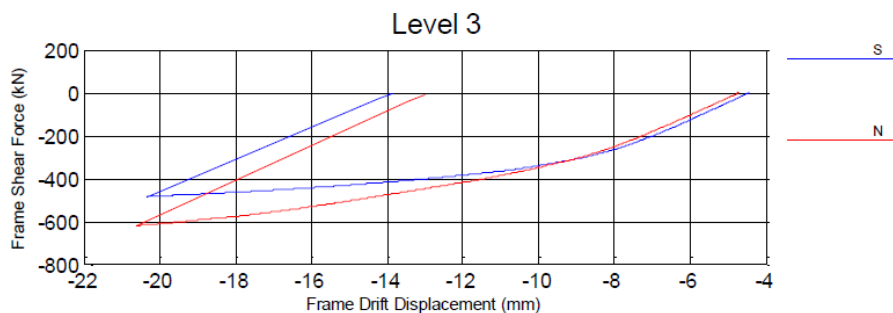


Figure 3.8: Pushover test results. S - south frame and N - north frame. Example from DUAREM [GA et al., 2014]

3.5 Conclusion

In order to numerically simulate a RWSF test on the Prototype discussed in in chapter 2 it is reasonable to conclude that the most suitable one would be a Pushover simulation. This is because, as previously mentioned, the Pushover is also a non-linear static seismic analysis method which is further discussed in section 4.3.

4 Seismic analysis & design methods

The aim of this chapter is to briefly describe the seismic analysis & design methods in EN1998-1 [2004] used to study the prototype. Some of the methods were previously studied in depth by the author and presented in the form of a case study [Minkov, 2022]. For the sake of avoiding repetition, reference to the aforementioned is made whenever a more in-depth explanation is required.

4.1 Introduction

There are many seismic analysis methods available, it is however decided to delimit the choice to what EN1998-1 [2004] can offer. Figure 4.1 below illustrate the four main seismic analysis methods proposed by EN1998-1 [2004].

		Structural model	
		Linear <i>EI, A, L, G</i> etc. = constant [K] = constant	Non-linear <i>EI</i> ≠ constant [K] ≠ constant
Seismic loading	Static P	Lateral force method of analysis (EC8-1, 4.3.3.2)	Pushover analysis (EC8-1, 4.3.3.4.2)
	Dynamic $P(t)$	Modal response spectrum analysis (EC8-1, 4.3.3.3)	Non-linear time history analysis (EC8-1, 4.3.3.4.3)

Figure 4.1: Analysis methods in EC8 [Minkov, 2022]

The Modal response spectrum analysis (MRSA) is the most preferred methods by earthquake engineers. This is because it is one of the most well established and researched analysis methods in EN1998-1 [2004]. Moreover, it is based on modal analysis which provides transparency of the output that helps understand the structural response. This is the reason for choosing the MRSA to analyse the Prototype structure (see later in chapter 5). The method is further discussed in details in the following section 4.2.

The Pushover analysis is most often used as a tool to evaluate the structural behaviour. Its most common use is in retrofitting and numerical assessment of old structures. As mentioned in section 3.4, it is also a RWSF test method. This makes it ideal to use as numerical tool for simulating and assessing the response of the Prototype structure during a RWSF test (see later in part IV). The method is further discussed in details in the following section 4.3.

4.2 Modal response spectrum (MRSA)

The MRSA is a pseudo dynamic linear analysis method. The method takes into account the dynamic characteristics of a structure (eigenperiod, damping, etc.) via a Modal analysis. Its equation of motion is stated in modal form in (4.1) where η_i are the modal coordinates with i being the investigated eigenmode.

$$\bar{m}_i \ddot{\eta}_i + \bar{c}_i \dot{\eta}_i + \bar{k}_i \eta_i = \bar{p}_i \quad (4.1)$$

An equivalent static load is derived from a response spectrum (Appendix D.1.1) and it simulates the maximum response (i.e. displacement) the structure will exhibit. The method is covered in the following five steps:

1. Perform a Modal Analysis and obtain the eigenperiod T_i of the different mode shapes i . According to EN1998-1 [2004] at least 90% of the modal mass must be activated - this dictates the minimum number of mode shapes i that must be investigated.
2. Choose a suitable elastic response spectrum S_e from EN1998-1 [2004] (figure 4.2) which best describes the expected geodynamical environment at the location of the structure - soil conditions, ground acceleration a_g , etc.
3. Based on how ductile the structure is (dictated by the behaviour factor q) obtain the design response spectrum S_d . Higher q corresponds to high ductility which lowers the S_d . However, a $q > 2$ requires undertaking special design measurements (capacity design concept) which ensure sufficient ductility by establishing an adequate dissipative mechanism - see more in section 4.4.1.
4. Use the response spectrum and modal analysis results to derive a design spectral acceleration $S_d(T_i)$ for each of the investigated mode shapes i . The $S_d(T_i)$ provides an equivalent static load P in each DOF of a given mode shape i . The load P simulates the maximum response (i.e. displacement) the structure will exhibit in the given mode shape for the given response spectrum.
5. Use a modal combination method (most often CQC) to combine the response from the different mode shapes i and obtain the final response of the structure - see also Appendix D.1.2.

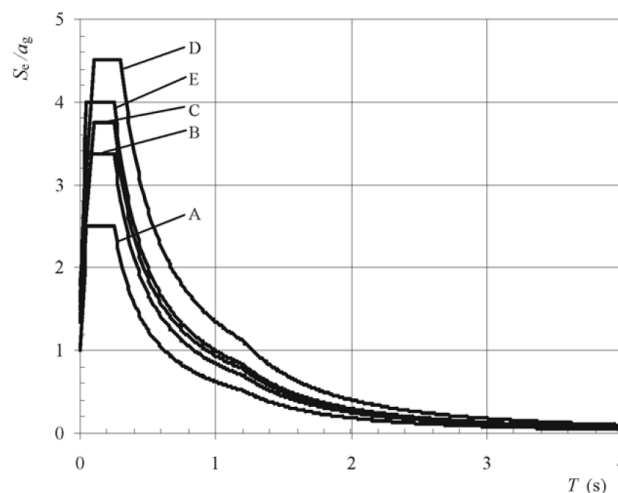


Figure 4.2: Elastic response spectrum type 1 for soil types A to E and $\xi = 5\%$ [EN1998-1, 2004]

4.3 Pushover analysis (PA)

This is a non-linear static analysis method as seen in figure 4.2, therefore its equation of motion is as stated in (4.2) below.

$$[M]\{\ddot{D}\} + [C]\{\dot{D}\} + [K(D)]\{D\} = [P] \quad (4.2)$$

The Pushover analysis works by monotonically increasing a set of static lateral forces on a non-linear numerical model with constant gravity loads. With increase of lateral loading, the response of the structure can be visualized through a capacity curve (top displacement - base shear)

As a first step a lateral load distribution type must be chosen. According to EN1998-1 [2004] the following two types must be studied and the one that yields the most conservative result for the given investigation must be used (see also figure 4.3):

1. Mass proportional (uniform) load distribution. This distribution assumes constant acceleration along the structure height which means that the lateral loads are proportional to the mass on each storey i . The force is obtained as $F_1^i = m_i$.
2. Modal load distribution assumes acceleration which is proportional to the fundamental mode shape m . In this case the normalized displacement Φ_m^i from the modal analysis of mode shape m is used to obtain the lateral force as $F_2^i = m_i \Phi_m^i$.

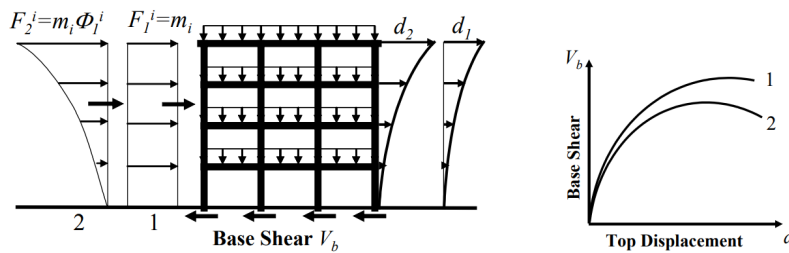


Figure 4.3: Load distributions methods according to EN1998-1 [2004] and the corresponding pushover response curves [Spacone et al., 2010]

For more details regarding the theory behind the Pushover analysis please refer to Appendix E.1.

4.4 Earthquake design

Once earthquake waves reach the surface they carry large amount of seismic energy $E_{seismic}$ which causes the ground and the buildings attached to it to shake violently. Generally, buildings can dissipate this energy through elastic (strain) energy $E_{elastic}$, inelastic energy $E_{inelastic}$, external $E_{damping}$ and material E_{ξ} damping as shown in (4.3).

$$E_{seismic} = E_{elastic} + E_{inelastic} + E_{damping} + E_{\xi} \quad (4.3)$$

As seen in figure 4.4, the maximum elastic energy is $E_{elastic} = 1/2 f_y \epsilon_y$ which is still very low compared to the available inelastic energy $E_{inelastic}$. This is the reason why earthquake resistant structures are very often designed to dissipate the energy through inelastic behaviour. This behaviour is ensured by providing sufficient ductility in lateral restraining systems of the structure. One way to do that is through capacity design, which is discussed in the following section 4.4.1. Another option is to increase $E_{damping}$ by employing an external damping mechanism such as the viscous damper shown in figures 4.5 and 4.6, however this can be very expensive.

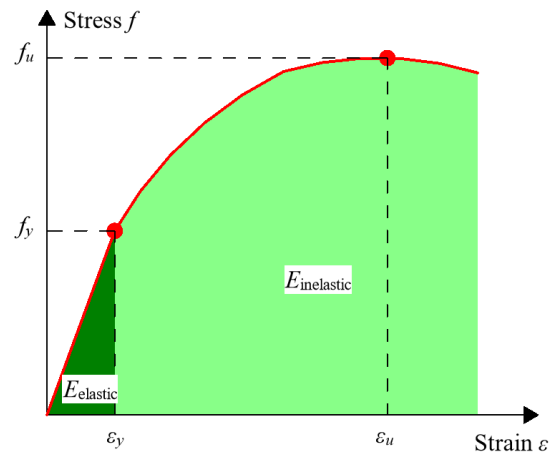


Figure 4.4: Elastic and inelastic energy on a typical stress-strain curve for steel



Figure 4.5: Fluid viscous damper employed on a bridge. Photo courtesy of roadjz.com.



Figure 4.6: Fluid viscous damper employed on a structure. Photo courtesy of roadjz.com.

4.4.1 Capacity design and influence of behaviour factor

The capacity design is an earthquake design method which aims at providing non-dissipative (ND) structural members with sufficient overstrength compared to the dissipative (D) ones. In this way it is ensured that when D members enter in inelastic stage (energy dissipation), the ND ones remain within their elastic limit. This is a rather smart approach since one can design the D members to be replaceable after they have accumulated too much plastic deformations. This method can be illustrated with a rather simple example - a chain with many brittle links (non-dissipative elements) and a ductile (dissipative element) as shown in figure 4.7

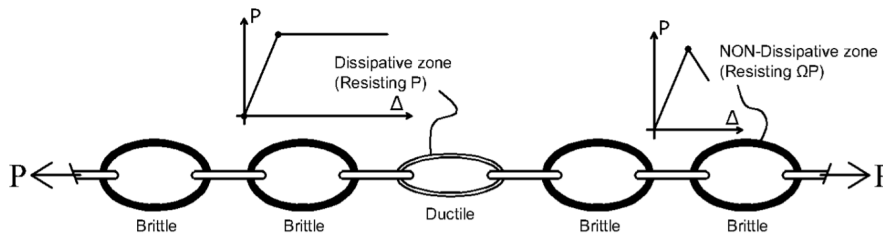


Figure 4.7: Capacity design principle: chain with brittle and ductile links [Khosro and Naqash, 2014]

In [EN1998-1, 2004] the use of this method is required if a ductility class medium DCM or high DCH is chosen i.e. when a behaviour factor of $q > 2$ is selected as shown in figure 4.8. Choosing $q < 4$ allows for working in the linear-elastic range which does not require employing special earthquake design procedures. However this can result in very large structural members since the seismic energy is dissipated only through $E_{elastic}$.

However, the behaviour influences the size of the seismic loads through the response spectra: the higher the q - the lower the spectral acceleration S and therefore applied seismic forces - see figure 4.9. Reducing the response spectra through q is how EN1998-1 [2004] indirectly exploits the non-linear properties of structures in DCM and DCH.

Design concept	Structural ductility class	Range of the reference values of the behaviour factor q
Concept a) Low dissipative structural behaviour	DCL (Low)	$\leq 1.5 - 2$
Concept b) Dissipative structural behaviour	DCM (Medium)	≤ 4 also limited by the values of Table 6.2
	DCH (High)	only limited by the values of Table 6.2

Figure 4.8: Influence of q on the design concepts [EN1998-1, 2004]

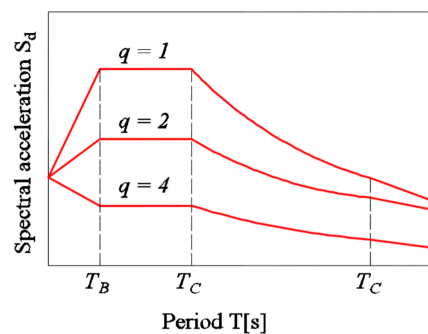
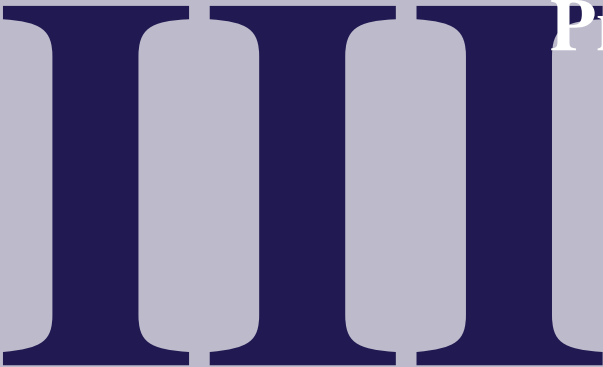


Figure 4.9: Influence of q on the response spectra [Peres et al., 2016]



Prototype Linear Analysis & Design

5	Modal Response Spectrum Analysis	41
5.1	Introduction	
5.2	Linear computational model	
5.3	Modal analysis parameters	
5.4	Response spectrum	
5.5	EC8 criteria and output quality assurance	
6	Capacity design	57
6.1	CBF	
6.2	MRF	
7	Seismic design situation	71
7.1	Seismic load cases and combinations	
7.2	Member capacity check (ULS+SLS)	
7.3	Conclusion	

5 Modal Response Spectrum Analysis

This chapter contains the documentation of the linear analysis performed on the Prototype structure (section 2) using the MRSA method previously discussed in section 4.2. The output from the used computational model is verified and described. The criteria posed by EN1998-1 [2004] in relation to MRSA are discussed in details.

5.1 Introduction

The three main aspects for performing the Modal Response Spectrum Analysis (MRSA) are:

- Choice of computational model - section 5.2
- Choice of modal analysis parameters - section 5.3
- Choice of response spectrum - section 5.4

Section 5.5 contain the quality assurance of the output from the analysis and the verification of the criteria posed by EN1998-1 [2004] in relation to MRSA. The following is part of it:

- Eigenperiods, mass participation and mode shapes - subsection 5.5.1
- Application of torsional effects - subsection 5.5.2
- Quality assurance of base shear - subsection 5.5.3
- Seismic displacements - subsection 5.5.4
- Damage limitation - subsection 5.5.5
- Sensitivity to second order effects - subsection 5.5.6
- Buckling analysis of columns - subsection 5.5.7

5.2 Linear computational model

The well known numerical tool Autodesk Robot [2021] is used to create the computational model (see figure 5.1) on which the MRSA is performed. The origin (0,0,0) is the crossing point of grid A and 1 at level +0.00. The output is verified via a quality check which can be seen in Appendix B.4. For the node and member numbers please refer to Appendix B.1.

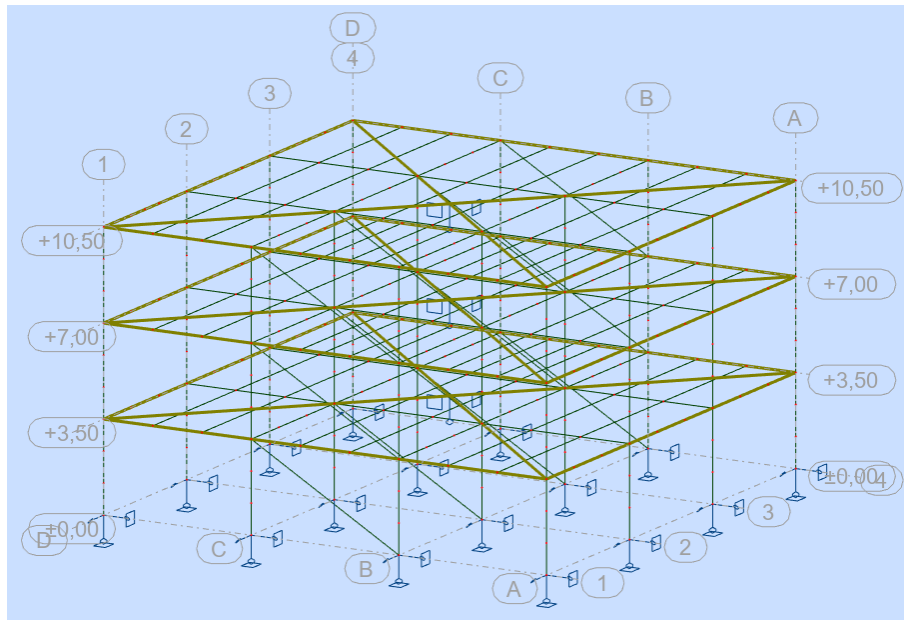


Figure 5.1: Computational model with shown support conditions and diaphragms

The most important modelling choices and assumptions are briefly summarized in the points below:

- A spatial model has been used with UX UY UZ termed as translational degrees of freedom (DOF) and RX , RY and RZ termed as rotational DOF.
- A linear elastic model is used with $P - \Delta$ effects ignored (see section 5.5.6)
- The floor diaphragm is simulated by fixing only the UX , UY and RZ DOF i.e. its vertical stiffness is neglected. In this way the MRF beams are loaded with seismic internal forces (primarily bending moment) instead of the diaphragm.
- The facade elements are modelled as cladding with no stiffness since they are non-load-bearing part of the structure.
- The foundation is modelled as rigid i.e. the soil-structure interaction is not considered as stated in the Thesis delimitation in section 1.5.
- The boundary conditions discussed in section 2.6 are simulated by fully releasing or fixing the appropriate DOF.

5.3 Modal analysis parameters

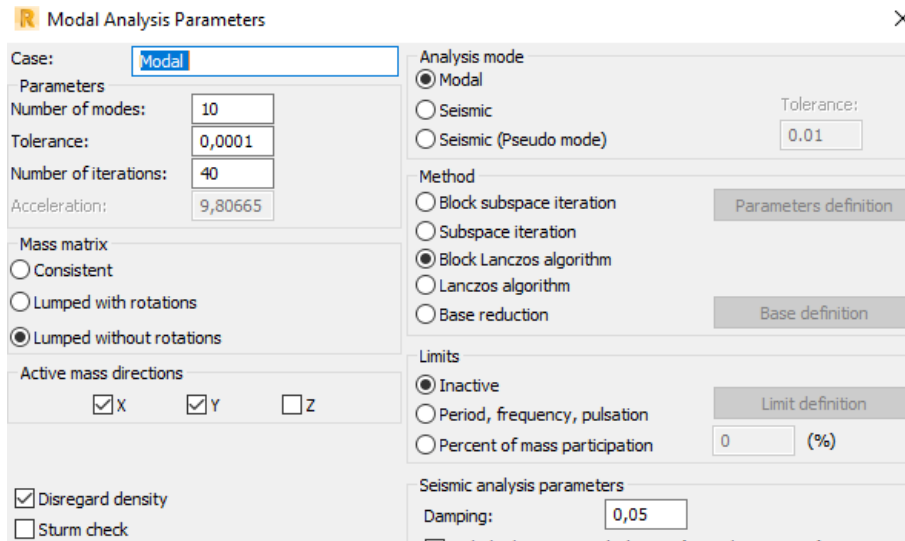


Figure 5.2: Modal analysis parameters in Autodesk Robot [2021]

- The mass is defined following EN1998-1 [2004] as shown in (5.1). Table 5.1 shows how it is split along each storey.
- The mass is lumped without rotations (diagonal mass matrix) i.e. mass rotational DoF are neglected. According to Autodesk Robot [2021] using this type of mass matrix requires minimum computational efforts and provides sufficiently accurate results.
- The mass is activated only in X and Y directions i.e. vertical seismic actions (Z -direction) are not considered since it is not required by EN1998-1 [2004] and it is not a common design practise. Moreover, in some cases activating the mass in Z -direction can lead to net reduction in the downward action.
- The accidental torsional effects are generated through mass shifting option in Autodesk Robot [2021] (see section 5.5.2)
- The rest of the parameters can be seen in figure 5.2 and are based either on recommendations from Autodesk Robot [2021] or practical experience.

$$m_{dyn} = 1.0kG + 0.4kS1 + 0.24kQ2 = 775t \quad (5.1)$$

Table 5.1: Dynamic mass on each storey (rounded)

Storey	Dynamic mass according to EC8-1
i	$m_{dyn,i}$
-	[t]
1	265
2	265
3	245
Σ	775

5.4 Response spectrum

The response spectrum is used to generate the seismic actions during the MRSA (for more information, please refer to section 4.2). Because of this reason it is decided to use a conservative approach when deciding which spectra from EN1998-1 [2004] to use. The following subsections cover the three main parameters influencing the response spectra, namely:

- Behaviour factor - subsection 5.4.1
- Design ground acceleration - subsection 5.4.2
- Ground and spectra type - subsection 5.4.3

The parameters of the chosen response spectrum are summarized in subsection 5.4.4.

5.4.1 Behaviour factor

The behaviour factor q dictates to which extent the non-linear properties of the structures will be exploited. The higher the q - the more dissipative a structure should be designed - see more in section 4.2. After consultation with the company supervisor it is decided to design the lateral systems of the prototype structures (MRF and CBF) as dissipative. This is because their non-linear behaviour can be better controlled and observed when later performing the non-linear static 'Pushover' analysis in Part IV of the report.

According to EN1998-1 [2004] the upper limit of q for MRF and CBF is 4 as shown in table 5.2 below. Choosing a $q > 2$ classifies the prototype structure in ductility class DCM/DCH (section 4.4.1) and this requires performing a Capacity Design according to EN1998-1 [2004] (see later in chapter 6).

Table 5.2: Choice of behaviour factor q according to EN1998-1 [2004]

Structural type	Direction	Behaviour factor	
		q	Reference to EN1998-1 [2004]
Steel MRF	X	4	6.3.2, Table 6.2, a)
Steel CBF	Y	4	6.3.2, Table 6.2, b)

5.4.2 Design ground acceleration

The magnitude of the reference ground acceleration a_{gR} depends on the seismic hazard in a given geographical region. Most prototypes that will be tested in the future RWSF facility will be designed according to the European geodynamical environment. Since Bulgaria is one of the most seismic active regions in Europe (see figure 5.3), it is decided to choose the highest possible a_{gR} on the territory of Republic of Bulgaria, which according to EN1998-1-BGNA [2012] is $a_{gR} = 3.14 \text{ m/s}^2$ or 0.32 g (see table 5.3).

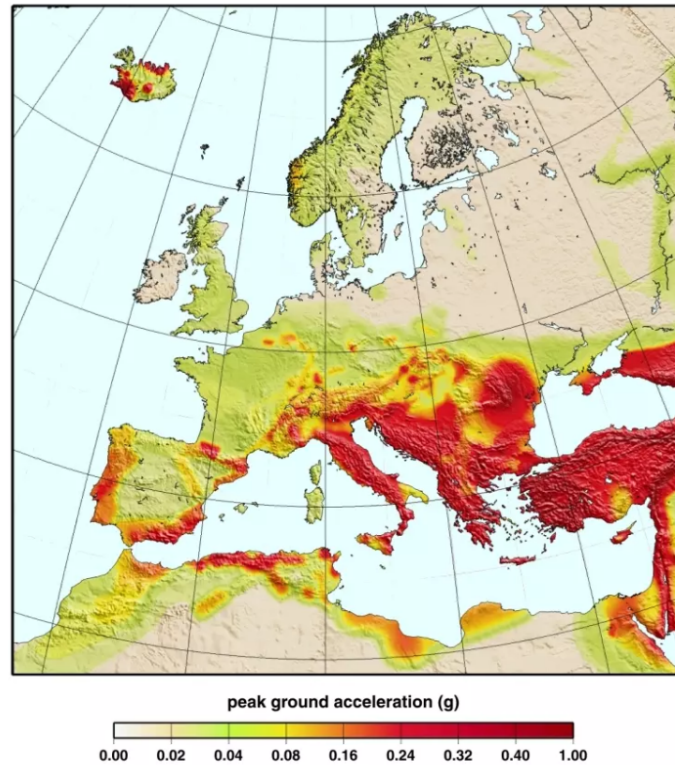


Figure 5.3: European seismic hazard map for the peak ground acceleration with 10% probability of exceedance in 50 years for stiff soil condition [Jiménez et al., 2003]

An importance factor γ_I of 1 is agreed with the company supervisor meaning that design ground acceleration $a_g = a_{gR}$ as shown in (5.2) below.

$$a_g = a_{gR} \gamma_I = a_{gR} \quad (5.2)$$

Table 5.3: Maximum reference ground acceleration for the territory of Bulgaria (return period of 475 years) [EN1998-1-BGNA, 2012]

Reference ground acceleration	Importance factor
a_{gR}/g [m/s ² /g]	γ_I [—]
0.32	1.00

5.4.3 Sensitivity study: ground and spectra types

The propagation of seismic waves below the surface strictly depends on the soil conditions at the site which are described using the ground and spectra types. As a conservative approach, the combination which results in the highest design spectral acceleration $S_d(T_i)$ (i.e lateral force from MRSA) is chosen. For this purpose a sensitivity study is carried out using the the prototype's natural periods in each orthogonal direction $T_1 = 0.67$ s and $T_2 = 0.55$ s (table 5.6) and the different spectra and ground types from EN1998-1-BGNA [2012] (Appendix D.1.3). The aim is to determine which combination results in the highest design peak acceleration S_d .

Using the formulas in Appendix D.1.3 the results for $S_d(T_i)$ are obtained as shown in table 5.4 below. It is clear that ground type C or E (same parameters) and spectra type 1 provide the highest S_d (see also figure 5.4 and table 5.5). The illustrations for all combinations of ground and spectra types can be found in Appendix D.3.

Table 5.4: Sensitivity study results: peak design spectral acceleration for different ground and spectra types. $a_g = 0.32$ g and $q = 4$

Spectra type [—]	Ground type [—]	Peak design spectral acceleration	
		$S_d(T_2)$ [m/s ²]	$S_d(T_1)$ [m/s ²]
1	B	1.86	1.52
1	C or E	2.14	1.76
1	D	1.96	1.76
2	B	1.2	0.99
2	C	1.34	1.10
2	D	1.93	1.58
2	E	1.43	1.17

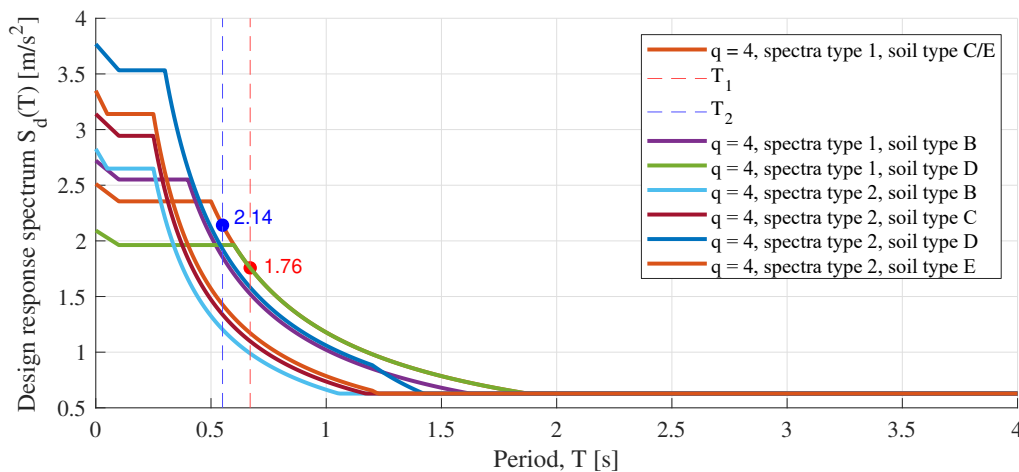


Figure 5.4: Sensitivity study on how soil and spectra types from EN1998-1-BGNA [2012] influence the response of the Prototype structure in its two dominant mode shapes - 1 and 2. $a_g = 0.32$ g and $q = 4$

5.4.4 Conclusion

Behaviour factor of $q = 4$ is chosen which classifies the Prototype structure in ductility class DCM (see section 4.4.1). The ground acceleration is chosen as $a_g = 0.32 \text{ g}$ which is the maximum one on the territory of Republic of Bulgaria. After a sensitivity study ground type C/E and response spectra type 1 are chosen the parameters of which are summarized in table 5.5 below.

Table 5.5: Elastic response spectrum parameters for the chosen response spectra: Type 1 spectra and ground type B [EN1998-1-BGNA, 2012]

Spectra type	Ground type	β	Soil factor S	Periods		
				T_B	T_C	T_D
[—]	[—]	[—]	[—]	[s]	[s]	[s]
1	C or E	0.2	1.2	0.1	0.5	2

5.5 EC8 criteria and output quality assurance

5.5.1 Eigenperiods, mass participation and mode shapes

Performing a modal analysis for the first 5 mode shapes i is deemed satisfactory for obtaining sufficiently accurate response since the activated mass $\sum m_{eff}/m_{dyn}$ for each orthogonal direction is more than 90 % as required by EN1998-1 [2004]. The mode shapes for the first three eigenmodes are shown in figures 5.5 to 5.7. As expected the first two mode shapes are translational and the third one is rotational which is visible by looking at the mass participation ratios in table 5.6 below. Unfortunately, Autodesk Robot [2021] is not able to provide the torsional mass participation UZ when diaphragms are used. This software limitation is accepted since it is of small importance as translational modes have a far greater impact on the structural response than the rotational ones.

Table 5.6: Elastic periods and mass participation ratios UX,UY,UZ

Eigenmode	Frequency	Period	UX	UY	UZ
i	f_i	T_i	$m_{eff,x,i}/m_{dyn}$	$m_{eff,y,i}/m_{dyn}$	$m_{eff,z,i}/m_{dyn}$
-	[Hz]	[s]	[%]	[%]	[-]
1	1.50	0.67	79.90	0.00	N/A
2	1.80	0.55	0.00	85.45	N/A
3	2.00	0.50	0.00	0.00	N/A
4	4.66	0.21	0.00	11.24	N/A
5	5.56	0.18	14.34	0.00	N/A
$\sum_{i=1}^5$			94	97	

Since the natural period T is a function of the stiffness k and mass m (5.3) and since the m remains unchanged in both direction it is concluded that the Prototype is stiffer in y -direction due to having a lower T (see table 5.6). This is expected since in most cases a CBF provides higher elastic stiffness compared to a MRF.

$$T = \frac{2\pi}{\omega} \quad \text{where} \quad \omega = \sqrt{\frac{k}{m}} \quad (5.3)$$

According to Damkilde [2019], a basic estimate of the structure's eigenperiod can be performed using the Rayleigh quotient. The quotient is defined as the ratio between the elastic and kinetic energy as show in (5.4) below. Please refer to Appendix D.2 for the detailed calculation.

$$\omega^2 = \frac{E_{Elastic}}{E_{Kinetic}} \quad \implies \quad T = 2\pi \sqrt{\frac{E_{Kinetic}}{E_{Elastic}}} \quad (5.4)$$

The results for both lateral systems (orthogonal directions) can be seen in table 5.7. Since the deviation between the analytical (Rayleigh) and numerical (Robot) results is very small, the validity of T_1 and T_2 eigenperiods is confirmed.

Table 5.7: Periods

Calculation method	MRF	CBF
	T_1	T_2
	[s]	[s]
Robot	0.67	0.55
Rayleigh	0.68	0.57

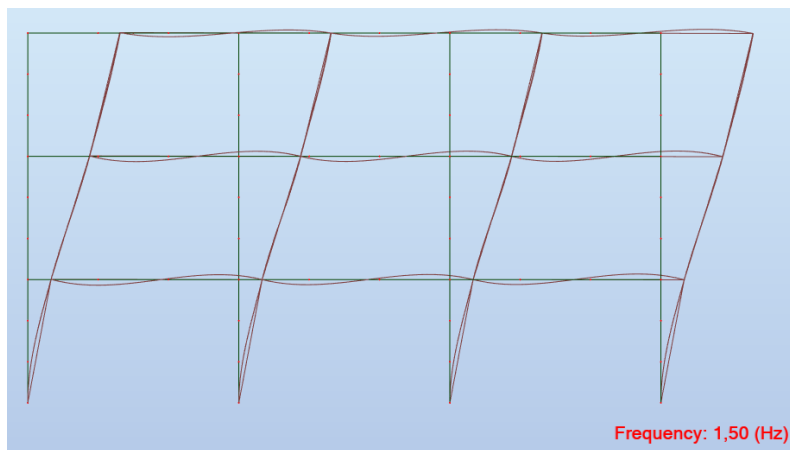


Figure 5.5: Mode 1 mode shape, dominant in x -direction

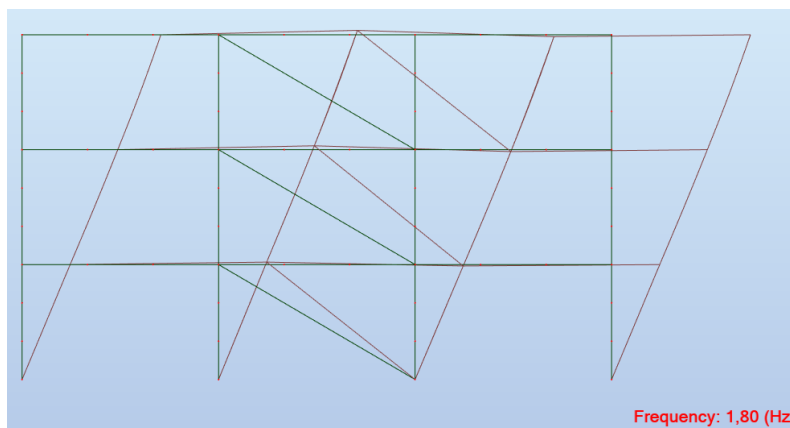


Figure 5.6: Mode 2 mode shape, dominant in y -direction

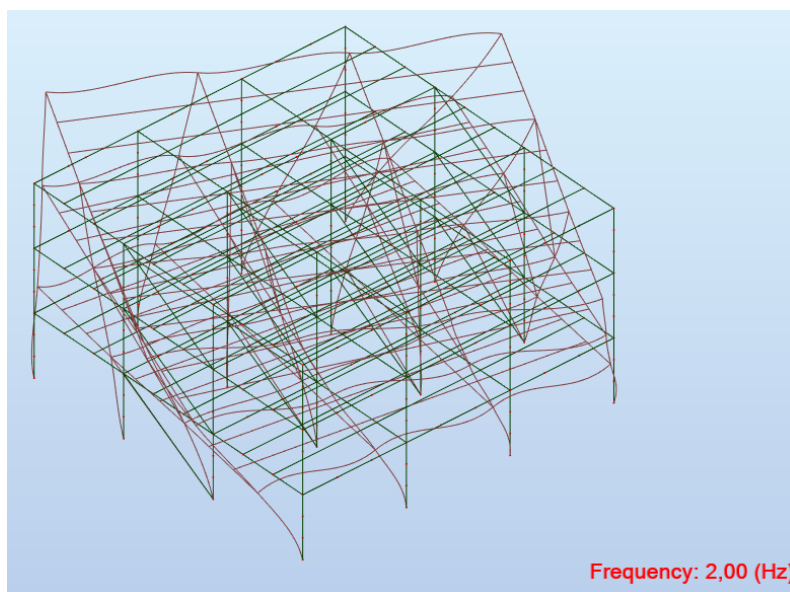


Figure 5.7: Mode 3 mode shape, torsional

5.5.2 Torsional effects

Buildings subjected to ground shaking undergo lateral as well as torsional motions simultaneously. Such motions are due to natural torsion in buildings with asymmetric plan; and accidental torsion in all buildings even with symmetric plan [Chopra and la Llera, 1996]

The natural torsion arises when the center of mass (CM) and center of stiffness (CS) are not in the same point i.e. due to structural irregularity in plan. It is well understood and quite predictable in contrast to the accidental one which arises from the uncertainty of the mass and stiffness distribution within the building and must be accounted for during the analysis. The accidental torsion is introduced by the accidental eccentricity e_a . There are two ways to define e_a in Autodesk Robot [2021]:

- **Method 1** - the accidental eccentricities are taken into account by moving the CM by 5 % of the dimension of the floor in the perpendicular direction to the seismic action $e_{a,x} = 0.05L_x$. This results in the torsional moment $M_z = F_y e_{a,x}$ which is applied in the CM.
- **Method 2** - the accidental eccentricities are simulated by modelling the shift of the mass i.e. by changing the mass matrix $[M]$. The software does this by generating additional nodal masses in the elements.

A brief study has been performed by the author in his previous scientific work (section 9.3 of Minkov [2022]) where it was concluded that the way Autodesk Robot [2021] applies the eccentricities leads to more conservative results (see figure 5.9). This is why it is decided to use Method 2 to apply e_a on the prototype structure. Moreover only x^+, y^+ and x^-, y^- eccentricity cases (figure 5.8) are considered due to the symmetry in plan of the prototype structure.

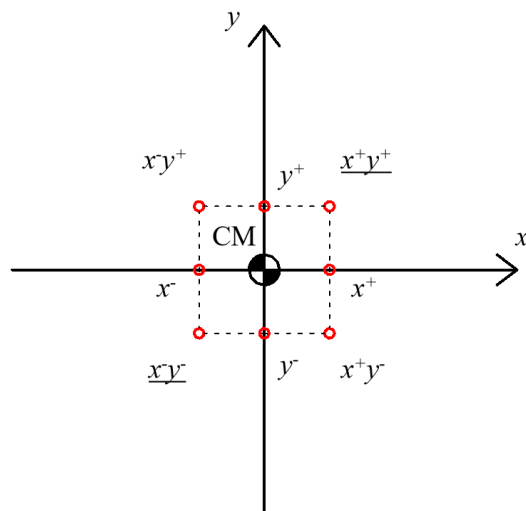


Figure 5.8: Investigated accidental torsion cases (underlined)

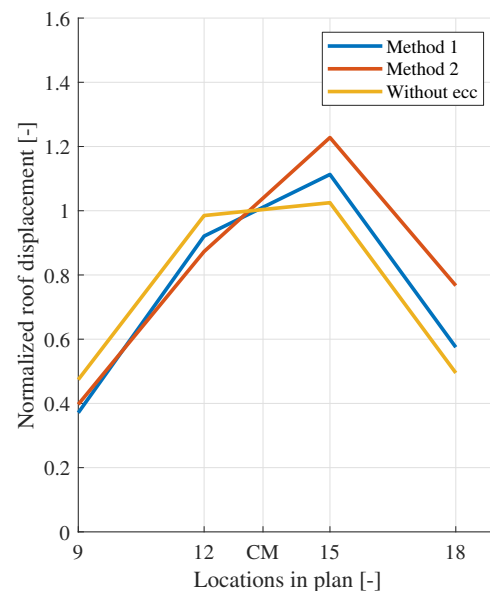


Figure 5.9: Normalized roof displacements for eccentricity case x^+y^- for seismic load in y-direction using different methods [Minkov, 2022]

5.5.3 Base shear

The storey shear forces for each orthogonal direction are illustrated in figures 5.10 and 5.11 and are obtained by summing up the lateral (seismic) forces on a current storey with the ones from the storey above it. Their value is based on the MRSA results from mode 1 for x and mode 2 for y or in other words - the dominating mode shape in each direction.

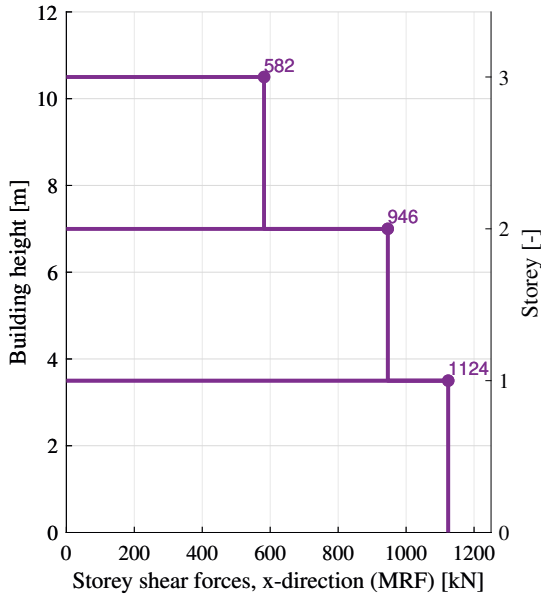


Figure 5.10: Storey shear forces in x-direction

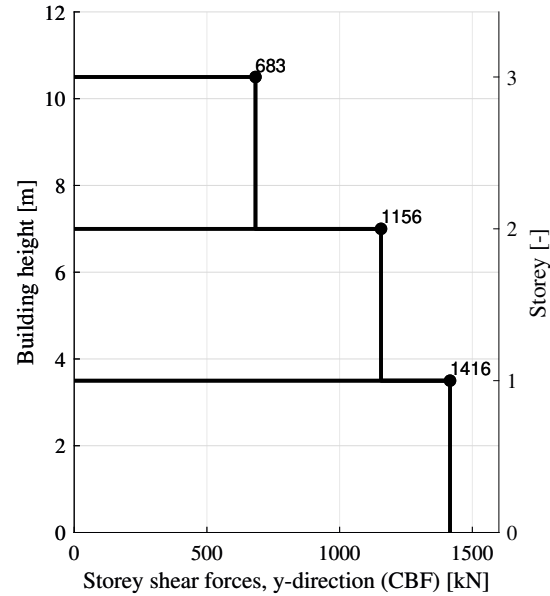


Figure 5.11: Storey shear forces in y-direction

One can notice that the base shear $F_{b,y}$ is around 20% larger than $F_{b,x}$. This is expected since as previously discussed in section 5.5.1 the CBF is stiffer than the MRF and thereby 'accumulates' higher storey shear forces F_i . This results in higher spectral acceleration S_d (see figure 5.4) in y -direction (CBF) and thereby larger lateral forces. In fact the S_d in y -direction is 19% larger than in x -direction which is very close to the base shear force difference of 20%.

Additionally, the value of F_b can be quality checked by ensuring it fits between its upper and lower boundaries as proposed by Bisch et al. [2011]. These boundaries are created by the maximum and minimum F_b that can be produced by the design spectrum in each orthogonal direction $S_d(T_1)$ and $S_d(T_2)$ and multiplying it with m_{eff} for the lower bound and m_{dyn} for the upper one (see subsection 5.4.3). The calculation can be seen in Appendix D.4. The results are summarized in table 5.8 from which can be concluded that the calculated F_b is very close to the more realistic lower bound.

Table 5.8: Check of base shear (see Appendix D.4)

Direction	Lower bound $F_{b,LB} = S_d(T_i)m_{eff}$ [kN]	Calculated F_b [kN]	Upper bound $F_{b,UB} = S_d(T_i)m_{dyn}$ [kN]
X	1088	1124	1362
Y	1416	1416	1659

5.5.4 Displacements

In relation to MRSA two types of displacements are defined. The elastic d_e and seismic d_s . As seen in (5.5) d_s is obtained by multiplying d_e with the behaviour factor $q = 4$ (see subsection 5.4.1) which indirectly takes into account the real non-linear behaviour of the structure (see more in subsection 4.4.1).

$$d_{s,i} = qd_{e,i} \quad (5.5)$$

The absolute value of the mean nodal seismic displacements at each storey $\bar{d}_{s,x}$ and $\bar{d}_{s,y}$ (see table 5.9) are used to plot the displacement curves in figure 5.12 so that the global structural behaviour can be better visualized.

Table 5.9: Absolute value of the mean nodal elastic and seismic displacements at each storey for each orthogonal direction

Storey	Behaviour factor q_x, q_y	Elastic displacement		Seismic displacement	
		$\bar{d}_{e,x}$ [mm]	$\bar{d}_{e,y}$ [mm]	$\bar{d}_{s,x}$ [mm]	$\bar{d}_{s,y}$ [mm]
3	4	25.85	21.63	103.41	86.52
2	4	17.35	14.93	69.41	59.72
1	4	6.60	7.57	26.41	30.28

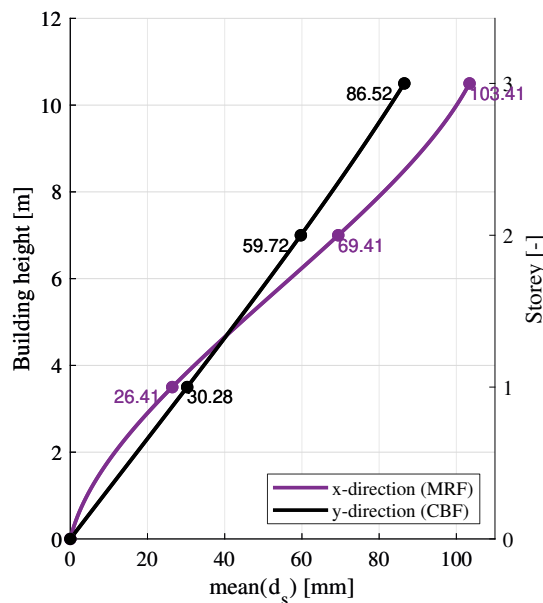


Figure 5.12: Absolute value of the mean nodal seismic displacements in x and y directions

As expected, the shape of the displacement curve in x-direction (MRF) reminds that of a cantilever column since the M_y moment is restrained at the column's support (i.e. level 0). Contrary, the displacement curve in y-direction (CBF) is a lot more linear due the M_x release at level 0. Additionally, the displacement curves in x and y directions match very well the vibration modes of mode 1 (figure 5.5) and 2 (figure 5.6) respectively. Moreover, the MRF displacements are larger than the CBF's since, as previously mentioned, its stiffness is lower. All of this leads to the conclusion that the computational model behaves as expected and that the results are trustworthy.

5.5.5 Damage limitation

As part of the design verification in EN1998-1 [2004] one must assure that the non-structural elements (NSE), such as the cladding, will not be damaged by excessive inter-storey displacements. This is why the design inter-storey drift d_r (5.6) is used to set the damage limitation criteria defined in (5.7) where i is the storey number and $\bar{d}_{s,i}$ is defined in (5.5).

$$d_{r,i} = \bar{d}_{s,i} - \bar{d}_{s,i-1} \tag{5.6}$$

Damage limitation - EC8-1, 4.4.3.2

$$d_{r,i} v \leq \alpha h \equiv \frac{d_{r,i}}{h_i} \leq \frac{\alpha}{v} \tag{5.7}$$

Result: OK for ductile NSE

Where:

i	Storey number	[—]
$d_{r,i}$	Inter-storey drift as defined in (5.6)	[mm]
v	Reduction factor (0.5 for importance class 2)	[—]
α	0.005, 0.0075 or 0.010 depending on the ductility of non-structural elements	[—]
h_i	Storey height	[mm]

For more details, please refer to Appendix D.5

The results for both orthogonal directions and each storey are visualized in figures 5.13 and 5.14 below. As expected, the largest drift is in storey 2 of the MRF due to its cantilever behaviour. The results show that the prototype structure must not have brittle NSE (ex. glass) attached to it since the criteria for $\alpha = 0.005$ in x direction of storey 2 is not met. After consulting with the company supervisor it was decided to accept this limitation since this criteria is very crude.

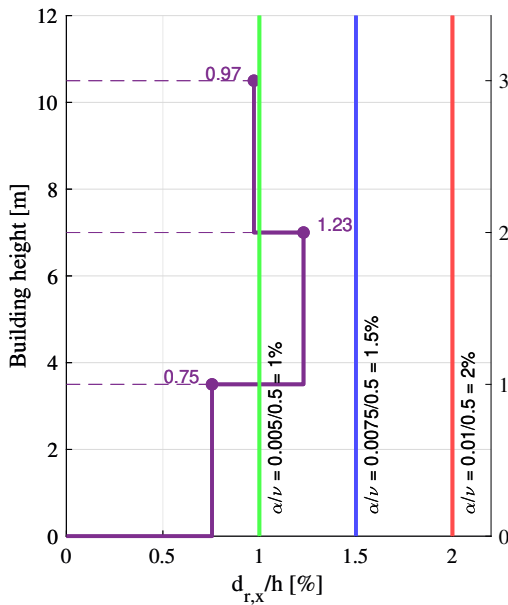


Figure 5.13: Interstorey drift control for longitudinal x -direction according to EN1998-1 [2004]

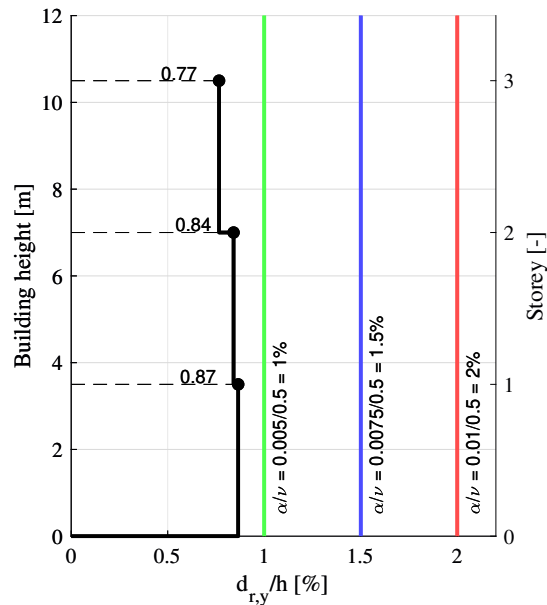


Figure 5.14: Interstorey drift control for transverse y -direction according to EN1998-1 [2004]

5.5.6 Second order effects

Second order effects (also called $P - \Delta$ effects) are a type of geometrical non-linearity causing the accumulation of a second order moment M_P in deformed structural members with axial forces. Usually $P - \Delta$ effects are ignored since their contribution to the design moment in the members is negligible. However, the presence of large M_P compared to the seismic moment M_V can lead to a notable influence of the second order effects and the necessity to perform a $P - \Delta$ analysis. This is why the criteria for the inter-storey drift coefficient θ is introduced in (5.8) and based on the obtained results, illustrated in figures 5.15 and 5.16, such an analysis is not required.

Inter-storey drift sensitivity coefficient - EC8-1-4.4.2.2(2)

$$\theta = \frac{M_{m,i}}{M_{V,i}} = \frac{m_{dyn,i}d_r}{V_{tot,i}h_i} \leq 0.1 \quad \text{Result: } P - \Delta \text{ analysis is not required} \quad (5.8)$$

Where:

i	Storey number	[-]
$M_{m,i}$	Second order 'destabilizing' moment	[kNm]
$M_{V,i}$	'Stabilizing' moment	[kNm]
$m_{dyn,i}$	Dynamic mass at storey i according to table 5.1	[kN]
$V_{tot,i}$	Seismic storey shear according to figures 5.10 and 5.11	[kN]
$d_{r,i}$	Inter-storey drift at storey i as defined in (5.6)	[mm]
h_i	Inter-storey height	[mm]

For more details, please refer to Appendix D.6

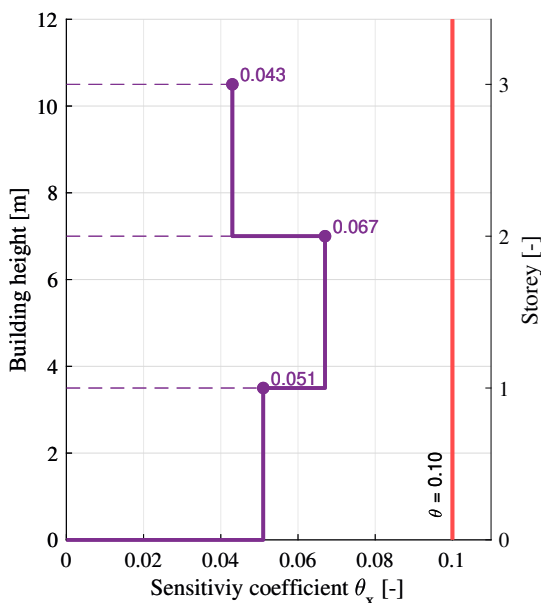


Figure 5.15: Inter-storey drift sensitivity coefficient control for transverse x -direction according to EN1998-1 [2004]

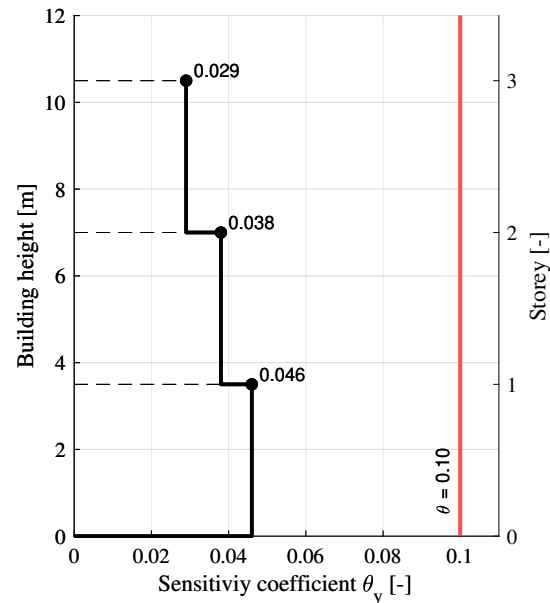


Figure 5.16: Inter-storey drift sensitivity coefficient control for transverse y -direction according to EN1998-1 [2004]

5.5.7 Buckling analysis of columns

In addition to the inter-storey drift sensitivity check according to EN1998-1 [2004] demonstrated in (5.8) one must assure that the change of structural behaviour caused by the effects of deformed geometry of the structure is not significant according to EN1993-1-1 [2007].

These effects are expressed with the increase of internal forces (or moments) in columns when they buckle (i.e. when $P - \Delta$ is introduced). For measuring their significance the critical coefficient α_{cr} is used. The coefficient is important for understanding the behaviour of the columns since it shows how close the applied design axial load F_{Ed} is to its critical (buckling) force F_{cr} . For this purpose a buckling analysis is performed in Autodesk Robot [2021] for the first 10 buckling modes and the ULS combination resulting in the maximum vertical force on the columns. The results are shown in figures 5.17 and 5.18.

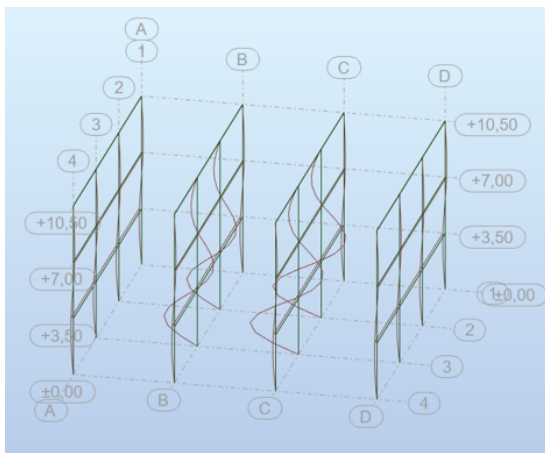


Figure 5.17: Visualization: Buckling analysis of columns in Autodesk Robot [2021], mode shape 1

Case/Mode	Critical coef.	Precision
203/ 1	1,79716e+01	8,59179e-04
203/ 2	1,81626e+01	1,30340e-03
203/ 3	1,82221e+01	1,63773e-03
203/ 4	1,82562e+01	2,70140e-03
203/ 5	3,08174e+01	1,18483e-03
203/ 6	3,14824e+01	3,43215e-03
203/ 7	3,17836e+01	1,60194e-03
203/ 8	3,19376e+01	2,32874e-03
203/ 9	3,20460e+01	3,15257e-03

Figure 5.18: Results: Buckling analysis of columns in Autodesk Robot [2021]

According to EC3-1 if the ratio is more than 10, as shown in (5.9), first order analysis can be performed since the influence of $P - \Delta$ effects on the structural behaviour are negligible. The value of 10 is determined after multiple experimental and numerical studies on buckling of columns in different structural systems.

Column's critical coefficient check - EC3-1-5.2.1(3),(5.1)

$$\alpha_{cr} = \frac{F_{cr}}{F_{Ed}} = 18 \geq 10 \quad \text{Result: } P - \Delta \text{ analysis is not required} \quad (5.9)$$

Where:

F_{cr}	Critical column force	[kN]
F_{Ed}	Maximum existing design axial load from a leading seismic combination	[kN]

For more details, please refer to Appendix D.6

6 Capacity design

This chapter documents the design choices undertaken for the Prototype structure (section 2) and how they conform to the capacity design requirements set in EN1998-1 [2004] with regards to MRF and CBF. Moreover the purpose and logic behind each requirement is discussed in details. The supporting calculations can be found in Appendix F.2 for MRF and F.1 for CBF. The theory behind capacity design is discussed in section 4.4

6.1 CBF

The CBF system dissipates energy by allowing for an inelastic behaviour and forming of plastic hinges in the tensile diagonals. Consequently, the CBF beams and columns must remain as non-dissipative because structure will lose its stability if plastic hinges form there as-well. This is a very common design choice since the CBF braces can be easily replaced once they have yielded. It should be noted that each diagonal can either act in tension or compression, however when compressed it is allowed to buckle causing it to become inactive. This is the reason of having only one pair of diagonals active in the computational model shown in figure 6.1.

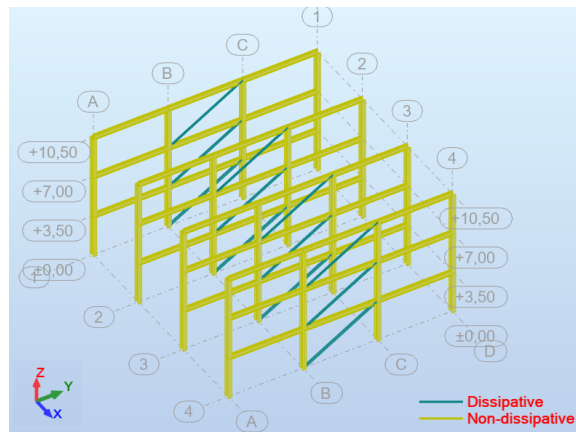


Figure 6.1: Dissipative and non-dissipative elements of the CBF

The requirements set in EN1998-1 [2004] with regards to the dissipative (diagonals) and non-dissipative CBF elements (beams+columns) are discussed in details in the following sections. Due to the sheer amount of calculations, only the results are shown in this chapter, please refer to Appendix F.1 for more details.

6.1.1 Diagonals

The CBF diagonals are the dissipative structural elements in the y -direction. Their correct ductile behaviour is ensured by the choice of a cross section which obeys to all criteria posed in EN1998-1-BGNA [2012] discussed in the following subsections.

Slenderness

The CBF diagonals can act in both compression and tension, however in the computational model the compressive diagonal is assumed as inactive. It is therefore necessary to undertake appropriate design consideration so that the compressive diagonals do not loose stability which would lead to cyclic degradation of the system and loss of its ability to dissipate energy. This is ensured by setting a lower and upper boundary for the slenderness.

Too slender diagonal (according to EC8-1: $\bar{\lambda} \geq 2.0$) risks developing a plastic hinge during flexural buckling. This inelastic behaviour in compression degrades its tensile strength when the brace direction changes (i.e. when it becomes a tensile diagonal). On the other hand, having too bulky diagonal (according to EC8-1: $\bar{\lambda} < 1.3$) makes both braces active which can overload the CBF column in the pre-buckling stage of the compressive diagonal.

Since $\bar{\lambda}$ is function of the buckling length L_{cr} - its choice is an important design consideration. It is decided to take L_{cr} as the full diagonal length which means that the out of plane buckling mode illustrated in figure 6.2 must be achieved by undertaking appropriate design measurements, i.e. diagonals must not be connected in their crossing points. By choosing $L_{cr} = L = 695$ cm, the slenderness requirement is fulfilled as shown in (6.1).

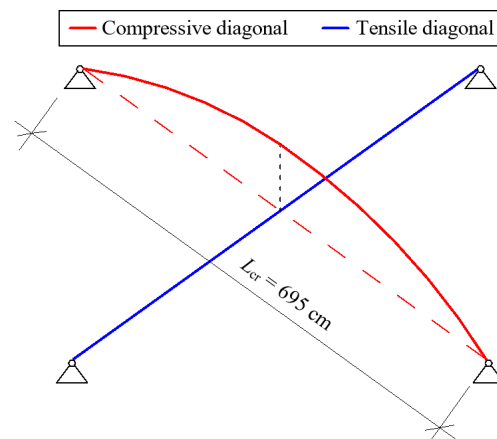


Figure 6.2: CBF buckling mode for the chosen L_{cr}

Slenderness - EC8-1, 6.7.3(1)

$$1.3 < \bar{\lambda}_n \leq 2.0$$

$$\text{Result: } \bar{\lambda}_1=1.34, \bar{\lambda}_2=1.57, \bar{\lambda}_3=1.88$$

(6.1)

Where:

$\bar{\lambda}$		Non-dimensionless slenderness	[-]
n		Storey number where the diagonal is located	[-]

For more details, please refer to Appendix F.1.2

Load-deflection characteristics

Similar load-deflection characteristics at each storey and in both braced directions is a way to ensure that the structure's stiffness (and thereby response) is symmetrical. For this purpose, according to EC8-1, the horizontal projections of the tensile diagonal cross-sections (A^+ and A^-) must not differ with more than 5 % for each storey - see (6.2). The cross sectional area A is used because in a traditional CBF, A is proportional to its lateral stiffness. Since the same tensile diagonal cross-sections are used in both braced directions for a corresponding storey, this rule is obeyed by default.

The authors believe that the below rule of symmetry is necessary for CBF structures because the influence of brace buckling induced cyclic capacity degradation on the global response makes it difficult to accurately predict their behavior. [Vigh et al., 2017]

Similar load-deflection characteristics - EC8-1, 6.7.1(3), (6.11)

$$\frac{|A^+ - A^-|}{A^+ + A^-} \leq 0.05 \quad \text{Result: TRUE} \quad (6.2)$$

Where:

A^+	Horizontal projections of the tensile diagonal cross-sections for direction +	[mm ²]
A^-	Horizontal projections of the tensile diagonal cross-sections for direction -	[mm ²]

For more details, please refer to Appendix F.1.2

Dissipative homogeneous behaviour

This criteria ensures the forming of the correct failure mechanism in the CBF - gradual yielding of the diagonals along the building height. This requires sufficient global ductility of the CBF at each level and is secured by setting a limitation of the strength-to-demand ratio $\Omega_{max}/\Omega_{min}$ (6.3). A low ratio reduces the likelihood for forming of a soft storey mechanism. As seen in (6.3), the criteria is met.

Dissipative homogeneous behaviour - EC8-1, 6.7.3(8)

$$\Omega_{max} \leq 1.25\Omega_{min} \quad \text{Result: TRUE} \quad (6.3)$$

Where:

$\Omega_{max} = \frac{N_{pl,Rd}}{N_{Ed,tension,min}}$	Maximum strength-to-demand ratio	[-]
$\Omega_{min} = \frac{N_{pl,Rd}}{N_{Ed,tension,max}}$	Minimum strength-to-demand ratio	[-]

For more details, please refer to Appendix F.1.2

6.1.2 Beams & columns

Since the beams and columns are the non-dissipative structural elements in the CBF system, they should remain such by providing them with sufficient over-strength Ω . This is ensured by designing them to remain within their elastic range while the diagonals dissipate the energy through inelastic behaviour. EN1998-1 [2004] proposes to do that by increasing the seismic induced axial force N_{Ed} during their capacity check as shown in (6.4). The way this is implemented in the linear computational model in Robot is further discussed in subsection 7.1.3.

Internal forces for verification of CBF beams & columns - EC8-1, 6.7.3(8)

$$N_{Ed} = N_{Ed,G} + 1.1\gamma_{ov}\Omega_{min}N_{Ed,E} = N_{Ed,G} + 1.60N_{Ed,E} \quad (6.4)$$

Where:

$N_{Ed,G}$	Axial force in the CBF beams & columns from non-seismic actions included in a seismic combination	[kN]
$N_{Ed,E}$	Axial force in the CBF beams & column from seismic actions	[kN]
γ_{ov}	Over-strength factor	[-]
$\Omega_{min} = \frac{N_{pl,Rd,d}}{N_{Ed,max,d}}$	Minimum strength-to-demand ratio	[-]
$N_{pl,Rd,d}$	Plastic axial resistance of the diagonals	[kN]
$N_{Ed,max,d}$	Maximum seismic design axial force in the diagonals	[kN]

For more details, please refer to Appendix F.1.2

6.2 MRF

The dissipative (D) zone in the MRF is decided to be in its beams. This requires undertaking suitable design measurements which will ensure a controlled development of plastic hinges in the MRF beams. Another possibility is to dissipate the energy in the beam-column connections but since this is not the case, they must remain as non-dissipative (ND). The MRF columns must also remain ND because development of plastic hinges in both the beams and columns will lead to loss of stability. Moreover, since a global mechanism is preferred the columns must not behave inelastic, otherwise the formation of a weak storey mechanism is a risk.

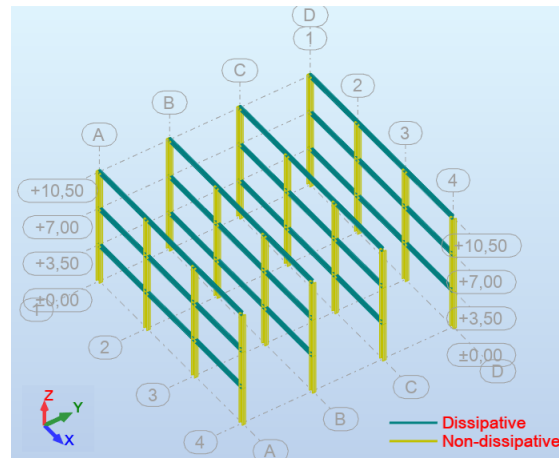


Figure 6.3: Dissipative and non-dissipative elements of the MRF

The requirements set in EN1998-1 [2004] and EN1993-1-1 [2007] with regards the the dissipative (beams) and non-dissipative elements (columns + connections) are discussed in details in the following sections. Due to the sheer amount of calculations, only the results are shown in this chapter, please refer to Appendix F.2 for more details.

6.2.1 Beams

Beams are the dissipative elements in the MRF system. In this relation EN1998-1 [2004] requires the following:

- The size of the internal forces in the beam (N and V) must not reduce its plastic capacity. Additionally the plastic moment resistance should not be exceeded (see subsection 6.2.1).
- Local instabilities of the beam segment next to the connection with the column must be avoided since that will interfere with the formation of the dissipative plastic mechanism (see subsection 6.2.1).

Plastic capacity

An adequate plastic capacity of the beams is ensured by limiting the ratio between their design internal forces and plastic resistance $\frac{F_{Ed}}{F_{pl,Rd}}$ to an appropriate boundary based on numerous experience performed for EC8-1.

However, members in cross sectional classes (CSC) 3 and 4 tend to buckle locally before they reach $F_{pl,Rd}$. In those cases their elastic resistance $F_{el,Rd}$ must be used instead of $F_{pl,Rd}$. The cross sections discussed in section 2.3 are classified as CSC 1 and 2 which means that their $F_{pl,Rd}$ can be utilized since it will develop before reaching a local instability.

The first and most important is the plastic moment capacity which must not be exceeded by the design bending moment as shown in (6.5) below:

Beam plastic moment capacity - EC8-1, 6.6.2(2), (6.2)

$$\frac{M_{Ed}}{M_{pl,Rd}} \leq 100\% \quad \text{Result: } 51\% \quad (6.5)$$

Where:

M_{Ed}	Design seismic bending moment (non CD combination)	[kNm]
$M_{pl,Rd}$	Plastic moment resistance of the beam	[kNm]

For more details, please refer to Appendix F.2.2

Influence of axial and shear forces

It is especially important to ensure that the size of the axial N_{Ed} and shear forces V_{Ed} would not reduce the beam's plastic moment resistance $M_{pl,Rd}$ and rotational capacity θ since it would negatively impact the formation of the dissipative plastic mechanism.

Figures 6.4 and 6.5 below show the points (size of N and V) at which the beam's plastic moment resistance starts to degrade. EC8-1 uses these values as a basis for limiting the axial and shear forces as shown in (6.6) and (6.7).

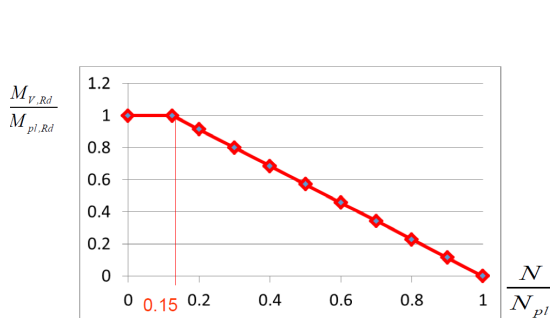


Figure 6.4: Influence of plastic axial ratio on $M_{pl,Rd}$ [Georgiev, 2021]

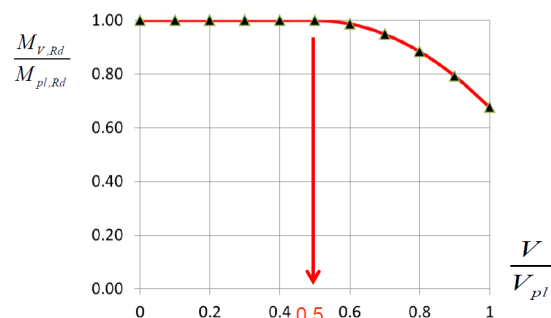


Figure 6.5: Influence of plastic shear ratio on $M_{pl,Rd}$ [Georgiev, 2021]

Beam plastic axial capacity - EC8-1, 6.6.2(2), (6.3)

$$\frac{N_{Ed}}{N_{pl,Rd}} \leq 15\% \quad \text{Result: 0\% (taken by the diaphragm)} \quad (6.6)$$

Where:

N_{Ed}		Design seismic axial force (non CD combination)	[kN]
$N_{pl,Rd}$		Plastic axial resistance of the beam	[kN]

For more details, please refer to Appendix F.2.2

Beam plastic shear capacity - EC8-1, 6.6.2(2), (6.4) + (6.5)

$$\frac{V_{Ed}}{V_{pl,Rd}} = \frac{V_{Ed,G} + V_{Ed,M}}{V_{pl,Rd}} \leq 50\% \quad \text{Result: 29\%} \quad (6.7)$$

Where:

$V_{Ed,G} = \frac{m_{dyn} L_h}{2}$		Design seismic shear due to the dynamic mass	[kN]
$V_{Ed,M} = \frac{M_{pl,A} + M_{pl,B}}{L_h}$		Design seismic shear due to plastification at ends A and B	[kN]
$V_{pl,Rd}$		Plastic shear resistance of the beam	[kN]

For more details, please refer to Appendix F.2.2

Determining V_{Ed} in (6.7) above depends on the assumed location of plastic hinges since the MRF beam enters a plastic stage when it dissipates energy. It is decided not to stiffen the connection which means that plastic hinges are expected to occur right next (or very close) to the outer part of the MRF column flange as shown in figure 6.6. In this case the design shear is formed as shown below:

- $V_{Ed,G}$ caused by the dynamic mass m_{dyn} on the beam (table 5.1)
- $V_{Ed,M}$ which arises when the MRF beam reaches its plastic capacity $M_{pl,Rd}$ at its both ends.

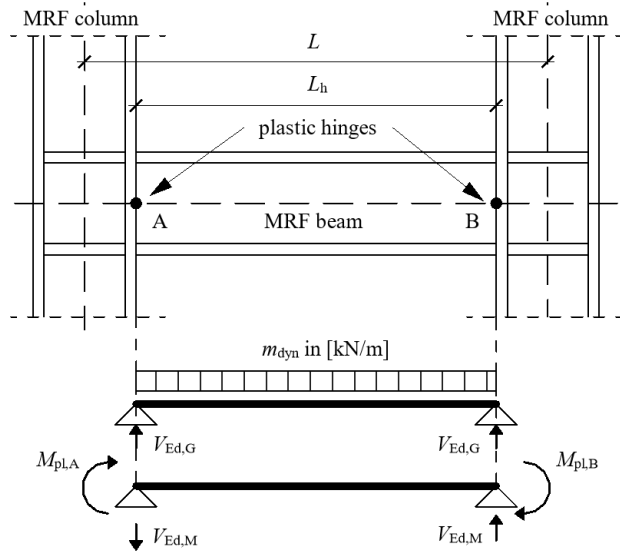


Figure 6.6: Determining the design shear when the MRF beam plastifies at its both ends (6.7)

Segment lateral stability

It is necessary to ensure the lateral stability of the segment of the MRF beam close to the the column. Otherwise, lateral torsional buckling (LTB) may occur before yielding (forming of plastic hinges) leading to adverse effects on the dissipative behaviour of the MRF. By calculating the

stable length $L_{stable} = 1.86\text{ m}$ (see Appendix F.2.3) and comparing it to the unrestrained beam length $L_h = 5.6\text{ m}$ it is concluded that the beam segment close to the MRF column is not laterally stable. This requires providing the MRF beam with a lateral restrain at a maximum distance of L_{stable} from both its ends.

The most common way to do that is to provide diagonal 'kicker' braces extending from the bottom flange of the MRF beam to the top one of an adjacent beam as shown in figure 6.7. This is a very practical solution, however due to the different load-deflection characteristics of both beams, the kicker tends to twist and push the bottom flange of the MRF beam which can alter its stability.



Figure 6.7: Diagonal 'kicker' braces [Hamburger and Malley, 2016]

Due to the problems posed by the 'kicker' braces it is decided to move them one bay from the MRF beam as shown in figure 6.8 below. In this way the brace twisting and pushing of the bottom flange of the MRF beam is avoided.

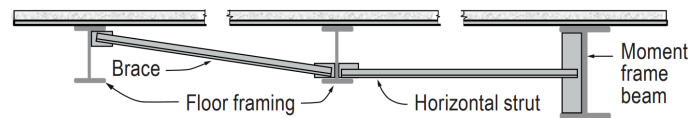


Figure 6.8: Alternate stability bracing detail [Hamburger and Malley, 2016]

An example of how this solution can be implemented on the prototype structure is shown in figure 6.9. Note that the placement of shear connectors at the top flange must not be in the first $2b_{eff,beam} = 340\text{ mm}$ of the MRF beam because the presence of holes can degrade the plastic behaviour in the dissipative zone of the beam segment.

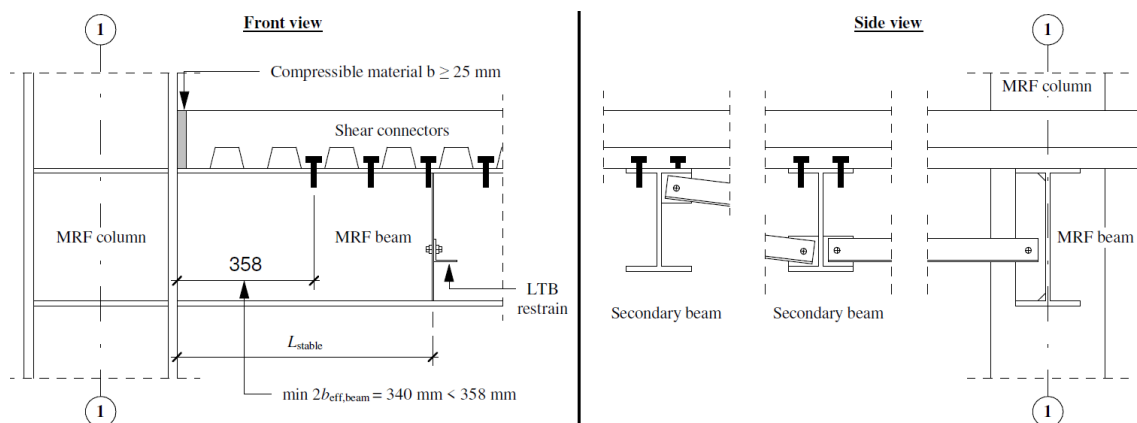


Figure 6.9: Example sketch of the solution in figure 6.8 applied for the prototype structure

6.2.2 Columns & connections

The MRF columns and connection to the MRF beams are chosen to be the non-dissipative structural elements of the MRF. In this relation EC8-1 requires the following:

- A global plastic mechanism must be achieved through suitable design measures (see page 66).
- The size of the internal forces (i.e. shear) must not lead to a reduced resistance of the columns (see page 67).
- Local failure and instabilities in the columns must be avoided so that the desired global plastic mechanism is achieved (see page 67).
- The connections must be provided with sufficient over-strength and adequate ductility so that plastic hinges will first develop in the MRF beams (see page 69).

Additionally, in order for the columns to remain non-dissipative they should (similar to the connections) be provided with sufficient over-strength compared to the beams. This is because the beams experience hardening after yielding which can cause the non-dissipative elements to yield before the wanted global mechanism is achieved. In EN1998-1 [2004] the sufficient over-strength is provided by increasing the internal forces in the columns (M , N , V) when verifying their capacity as shown in (6.10). The way this is implemented in the linear computational model in Robot is further discussed in subsection 7.1.3.

Internal forces for verification of MRF columns - EC8-1, 6.6.3(1) (6.6)

$$M_{Ed} = M_{Ed,G} + 1.1\gamma_{ov}\Omega_{min}M_{Ed,E} = M_{Ed,G} + 2.72M_{Ed,E} \quad (6.8)$$

$$N_{Ed} = N_{Ed,G} + 1.1\gamma_{ov}\Omega_{min}N_{Ed,E} = N_{Ed,G} + 2.72N_{Ed,E} \quad (6.9)$$

$$V_{Ed} = V_{Ed,G} + 1.1\gamma_{ov}\Omega_{min}V_{Ed,E} = V_{Ed,G} + 2.72V_{Ed,E} \quad (6.10)$$

Where:

$M_{Ed,G}, N_{Ed,G}, V_{Ed,G}$	Internal forces in the MRF columns from non-seismic actions included in a seismic combination	[kNm, kN]
$M_{Ed,E}, N_{Ed,E}, V_{Ed,E}$	Internal forces in the MRF columns from seismic actions	[kNm, kN]
γ_{ov}	Over-strength factor	—
$\Omega_{min} = \frac{M_{pl,Rd,b}}{M_{Ed,max,b}}$	Minimum strength-to-demand ratio	—
$M_{pl,Rd,b}$	Plastic bending moment resistance of the MRF beam	[kNm]
$M_{Ed,max,b}$	Maximum seismic design bending moment in the MRF beams	[kNm]

For more details, please refer to Appendix F.2.7

Please note that Ω_{min} in (6.10) is calculated based on the plastic resistance of the beam $M_{pl,Rd,b}$ since it is assumed that the MRF beams has formed plastic hinges (i.e. they dissipate energy).

Strong column - weak beam (SCWB) concept

Figure 6.10 illustrates the formation of a local failure mechanism caused by yielding of the ground level columns. This must be avoided because of the potential development of large $P - \Delta$ effects which would cause a structural collapse of the ground floor and the so called 'sandwich' failure. However, by introducing plastic hinges in the MRF beams as shown in figure 6.11. it can be seen that the lateral drift now becomes uniformly distributed along the height and a much more desired global mechanism is achieved.

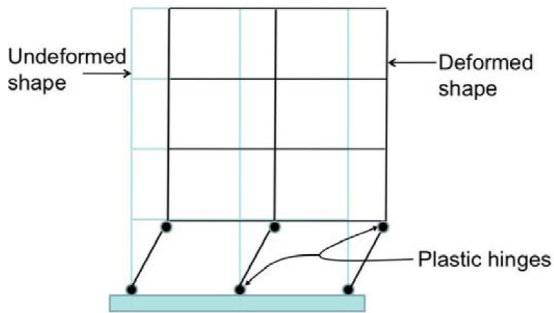


Figure 6.10: Formation of a weak storey mechanism [Hamburger and Malley, 2016]

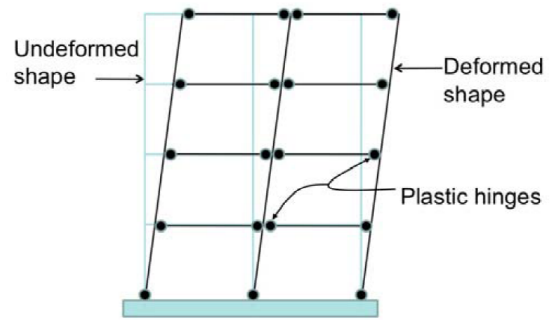


Figure 6.11: Desirable mechanism resulting from using the SCWB concept [Hamburger and Malley, 2016]

The SCWB concept promotes the formation of this desired mechanism (figure 6.11) by ensuring that the bending strength of the MRF columns is at least 30% higher than that of the MRF beams as shown in (6.11). This value is determined by various experiments on MRF.

SCWB - EC8-1, 4.4.2.3(4), (4.29)

$$\sum M_{Rc} \geq 1.3 \sum M_{Rb} \Leftrightarrow \frac{1.3 \sum M_{Rb}}{\sum M_{Rc}} \leq 100\% \quad \text{Result: 21\%} \quad (6.11)$$

Where:

$\sum M_{Rc}$	Sum of design moment resistance of the columns framing the MRF column-beam joint	[kNm]
$\sum M_{Rb}$	Sum of design moment resistance of the beams framing the MRF column-beam joint	[kNm]

For more details, please refer to Appendix F.2.4

Plastic shear capacity

Due to the presence of large base shear in the MRF, it should be checked that the design shear force does not reduce the column's load bearing resistance which would alter its behaviour. EN1998-1 [2004] ensures this by limiting the base shear to a maximum 50% of the column's plastic shear resistance as shown in (6.12). This value is determined by various experiments on MRF.

Column plastic shear capacity - EC8-1, 6.6.3(4), (6.7)

$$\frac{V_{Ed,c}}{V_{pl,Rd,c}} \leq 50\% \quad \text{Result: 7\%} \quad (6.12)$$

Where:

$V_{Ed,c}$	Seismic design base shear in the column (CD combination)	[kN]
$V_{pl,Rd,c}$	Plastic shear load-bearing capacity of the column	[kN]

For more details, please refer to Appendix F.2.5

Panel zone

The panel zone is termed as the part of the MRF column web at its connection with the MRF beam. This zone experiences large shear forces arising from the transfer of moments from the beam to the column. These forces lead to yielding that propagates towards the panel's corners. An example of a deformed panel zone is shown in figure 6.12 on the right.

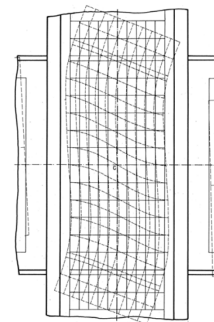


Figure 6.12: Exaggerated deformation of the panel zone [Hamburger and Malley, 2016]

Even though the panel zone holds excellent dissipative properties, its contribution to the dissipative behaviour is most often neglected due to the large axial force in the columns and complicated stress distribution in the welds. EN1998-1 [2004] does not limit the use of the panel zones as dissipative elements but due to the above-mentioned it is decided to keep it within its elastic limit.

As a common design practise, it is decided to use four transverse stiffeners (two at each column side) which are placed as a natural continuation of the beam flanges (see figure 6.9). However, no longitudinal web stiffeners are used which means that the out of plane behaviour of the panel zone depends entirely on the column's cross section. In this way the weight of the structure is increased but the necessity of costly web stiffeners and doubler plates is avoided.

EC8-1 sets two requirements in relation to the panel zone (i.e MRF column web) both of which are related to shear capacity.

The first one is related to its resistance in plastic stage (6.14) and the second - shear buckling (6.15). As seen in (6.13) and figure 6.13, the design shear force $V_{wp,Ed}$ for both requirements is determined assuming that the MRF has entered in a dissipative stage (i.e. inelastic behaviour in the beam and elastic in the column).

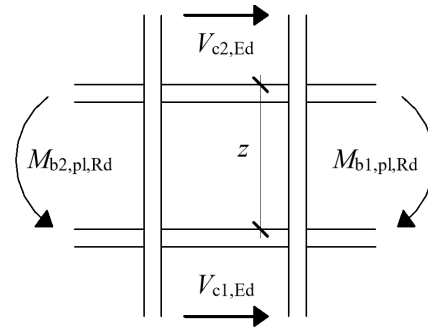


Figure 6.13: Determining $V_{wp,Ed}$ in (6.13)

$$V_{wp,Ed} = \frac{M_{b1,pl,Rd} - M_{b2,pl,Rd}}{z} - \frac{V_{c1,Ed} - V_{c2,Ed}}{2} \quad (6.13)$$

Panel shear resistance in plastic stage - EC8-1, 6.6.3(6), (6.8)

$$\frac{V_{wp,Ed}}{V_{wp,Rd}} \leq 100\% \quad \text{Result: 86\%} \quad (6.14)$$

Where:

$V_{wp,Ed}$	Shear force in the panel zone as in (6.14)	[kN]
$V_{wp,Rd}$	Plastic shear resistance of the panel zone	[kN]

For more details, please refer to Appendix F.2.6

Panel shear buckling in plastic stage - EC8-1, 6.6.3(7), (6.9)

$$\frac{V_{wp,Ed}}{V_{wb,Rd}} \leq 100\% \quad \text{Result: 96\%} \quad (6.15)$$

Where:

$V_{wp,Ed}$	Shear force in the panel zone as in (6.14)	[kN]
$V_{wb,Rd}$	Buckling resistance of the panel zone	[kN]

For more details, please refer to Appendix F.2.6

Connections

As previously discussed the connections are chosen to be non-dissipative structural elements. This means that the inelastic deformation and consequently the forming of plastic hinges at joints must be avoided.

EN1998-1 [2004] sets special design rules for detailing of connections which ensure their non-dissipative behaviour. Since connections are not part of the delimitation in this project, these design rules are not further investigated, however they are briefly discussed below:

- Since connections must not dissipate energy they should be stronger than the dissipative beam elements. In EN1998-1 [2004] this is achieved by making the connection resistance R_d be a function of the beam resistance R_{fy} . In that relation the following expression must be satisfied: $R_d \geq 1.1\gamma_{ov}R_{fy}$.
- The connections must be sufficiently ductile to allow for the forming of the plastic hinge in the beam and not in the joint. In EN1998-1 [2004] this local ductility condition is controlled by setting a lower boundary of the plastic rotation at the joint $\theta_p = \frac{\delta}{0.5L}$ of 35 mrad for DCH and 25 mrad for DCM (see figure 6.14).

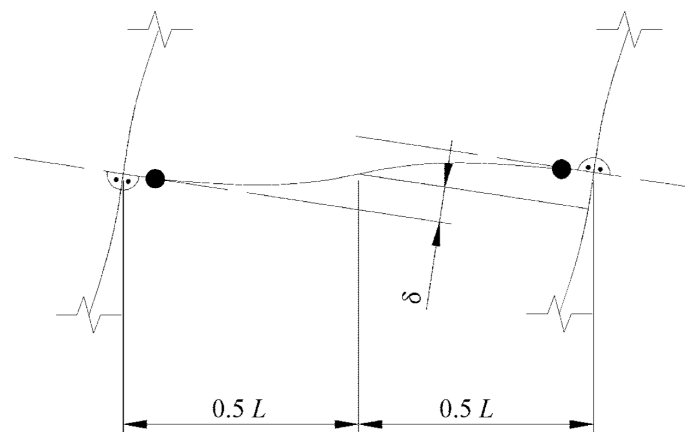


Figure 6.14: Beam deflection for the calculation of θ_p [EN1998-1, 2004]

7 Seismic design situation

The aim of this chapter is to define the seismic load cases and combinations applied on the Prototype structure based on the analysis and design results obtained in chapters 5 and 6. This also chapter summarizes the results obtained from the MRSA and capacity designs of the MRF and CBF. The ULS and SLS capacity checks of the cross sections defined in section 2.3 are also presented.

7.1 Seismic load cases and combinations

Defining the seismic load cases and combinations are not as simple as in regular loads - especially when capacity design is involved. There are many different ways to create the seismic load cases, the chosen of which is explained step-by-step in subsection 7.1.1.

The seismic load combinations are defined separately for the dissipative and non-dissipative elements in subsection 7.1.2 and 7.1.3 respectively. This is done via an iterative procedure in which the capacity design (sections 6.1 and 6.2) is involved.

7.1.1 Load cases

The seismic load cases are obtained in the following two steps:

1. As seen in table 7.1, six seismic cases are defined according to the performed MRSA (Chapter 5). Each of the three pairs is associated with seismic action in x and y direction for the three different eccentricity types - no eccentricity (N/A), X^+Y^+ and X^-Y^- (see section 5.5.2). The responses (deflection, force, etc.) in each case for modes 1 to 5 are combined using the CQC (complete quadratic combination) rule (D.2).
2. Next, each pair is combined by direction using the SRSS (square root of the sum of squares) rule (D.1) to obtain the three seismic cases shown in table 7.2. In this way, the response from both x and y directions are accounted for in one case.

Table 7.1: Step 1: combination by modes (CQC)

Case number	Definition	Direction	Eccentricity type
E_{25}	$CQC(mode1 - 5)$	X	N/A
E_{26}	$CQC(mode1 - 5)$	Y	N/A
E_{28}	$CQC(mode1 - 5)$	X	X^-Y^-
E_{29}	$CQC(mode1 - 5)$	Y	X^-Y^-
E_{31}	$CQC(mode1 - 5)$	X	X^+Y^+
E_{32}	$CQC(mode1 - 5)$	Y	X^+Y^+

Table 7.2: Step 2: combination by direction (SRSS)

Case number	Definition	Direction	Eccentricity type
E_{102}	$SRSS(E_{25}, E_{26})$	XY	N/A
E_{103}	$SRSS(E_{28}, E_{29})$	XY	X^-Y^-
E_{104}	$SRSS(E_{31}, E_{32})$	XY	X^+Y^+

The load combinations are created on the basis of the load cases defined in table 7.2. As previously discussed in sections 6.2.2 and 6.1.2 the internal forces in the non-dissipative elements of the CBF and MRF must be increased according to the capacity design rule in EN1998-1 [2004]. For this purpose it is necessary to differentiate the load combinations depending on what kind of elements they will be applied on:

- Dissipative elements (MRF beams and diagonals) - subsection 7.1.2
- Non-dissipative elements (columns, CBF beams and secondary beams) - subsection 7.1.3

7.1.2 Load combinations: dissipative elements

The three seismic load cases defined in table 7.2 lose their signs (directions) when combined using SRSS. As shown in table 7.3, this is accounted for by multiplying them with 1 and -1 in the combination with vertical loads from the seismic mass m_{dyn} defined in table 5.1. Load combinations 401-406 are used to design the dissipative elements for the lateral (seismic) actions in section 7.2.

Table 7.3: Seismic combinations for dissipative elements

Combination number	Definition	Direction	Eccentricity type
401	$1.0m_{dyn} + E_{102}$	$+XY$	N/A
402	$1.0m_{dyn} - E_{102}$	$-XY$	N/A
403	$1.0m_{dyn} + E_{103}$	$+XY$	X^-Y^-
404	$1.0m_{dyn} - E_{103}$	$-XY$	X^-Y^-
405	$1.0m_{dyn} + E_{104}$	$+XY$	X^+Y^+
406	$1.0m_{dyn} - E_{104}$	$-XY$	X^+Y^+

7.1.3 Load combinations: non-dissipative elements

Referring back to sections 6.1.2 and 6.2.2:

- The factor for multiplying the internal forces in the MRF columns (x -direction) is calculated as **2.72** (6.10).
- The factor for multiplying the internal forces in the CBF columns and beams (y -direction) is calculated as **1.60** (6.4).

In Autodesk Robot [2021] it is not possible to multiply the seismic internal forces, however the factors above can be used to multiply the corresponding seismic loads and create the so called capacity design combinations (CDC) as shown in table 7.4 below. It should be noted that this software limitation leads to more conservative results for the CBF's non-dissipative elements. This is because according to (6.4) only N_{Ed} must be increased but by increasing the seismic actions in the load combination, M_{Ed} and V_{Ed} are also increased.

- Cases 601-606 are used to obtain the CD forces for the columns since they are part of both the MRF and CBF lateral system (xy -direction).
- Cases 701-706 are used to obtain the CD forces for the MRF columns (x -direction)
- Cases 801-806 are used to obtain the CD forces for the CBF beams and columns (y -direction)

Table 7.4: Seismic combinations for non-dissipative elements

Combination number	Definition	Direction	Eccentricity type
601	$1.0m_{dyn} + SRSS(2.72E_{25}, 1.60E_{26})$	+XY	N/A
602	$1.0m_{dyn} - SRSS(2.72E_{25}, 1.60E_{26})$	-XY	N/A
603	$1.0m_{dyn} + SRSS(2.72E_{28}, 1.60E_{29})$	+XY	X^-Y^-
604	$1.0m_{dyn} - SRSS(2.72E_{28}, 1.60E_{29})$	-XY	X^-Y^-
605	$1.0m_{dyn} + SRSS(2.72E_{31}, 1.60E_{32})$	+XY	X^+Y^+
606	$1.0m_{dyn} - SRSS(2.72E_{31}, 1.60E_{32})$	-XY	X^+Y^+
701	$1.0m_{dyn} + SRSS(2.72E_{25}, E_{26})$	+XY	N/A
702	$1.0m_{dyn} - SRSS(2.72E_{25}, E_{26})$	-XY	N/A
703	$1.0m_{dyn} + SRSS(2.72E_{28}, E_{29})$	+XY	X^-Y^-
704	$1.0m_{dyn} - SRSS(2.72E_{28}, E_{29})$	-XY	X^-Y^-
705	$1.0m_{dyn} + SRSS(2.72E_{31}, E_{32})$	+XY	X^+Y^+
706	$1.0m_{dyn} - SRSS(2.72E_{31}, E_{32})$	-XY	X^+Y^+
801	$1.0m_{dyn} + SRSS(E_{25}, 1.60E_{26})$	+XY	N/A
802	$1.0m_{dyn} - SRSS(E_{25}, 1.60E_{26})$	-XY	N/A
803	$1.0m_{dyn} + SRSS(E_{28}, 1.60E_{29})$	+XY	X^-Y^-
804	$1.0m_{dyn} - SRSS(E_{28}, 1.60E_{29})$	-XY	X^-Y^-
805	$1.0m_{dyn} + SRSS(E_{31}, 1.60E_{32})$	+XY	X^+Y^+
806	$1.0m_{dyn} - SRSS(E_{31}, 1.60E_{32})$	-XY	X^+Y^+

7.2 Member capacity check (ULS+SLS)

In order to finalize the design, the ULS capacity of the chosen cross sections must be verified according to EN1993-1-1 [2007]. Moreover, the SLS criteria set in table 2.3 must also be verified. Figures 7.1 and 7.2+7.3 contain the results from the SLS and ULS verification in Autodesk Robot [2021] respectively.

In this relation the following references are provided:

- The member numbers can be seen in Appendix B.1.
- The code groups are the same as the member types shown in Appendix B.2.
- The non-seismic load cases are defined in Appendix B.3, the seismic load cases can be seen in subsection 7.1.1.
- The design parameters of the members (example: buckling length) are defined in Appendix B.2.

Member	Section	Material	Ratio(uy)	Case (uy)	Ratio(uz)	Case (uz)	Ratio(vx)	Case (vx)	Ratio(vy)	Case (vy)
Code group : 1 Columns										
211 Column_1	HEB 400	S 460 N/NL	-	-	-	-	0.00	303 SLS03	0.01	303 SLS03
Code group : 2 CBF beams										
80 Beam_80	IPE 400	S 275	0.00	304 SLS04	0.58	303 SLS03	-	-	-	-
Code group : 3 MRF beams										
28 Beam_28	IPE 360	S 275	0.00	303 SLS03	0.06	303 SLS03	-	-	-	-
Code group : 4 Secondary beams										
323 Beam_323	IPE 270	S 275	0.00	301 SLS01	0.84	303 SLS03	-	-	-	-

Figure 7.1: SLS results

The ULS results are presented in figures 7.2 and 7.3. The following is concluded:

- The choice of cross sections for the columns is dictated by the capacity of their shear panel which is utilized at 96 % (6.15), rather than the member capacity check shown in figure 7.3. This means that adding panel stiffeners could potentially reduce its cross section, however the SCWB criteria (6.11) must also be met.
- As seen in figure 7.2, the highest utilization ratio for the diagonals is 99 %. This not only means that the most efficient cross sections are used but it also reduces Ω_{min} which lowers the internal forces for the validation of the non-dissipative CBF elements as seen in (6.4).
- The leading (design) load combination for the CBF beams is non-seismic (ULS) as shown in figure 7.3. This is expected since the beams are hinged on both sides and no seismic (lateral) induced moment can arise. Moreover, 2/3 of the gravity load is transferred through the CBF as previously discussed in subsection 2.6.1.
- Even though only 1/3 of the gravity load is transferred to the MRF, the leading load combination for the MRF beams is an ULS one (figure 7.3). This is not expected, however their utilization ratio from a seismic combination (ALS) is 90 % which is very close to 93 % (ULS).

Member	Section	Material	Ratio	Case
Code group : 3 MRF beams				
60 Beam_60	☒ IPE 360	S 235	0.63	203 ULS03
Code group : 5 Diagonals_F0				
377 5. Diagonals_377	☒ HSHS 140x140x4	S 235	0.97	405 ASL_3.1
Code group : 6 Diagonals_F1				
378 5. Diagonals_378	☒ HSHS 120x120x4	S 235	0.99	405 ASL_3.1
Code group : 7 Diagonals_F2				
379 5. Diagonals_379	☒ HSHS 100x100x3	S 235	0.87	405 ASL_3.1

Figure 7.2: ULS results: dissipative elements

Member	Section	Material	Ratio	Case
Code group : 1 Columns				
211 Column_1	☒ HEB 400	S 460 N/NL	0.34	605 CD_XY_AS_L_3.1
Code group : 2 CBF beams				
81 Beam_81	☒ IPE 400	S 275	0.92	203 ULS03
Code group : 4 Secondary beams				
333 Beam_333	☒ IPE 270	S 275	0.90	203 ULS03

Figure 7.3: ULS results with capacity combinations: non-dissipative elements

7.3 Conclusion

The linear analysis of the Prototype structure has been performed on a spatial model using the MRSA. It is concluded that all criteria defined in EN1998-1 [2004] in relation to that analysis method are met - drift and damage limitation, sensitivity to second order effects, etc. Moreover, the obtained results are discussed in detail in section 5.5 and certain analytical methods are used to quality check the modal periods and base shear produced by the numerical model. The internal force diagrams generated by the linear computational model in Autodesk Robot [2021] are verified in Appendix B.4.

The capacity design of the CBF and MRF of the Prototype are performed according to the rules in EN1998-1 [2004]. The chosen cross sections and materials for the dissipative and non-dissipative element (section 2.3) ensure adequate ductility and sufficient plastic capacity. In that relation all capacity design criteria set in EN1998-1 [2004] and EN1993-1-1 [2007] are met. However, it is concluded that the MRF beam segment close to the columns is not laterally stable which can cause local instability (LTB) in the beam before it develops plastic hinges (i.e. before it starts dissipating energy). To avoid that, an alternate 'kicker' braces solution is proposed in subsection 6.2.1.

It is concluded that by using the MRSA, the response of the Prototype structure has been depicted with sufficient accuracy and well understood. The output from the linear numerical model has been quality assured and the results do not deviate from what is expected. The chosen cross sections provide adequate ductility and energy dissipation properties of the structure. Their plastic capacity ensures the development of the wanted yielding mechanism. Their capacity check according to EN1993-1-1 [2007] is provided in the following section 7.2.

IV Prototype response assessment through Pushover analysis

8	Pushover analysis	79
8.1	Introduction	
8.2	Non-linear computational models	
8.3	Constitutive model	
8.4	Loads and mass	
9	Non-linear response	89
9.1	Preliminaries	
9.2	MRF pushover curve	
9.3	CBF pushover curve	
9.4	Conclusion	
10	Discussion	101
	Bibliography	111

8 Pushover analysis

This chapter describes the parameters used to perform the non-linear static (Pushover) analysis (section 4.3) on the Prototype structure. These parameters include the non-linear computational and constitutive models, and the applied loads. Arguments are provided for the choice of each of them.

8.1 Introduction

Since the Prototype structure is regular both in height and elevation, according to EN1998-1 [2004], it is possible to perform the Pushover analysis on two planar models of the lateral restraining systems (LRS) in both orthogonal directions - MRF (x -direction) and CBF (y -direction). This is a reasonable simplification based on the fact that the mass and stiffness are distributed evenly in regular structures - torsional modes are not a problem. Additionally, the rigid diaphragm behaviour of the slab causes the same in-plane response of each LRS.

Next it should be decided what kind of non-linearities will be considered in the non-linear analysis. Only the following two types are included:

- **Geometrical** - this is the $P - \Delta$ effect causing secondary moments in structural members arising from the deformed shape of the structure. This is taken care of by choosing appropriate elements in the computational model which are able to simulate this type of non-linearity - see section 8.2.
- **Material** - with increase of stress in the material, the stress-strain relationship (modelled by the Young's Modulus) stops being linear. This non-linearity is modelled by choosing a suitable constitutive model in section 8.3.

The final step is to choose the lateral load distribution (see section 8.4) and verify the response of the structure.

8.2 Non-linear computational models

The non-linear computational model is executed in SeismoStruct [2022]. Two planar (2D) models are created in the XZ plane for the LRS in each orthogonal direction (i.e. for MRF and CBF) - see figures 8.1 and 8.2 below. The member and node numbers can be seen in Appendix C.1.

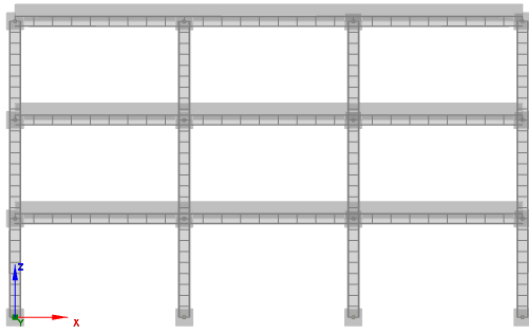


Figure 8.1: MRF planar non-linear computational model

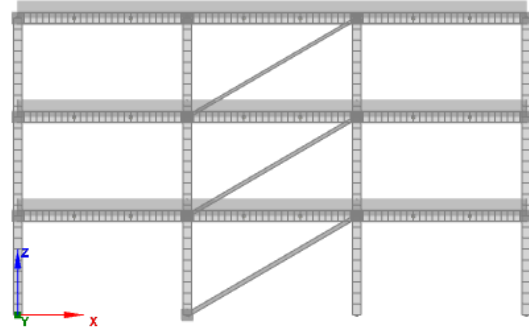


Figure 8.2: CBF planar non-linear computational model

- The same cross sections are used as in the linear model in Robot - see section 2.3.
- The used constitutive model is discussed in section 8.3.
- The same boundary conditions are used as for the linear model in Robot. They are discussed in subsection 8.2.1.
- The element types used to simulate the geometrical and material non-linearity are described in subsection 8.2.2.
- The computational model is verified by comparing the modal analysis results and internal force diagrams to those obtained from the linear model in Robot. See subsection 8.2.3 for more details.
- The maximum iteration and convergence tolerances are set differently for both models to avoid numerical instability.

8.2.1 Boundary conditions

The boundary conditions in SeismoStruct are the same as defined in the linear model created in Autodesk Robot [2021] (see section 2.6). However, due to the nature of SeismoStruct [2022] it is necessary to further discuss how the diaphragm is simulated and how a moment release is defined.

Simulation of the diaphragm

Even though a planar model is used in SeismoStruct, the out of plane DoF is not restrained. Since the slab acts as a diaphragm, it is reasonable to assume that the out of plane movement of the 2D models is restricted. For this purpose the movement in y -direction at each beam-column connection for both the MRF and CBF models is restrained. This is necessary to ensure the same structural response (ex. natural periods) as in the linear model and figure 8.3 below illustrates that. The contribution of the diaphragm to the structural response is clearly visible when looking at the obtained natural periods.

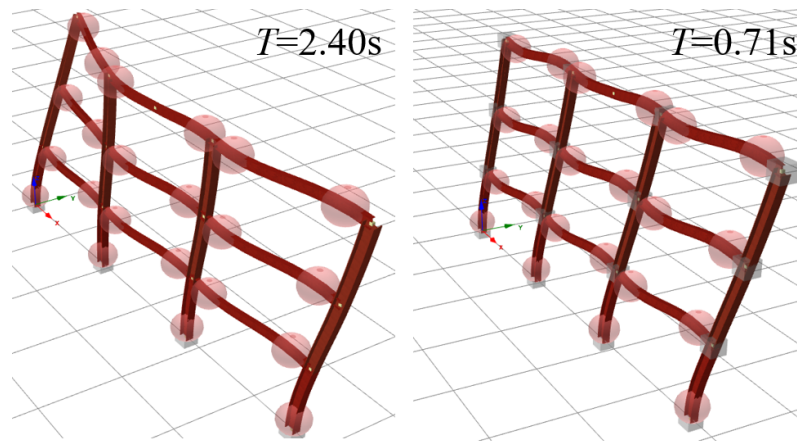


Figure 8.3: MRF response before (left) and after (right) simulating the diaphragm

Definition of a moment release in the CBF model

When performing a non-linear analysis in SeismoStruct it is not possible to fully release rotation (i.e define a moment release/hinge) since it causes numerical instability. Instead this is simulated by assigning the corresponding node with a symmetric force/displacement or moment/rotation curve, the slope of which is the stiffness K_0 of the joint - see figure 8.4. For displacements it is defined as infinitely large ($K_0 = 1E + 13$) and for rotation - infinitely small ($K_0 = 1E - 13$).

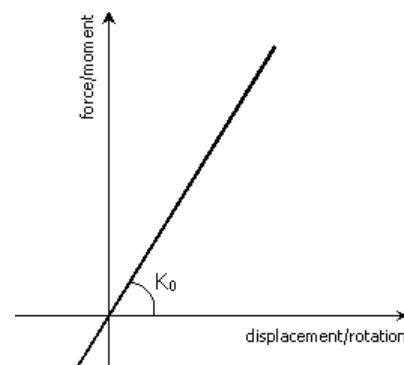


Figure 8.4: Curve parameter for a joint [SeismoStruct, 2022]

8.2.2 Element types

Each element is discretized along its section to 150 section fibres using triangular mesh elements. Every element split its length in 5 integration (calculation) sections. All of this is decided after performing a brief convergence study on both models.

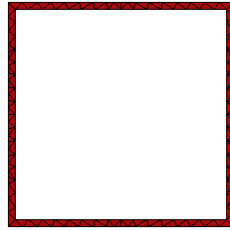


Figure 8.5: Discretization of SHS profile section - 150 fibers [SeismoStruct, 2022]



Figure 8.6: Discretization of HE profile section - 150 fibers [SeismoStruct, 2022]

The diagonals in SeismoStruct are modelled as tension only elements (as in the linear model). The element type that best represents this behaviour in SeismoStruct is the inelastic truss element *truss* shown in figure 8.7. It is common to model both the compressive and tensile diagonal during a non-linear analysis. However, to model accurately the buckling behaviour of the compressive one requires extensive study which is out of the scope of this Thesis. Moreover, its contribution to the global response is insignificant since it is designed to buckle according to the capacity design rule.

All beams and columns are modelled with inelastic force-based frame element defined as *infrmFB* in SeismoStruct (see figure 8.8). This element is capable of modelling both material and geometrical non-linearities. It considers the spread of inelasticity along the member length and across its cross-section making it one of the most accurate element types to use.

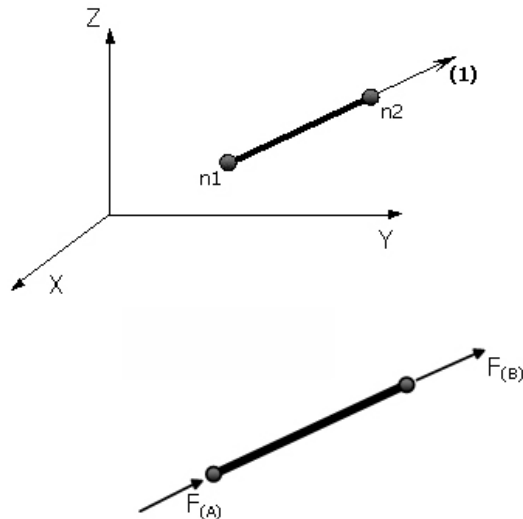


Figure 8.7: truss element [SeismoStruct, 2022]

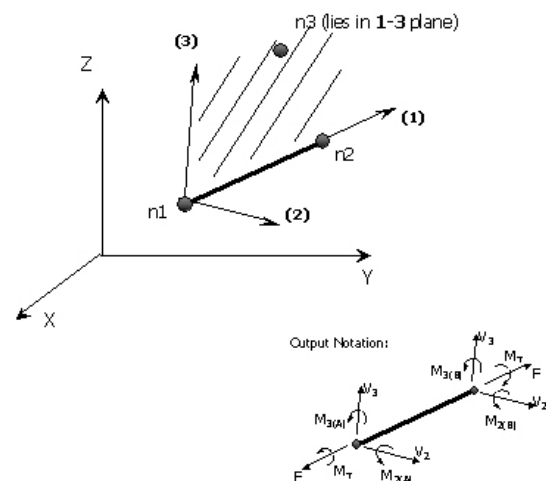


Figure 8.8: infrmFB element [SeismoStruct, 2022]

8.2.3 Model verification

The best way to verify the numerical model in SeismoStruct is to compare its linear results to the ones obtained from the already verified linear computational model in Robot (section 5.2). This is done by looking into the following two:

- Internal force diagrams for a load factor of $LF = 0$ (only vertical forces) - see subsection 8.4.2 and Appendix C.4
- Fundamental periods - see below and table 8.1

Using the fundamental mode shape periods T is a way to verify both the mass m and stiffness k of the planar models since $T = f(k, m)$. As seen in table 8.1, there is a small difference in the fundamental periods calculated in the spatial Robot model and 2D SeismoStruct models.

Table 8.1: Fundamental mode shape periods from the different computational models

Computational model	MRF	CBF
	T_1 [s]	T_2 [s]
Robot (3D)	0.67	0.55
SeismoStruct (2D)	0.71	0.60
Robot (2D)	0.71	0.60

One of the reasons behind this is that the response of the spatial model has contribution from both orthogonal directions i.e. the modal period is not exclusively obtained for one direction. Another reason is that the 3D model uses lumped mass (see section 5.2), whereas the mass in the 2D one is considered uniformly distributed (see subsection 8.4.1). In order to confirm this, a 2D model is created in Robot using the same properties as the 2D model in SeismoStruct and as seen in table 8.1 the results are identical. This proves that the difference in the periods is caused only by m and not k . Since m does not impact the results from the Pushover analysis it is decided to accept the deviation in T between the spatial and planar models.

8.3 Constitutive model

The non-linear behaviour of the steel is modelled using a **bi-linear steel model with kinematic strain hardening**. This model is chosen since it is simple, captures sufficiently accurate the elastic and plastic stages of the material and it is not computationally intensive. It should be noted that more precise steel constitutive models exist (ex: Menegotto-Pinto) but they require experimental testing to determine their relevant parameters. Choosing the way the yield surface changes (i.e isotropic or kinematic hardening) is of no importance since the load is applied only in one direction and no hysteresis curves are produced. The kinematic model is less computationally intensive and this is the reason for choosing it.

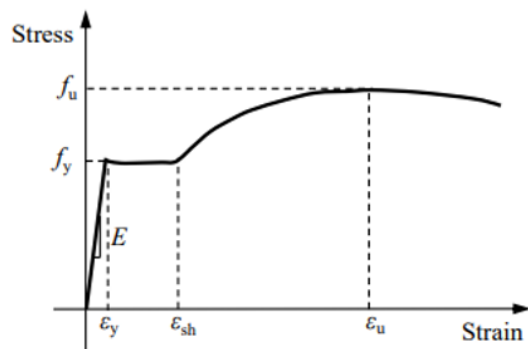


Figure 8.9: Typical engineering stress-strain curve of hot-rolled carbon steel [Yun and Gardner, 2017]

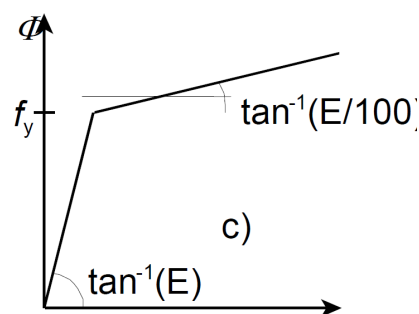


Figure 8.10: Bi-linear stress-strain curve with strain hardening [EN1993-1-5, 2006]

As seen in figure 8.10 above, the plastic Young's Modulus is determined as $E_p = E/100$ following the recommendations in EN1993-1-5 [2006]. In SeismoStruct [2022] this model is called *stl_bl*.

The main limitation of the chosen constitutive model is that the strain development between the ultimate ϵ_u and fracture strain ϵ_f cannot be tracked. As seen in figure 8.9 the strain can still increase after ϵ_u but the stress decreases. This is why it is assumed that when ϵ_u is reached, the material fractures i.e. $\epsilon_u = \epsilon_f$.

The only way to obtain the true (engineering) stress-strain relationship for the used steel grades is by performing a tensile lab test. Since such information is not available, assumptions must be made relying on previous experience. After consultation with the company supervisor, the following parameters are assumed: (see table 8.2 and figures 8.11 to 8.11):

- **S235:** f_y is increased by 30 %, the lower bound for f_u is used
- **S275:** f_y is increased by 25 %, the lower bound for f_u is used
- **S460:** as a conservative assumption the lower bound values for f_y and f_u are used (the impact of member thickness is taken into account)

Table 8.2: Assumed steel material parameters for the non-linear analysis

Steel	Yield strength	Ultimate strength	Yield strain	Ultimate strain	Young's modulus	
	f_y [MPa]	f_u [MPa]	$\epsilon_y = f_y/E$ [-]	$\epsilon_u = (f_u - f_y)/E_p$ [-]	E [MPa]	E_p [MPa]
S235 JR	305.50	360.00	0.00145	0.02595	210000	2100
S275 JR	343.75	410.00	0.00164	0.03155	210000	2100
S460 N/NL	440.00	540.00	0.00210	0.04762	210000	2100

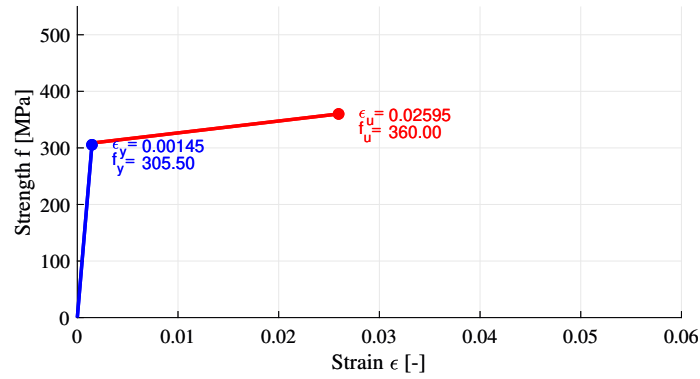


Figure 8.11: Used stress-strain relationship for S235 JR

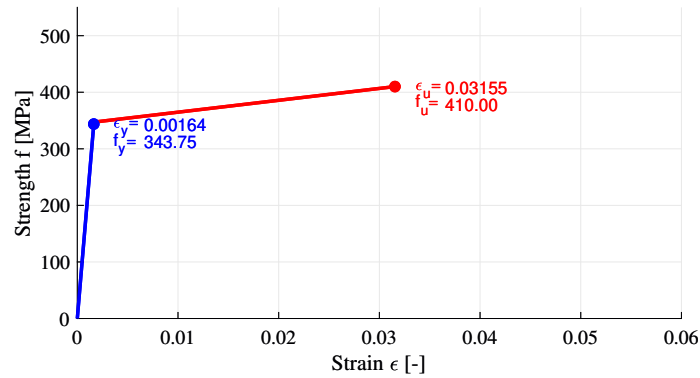


Figure 8.12: Used stress-strain relationship for S275 JR

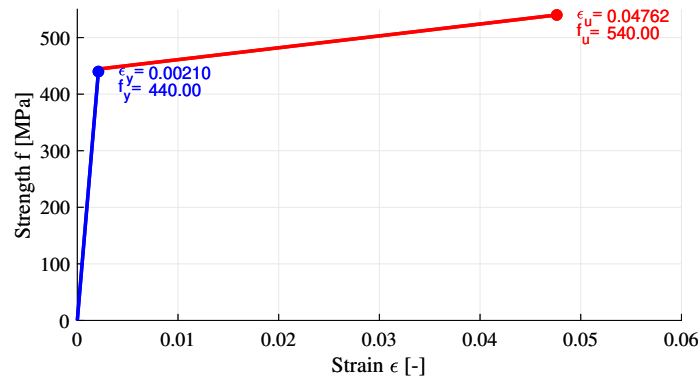


Figure 8.13: Used stress-strain relationship for S460 N/NL

8.4 Loads and mass

8.4.1 Mass definition

One must not confuse the mass with the vertical (gravity) load. The mass generates the inertia forces during an earthquake and is the same in both orthogonal directions - $m_{dyn} = 775$ t (table 5.1). The vertical (gravity) loads also originate from m_{dyn} but their size depend on the chosen load distribution for the MRF and CBF - see later in subsection 8.4.2.

Since a rigid diaphragm is used and since each of the four bays in x and y directions have the same stiffness, it is safe to assume that the CBF and MRF 2D models will generate inertia force from $m_{dyn,i}/4$ as shown in table 8.3.

Table 8.3: Mass in 2D Pushover model

Storey	Mass (spatial model)	Mass (2D models)	
i	$m_{dyn,i}$	$m_{dyn,i}/4$	
-	[t]	[t]	[t/m]
1	265	66.25	3.681
2	265	66.25	3.681
3	245	61.25	3.403
Σ	775	193.75	

In SeismoStruct [2022] the mass is considered as a separate entity and it is not included as part of the vertical (gravity) load on the 2D models. It is applied as linearly distributed element on the beams and is marked in green in figure 8.14. The mass is only used to verify the modal periods T_1 and T_2 by comparing them to the ones obtained from the modal analysis of the spatial model - see subsection 8.2.3.

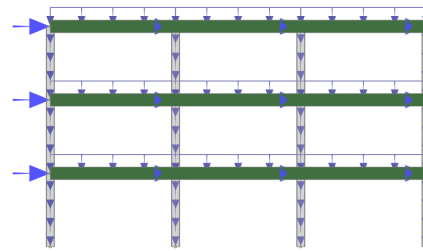


Figure 8.14: Distributed mass element on each storey of the MRF (marked in green)

8.4.2 Vertical (gravity) load

In comparison to the lateral load (subsection 8.4.3), the vertical one remains constant when increasing the load factor. Its main purpose is to simulate the $P - \Delta$ effects and because of this it is important to accurately represent it in the 2D SeismoStruct model

The vertical (gravity) loads are generated from the dynamic (seismic) mass load combination as shown in (8.1) below. The way they are applied on the MRF and CBF 2D models in SeismoStruct can be seen in Appendix C.2

$$m_{dyn} = 1.0kG + 0.4kS1 + 0.24kQ2 \tag{8.1}$$

To ensure that the $P - \Delta$ effect are simulated properly during the non-linear analysis a quality check is performed on the axial forces N_{Ed} in the columns. This is done by comparing the N_{Ed} diagrams generated from SeismoStruct 2D model (figure 8.15) to the ones from Robot 3D model (figure 8.16). Table 8.4 contain a summary of the results. It is concluded that the diagrams are identical and therefore the vertical loads applied in SeismoStruct (Appendix C.2) are correct. The same comparison is made for the moment diagrams and can be found in Appendix C.4.

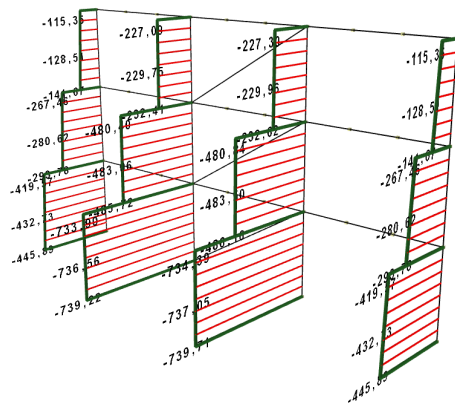


Figure 8.15: Axial force diagrams in columns from seismic mass load combination [SeismoStruct, 2022]. Load factor = 0



Figure 8.16: Axial force diagrams in columns from seismic mass load combination [Autodesk Robot, 2021]

Table 8.4: Quality assurance: axial forces in the side and middle columns in both models

Storey <i>i</i>	Side 3D	Side 2D	Middle 3D $N_{Ed,i}$ [kN]	Middle 2D
3	115	115	228	227
2	268	268	482	481
1	420	420	736	735
base	446	446	741	740

8.4.3 Lateral (incremental) load

The Pushover analysis in EN1998-1 [2004] considers two different lateral load distributions methods as shown in figure 8.17. In order to plot the capacity curve (right part of figure 8.17) the lateral load is constantly increased by a load factor in SeismoStruct [2022]. Both methods are investigated and the method that yields the most conservative results (displacement, base shear) is used.

The applied lateral loads using methods 1 and 2 on both 2D models (MRF and CBF) in SeismoStruct [2022] can be seen in Appendix C.3. An example using method 1 for the MRF can be seen in figure 8.18. It should be noted that the numerical value of the load is not important however its ratio along the stories is is.

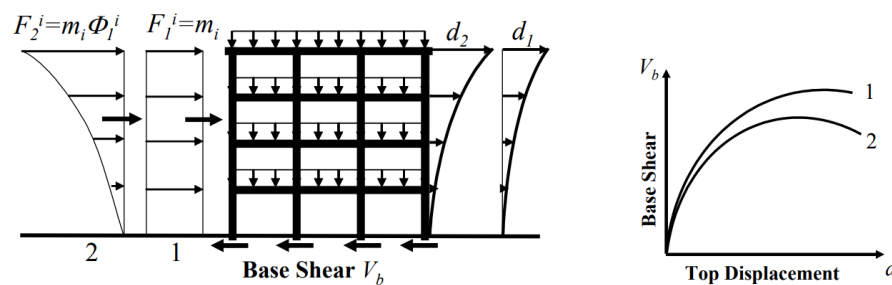


Figure 8.17: EN1998-1 [2004] methods for distributing the incremental loads along the stories during a Pushover analysis [Spacone et al., 2010]

- **Method 1 - mass proportional distribution** - the lateral load F_1^i is proportional to the mass m_i of each storey i . This is under the assumption that the acceleration is constant along the height of the structure.
- **Method 2 - modal load distribution** - the distribution of the acceleration (and therefore lateral load F_2^i) is considered proportional for the fundamental mode shapes in each orthogonal direction - mode shape 1 for MRF (x -direction) and mode shape 2 for CBF (y -direction). The fundamental mode shapes are represented by the normalized modal displacement Φ_1^i (mode 1) and Φ_2^i (mode 2).

According to EN1998-1 [2004], the lateral loads F^i should be applied in the center of mass of each storey i . In SeismoStruct [2022], the F^i are applied at the crossing point between beams and columns as shown in figure 8.18. In this way a more uniform distribution is achieved simulating better the diaphragm function of the slab.

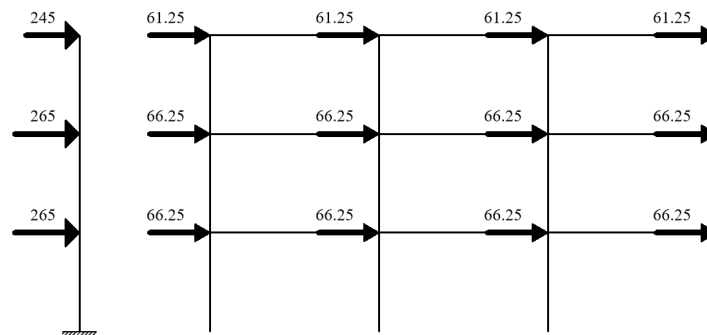


Figure 8.18: Example: method 1 lateral load distribution on the MRF. Load factor = 1

9 Non-linear response

This chapter presents the results from the Pushover analysis performed on the two planar models - CBF and MRF. The chapter is concluded with the most important parameters concerning the choice of actuators for the RWSF facility.

9.1 Preliminaries

Before looking into the non-linear response of the two planar models documented in sections 9.2 and 9.3 it is necessary to document the preliminary choices regarding:

- The location of the control node
- The used criteria
- The used load distribution

All of the above mentioned dictate to a large extent the non-linear response produced by the Pushover analysis. Thereby, all three of them are discussed in details in the following three sub-sections.

9.1.1 Choice of control node

The control node *CN* is used to derive the displacement for the capacity curve (*CN* displacement - base shear). This is why it is important to locate it in a place where it can depict the the maximum lateral displacement of the planar models. According to EN1998-1 [2004] the *CN* must be located in the center of mass *CM* of the last storey since it exhibits the largest lateral deformation. However, because the slab is modelled as a rigid diaphragm, the location of the *CN* does not matter since its displacement is the same as for all the nodes on the corresponding storey. It is therefore decided to locate the *CN* at the end of the rightmost element on storey 3 as shown in figure 9.1.

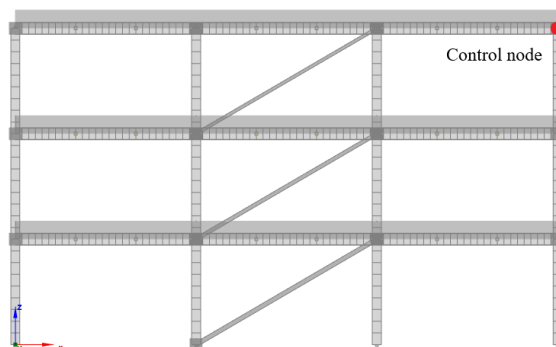


Figure 9.1: Location of control node in the CBF (same for MRF).

9.1.2 Choice of criteria

Criteria are essentially conditions which when reached change the behaviour of the elements in the non-linear numerical model. Since the constitutive model (section 8.3) describes best the change of this behaviour, two conditions are used: yield and fracture i.e. when the material starts to behave inelastically and when it breaks.

For the MRF planar model the yield and fracture strain in the material are used as shown in table 9.1 (see also table 8.2). Using the internal forces for the MRF elements is not a viable option because the stress combination resulting from the bending moment, axial and shear forces would not be accurately represented.

Table 9.1: Yield and fracture criteria for MRF beams & columns

MRF element	Cross section	Material	Yield criteria	Fracture criteria
Beams	HEB400	S275 JR	$\epsilon = 0.00164$	$\epsilon = 0.03155$
Columns	IPE360	S460 N/NL	$\epsilon = 0.00210$	$\epsilon = 0.04762$

The most important elements for the lateral stability of the CBF are the diagonals which are allowed to develop only tensile axial forces as discussed in subsection 8.2.2. For this reason it is decided to use the axial forces $N_{Ed,pl} = f_y A$ and $N_{Ed,f} = f_u A$ to set the yield and fracture criteria respectively - see table 9.2 below (see also table 8.2).

Table 9.2: Yield and fracture criteria for CBF diagonals

Storey	Cross section	Material	Yield criteria	Fracture criteria
3	CF SHS 100x3	S235 JR	$N_{Ed} = 348.30$	$N_{Ed} = 410.40$
2	CF SHS 120x4	S235 JR	$N_{Ed} = 553.00$	$N_{Ed} = 651.60$
1	CF SHS 140x4	S235 JR	$N_{Ed} = 650.70$	$N_{Ed} = 766.80$

9.1.3 Choice of lateral load distribution

Figures 9.2 and 9.3 below illustrate the capacity curves for MRF and CBF respectively using the two lateral load distribution methods discussed in subsection 8.4.3. Method 1 is chosen since it provides larger values for the base shear and control node displacement for both MRF and CBF. This is because:

- The lateral load distribution according to method 1 allows the structures to develop larger base shear. In a RWSF experiment, this means that the actuator must apply more force and therefore have larger capacity.
- Method 1 results in a more numerically stable solution since it allows for the control node displacements to develop further. This requires larger actuator stroke during a RWSF experiment.

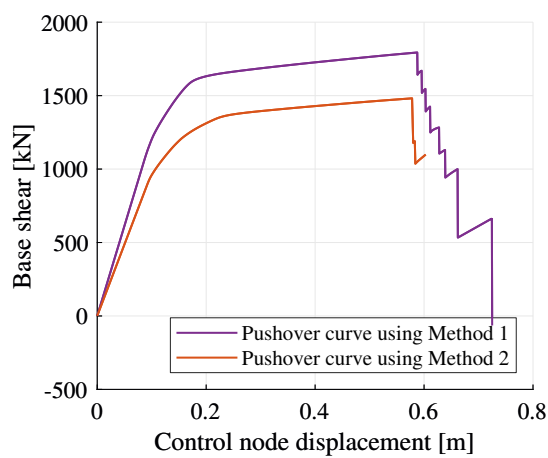


Figure 9.2: MRF pushover curves for load distribution methods 1 and 2

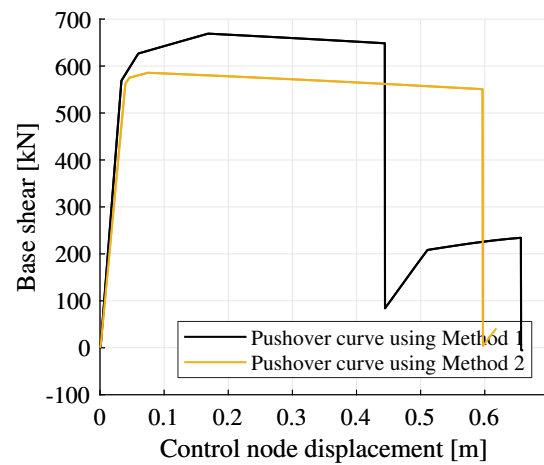


Figure 9.3: CBF pushover curves for load distribution methods 1 and 2

It should be noted here that in many numerical simulations collapse is assumed when 20 % of the capacity (base shear) is left. However, as seen in figures 9.2 and 9.3 above it is decided to 'push' the MRF and CBF until numerical instability or structural collapse is reached. This is done to achieve larger *CN* displacement which would correspond to necessity for larger actuator stroke.

9.2 MRF pushover curve

The MRF pushover (capacity curve) is shown in figure 9.4. Four distinct phases of the curve can be seen in the figure, the parameters of which are summarized in table 9.3 and discussed below:

1. The elastic behaviour of the MRF ends at the point where the first plastic hinge develops in beam bm_{x1} (i.e. it reaches ϵ_y) - figure 9.6. From this point onward bm_{x1} has a Young's Modulus of $E = 2100\text{MPa}$ obeying to the constitutive model discussed in section 8.3.
2. The full plastic mechanism in the MRF is formed when all beams and column bases have formed a plastic hinges (i.e. their strain is equal to ϵ_y) - figure 9.11. Exactly this type of mechanism has been targeted by the capacity design performed earlier in section 6.2. Therefore, it is concluded that the design has been correctly executed and the desirable plastic mechanism in the MRF has been achieved: strong column - weak beam concept (see figure 6.11).
3. Once ϵ_u has been reached in the first element (bm_{x1}), it fractures and can no longer sustain forces - see figure 9.13. The forces are redistributed in the rest of the MRF elements that still have capacity left. The first fracture point marks the theoretical maximum base shear that the MRF can sustain - $F_b = 1794\text{kN}$.
4. The structural collapse happens either when numerical instability in the model is reached or when the equilibrium is violated. Figure 9.20 illustrates the collapse state of the MRF and it can be seen that this happens when the leftmost beams and column base fracture. The collapse point marks the maximum theoretical CN displacement that the MRF can sustain - 0.724m .

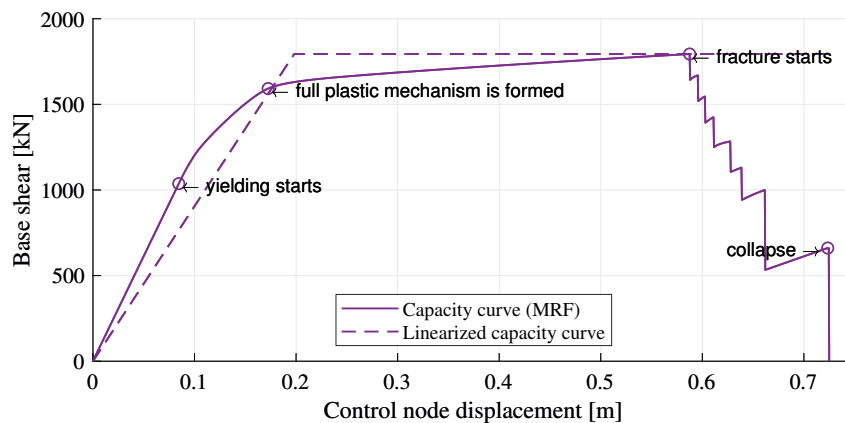


Figure 9.4: MRF capacity curve overview

9.2.1 Yield stages

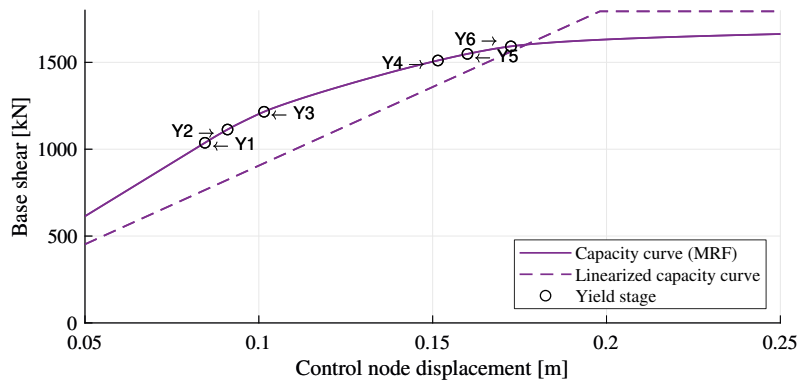


Figure 9.5: MRF capacity curve: yield stages

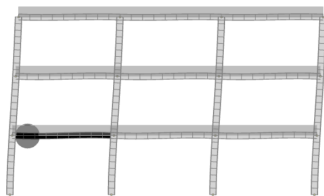


Figure 9.6: Yield stage Y1

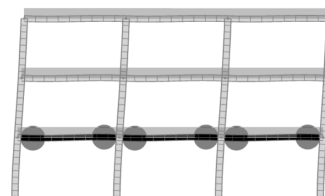


Figure 9.7: Yield stage Y2

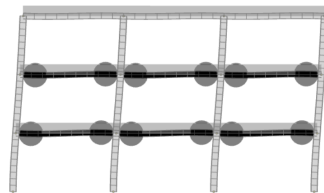


Figure 9.8: Yield stage Y3

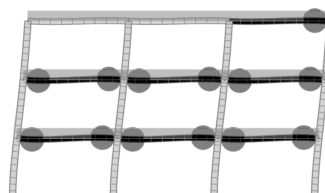


Figure 9.9: Yield stage Y4

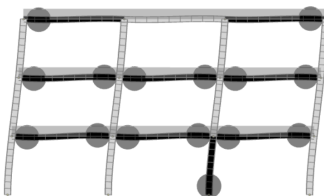


Figure 9.10: Yield stage Y5

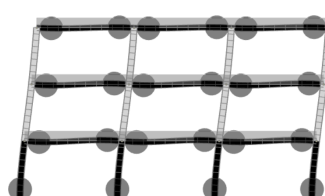


Figure 9.11: Yield stage Y6

9.2.2 Fracture stages

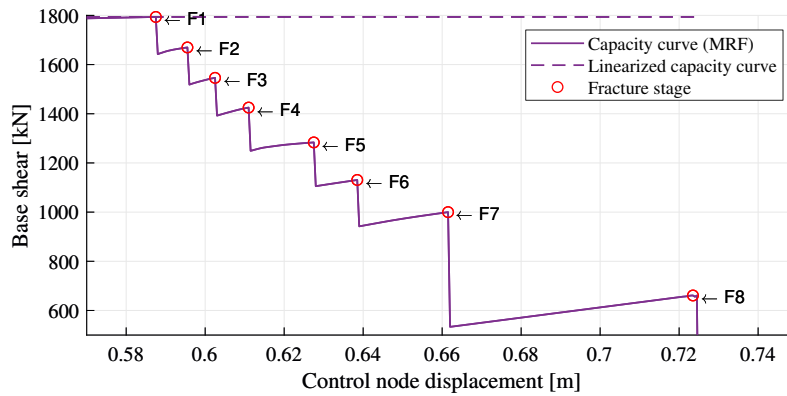


Figure 9.12: MRF capacity curve: fracture stages

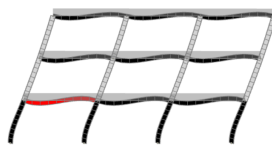


Figure 9.13: MRF fracture stage F1

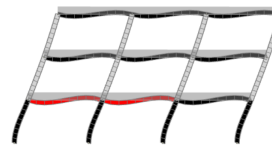


Figure 9.14: MRF fracture stage F2

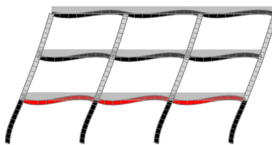


Figure 9.15: MRF fracture stage F3

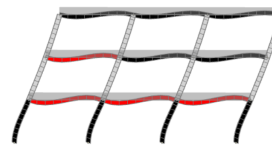


Figure 9.16: MRF fracture stage F4

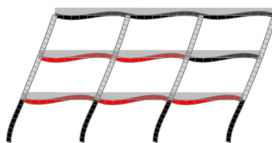


Figure 9.17: MRF fracture stage F5

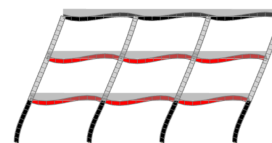


Figure 9.18: MRF fracture stage F6

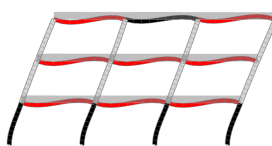


Figure 9.19: MRF fracture stage F7

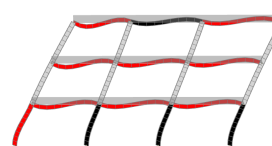


Figure 9.20: MRF fracture stage F8

9.3 CBF pushover curve

The CBF pushover (capacity curve) is shown in figure 9.21. Four distinct phases of the curve can be seen in the figure, the parameters of which are summarized in table 9.4. The diagonals on storey 3,2 an 1 - $D1$, $D2$ and $D3$ mainly contribute to the lateral stiffness of the CBF. Therefore, looking into their axial force - displacement diagrams illustrated in figure 9.22, provides insight to the CBF capacity curve illustrated in figure 9.21.

As seen in figure 9.22, all diagonals reach the yield criteria discussed in subsection 9.1.2 but only $D2$ and $D3$ reach fracture since numerical instability happens before $D1$ to reaches fracture. However, looking at figures 9.25 to 9.30, one can notice that all beams and columns remain within their elastic range throughout the entire loading phase. This is expected as no moment develops in them since they are hinged to each-other and the column bases are pinned to the foundation. Once all diagonals yield (plastic mechanism is formed) the maximum base shear is recorded at $F_b = 669\text{kN}$. As seen in figure 9.22, the fracture phase starts with fracture in $D1$ causing force redistribution and base shear decrease which also means reduced axial forces in $D2$ and $D3$. Having no diagonal on storey 1 causes the storey shear to be transferred to the foundation through the columns which reduces significantly the stiffness of the CBF as seen in figure 9.21. Looking at figures 9.22 and 9.21 one can observe that $D2$ experiences secondary yield (illustrated in figure 9.29) after which it fractures causing numerical instability in the model at a CN displacement of 0.66 m.

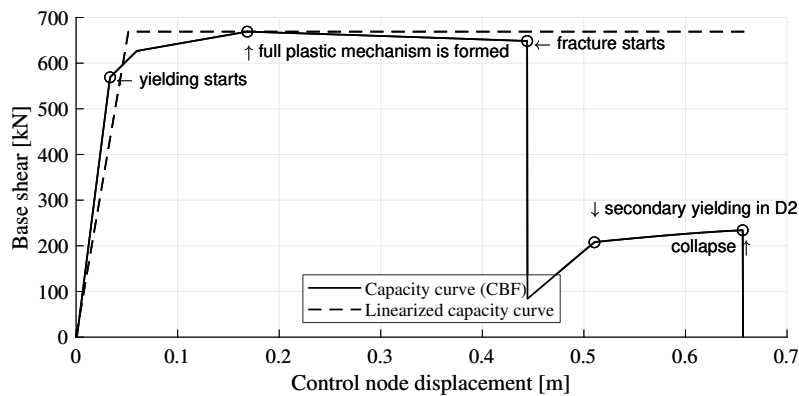


Figure 9.21: CBF capacity curve overview

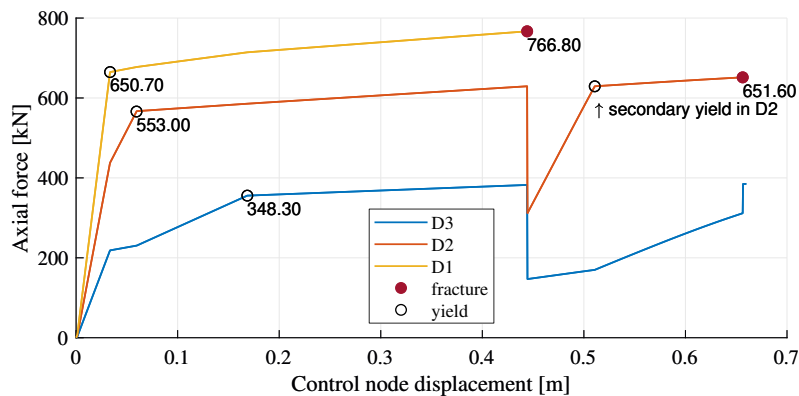


Figure 9.22: Axial force - displacement diagram for all CBF diagonals in the same time domain.

9.3.1 Yield and fracture stages

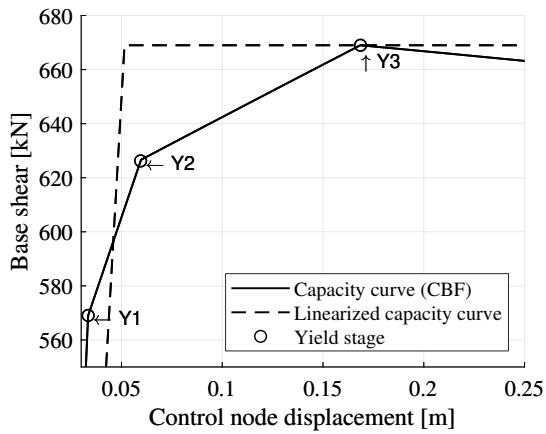


Figure 9.23: CBF capacity curve: yield stages

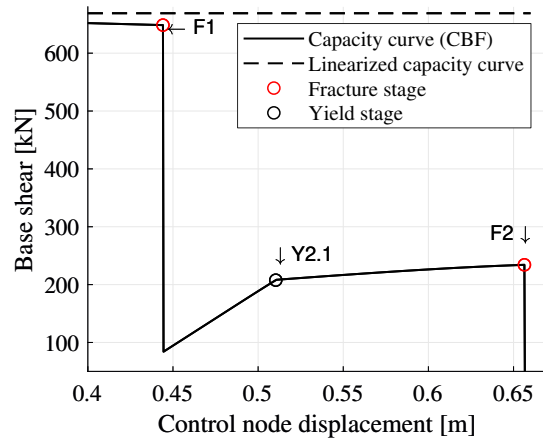


Figure 9.24: CBF capacity curve: fracture stages and secondary yield in diagonal on storey 2

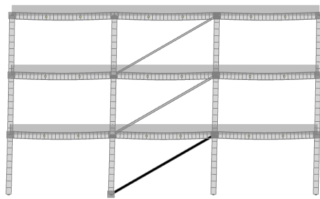


Figure 9.25: CBF yield stage Y1

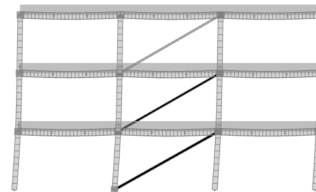


Figure 9.26: CBF yield stage Y2

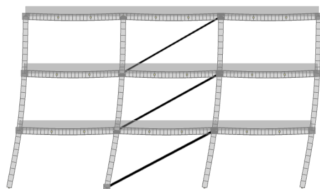


Figure 9.27: CBF yield stage Y3

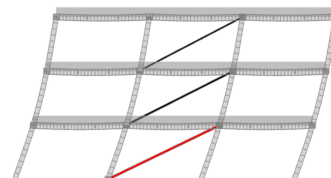


Figure 9.28: CBF fracture stage F1

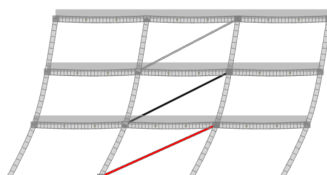


Figure 9.29: CBF yield stage Y2.1

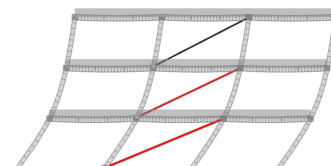


Figure 9.30: CBF fracture stage F2

9.4 Conclusion

The conclusion aims at summarizing the most important results produced from the Pushover analysis concerning the choice of actuator parameters and the design of the RWSF facility. It also includes a short discussion on the obtained results.

Both MRF and CBF capacity curves are plotted next to each-other in figure 9.31 on the right. Looking at their elastic portion it is visible that the CBF has a higher elastic stiffness compared to the MRF. This is expected since the same was concluded during the linear MRSA analysis in subsection 5.5.1. Both MRF and CBF exhibit a very ductile behavior, however, the MRF can sustain higher base shear and larger CN displacement. This is because in the MRF all columns and beams contribute to its lateral capacity and stiffness, on the other hand, the lateral stability of the CBF is provided mainly by its three tensile diagonals.

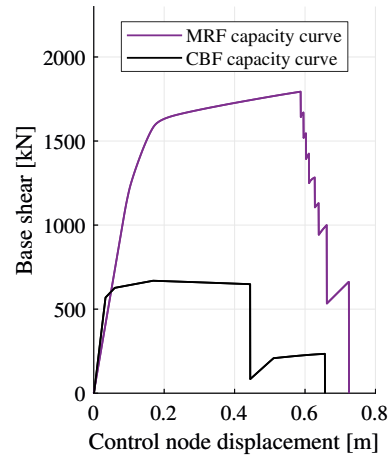


Figure 9.31: MRF and CBF pushover curves

Tables 9.3 and 9.4 below summarize the parameters of the main stages for MRF and CBF respectively.

Table 9.3: Parameters for the main stages of the MRF capacity curve

Stage	Load factor LF	Base shear F_b [kN]	Control node displ. d_{cn} [m]	Reference to illustration
Start of yielding	1.338	1037	0.085	Figure 9.6
Full plastic	2.054	1592	0.173	Figure 9.11
Start of fracture	2.315	1794	0.588	Figure 9.13
Collapse	0.854	661	0.724	Figure 9.20

Table 9.4: Parameters for the main stages of the CBF capacity curve

Stage	Load factor LF	Base shear F_b [kN]	Control node displ. d_{cn} [m]	Reference to illustration
Start of yielding	0.734	569	0.035	Figure 9.25
Full plastic	0.863	669	0.169	Figure 9.27
Start of fracture	0.837	649	0.444	Figure 9.28
Collapse	0.302	234	0.656	Figure 9.30

It is assumed that during a RWSF experiment the actuators will be attached to the leftmost columns of the MRF and CBF. This is why it is important to look at the displacements illustrated in figures 9.32 and 9.33 rather than the ones in the *CN* (tables 9.3 and 9.4) when choosing the necessary actuator stroke. It is vital to note that the obtained displacements obey to the used constitutive model (section 8.3) which assumes fracture when the ultimate stress is reached. In reality this is not the case which raises a level of uncertainty in the displacement results. This is why the first element fracture is set as a lower bound for the displacements and the total collapse - upper bound.

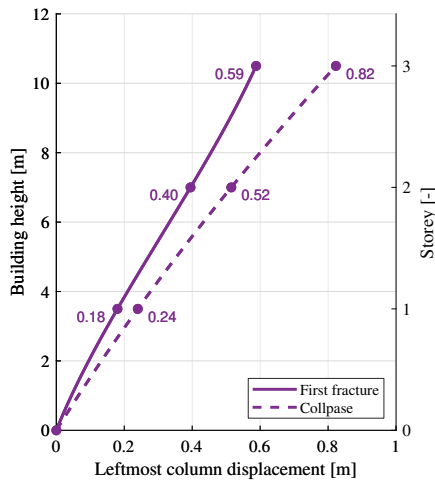


Figure 9.32: Displacement in the leftmost MRF column

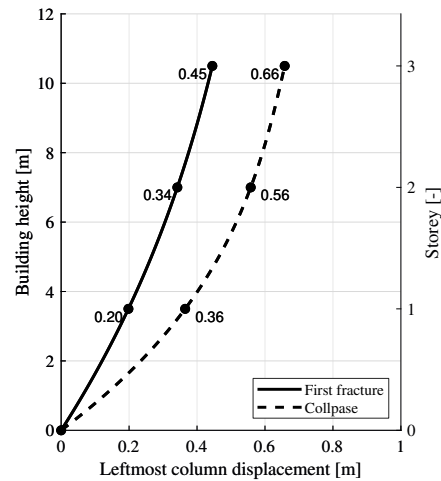


Figure 9.33: Displacement in the leftmost CBF column

Figures 9.34 and 9.35 below illustrate the maximum force on each storey, the summation of which result in the maximum base shear each structure can sustain. These forces reflect the necessary actuator capacity. In contrast to the values obtained for the *CN* displacement the uncertainty in the force is a lot smaller. This is because in both the used and realistic constitutive models, the ultimate force is the point where the material cannot sustain larger forces.

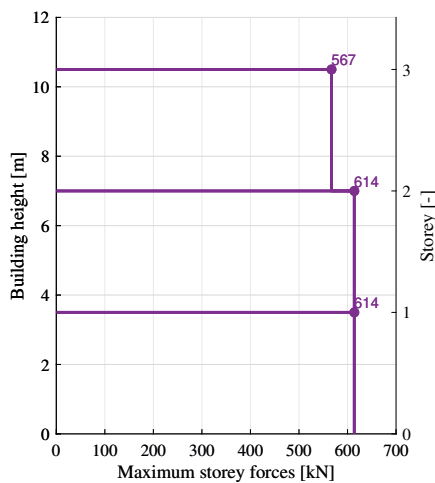


Figure 9.34: Storey forces for 1 MRF obtained from the maximum base shear from the pushover curve

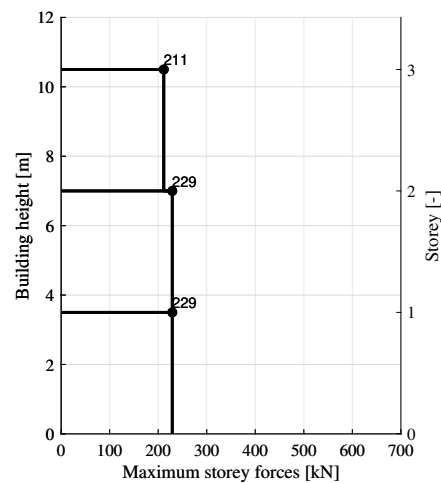


Figure 9.35: Storey forces for 1 CBF obtained from the maximum base shear from the pushover curve

Figure 9.36 below illustrates the response of a RWSF assembly due to a applied unit force. Since the reaction wall and strong floor are typically designed as one structural entity, obtaining the design loads on it requires considering the worst load combination arising from:

- The forces applied from the actuator to the reaction wall as shown in figure 9.34.
- The maximum (or total) reactions of the Prototype on the strong floor shown in tables 9.5 and 9.6.

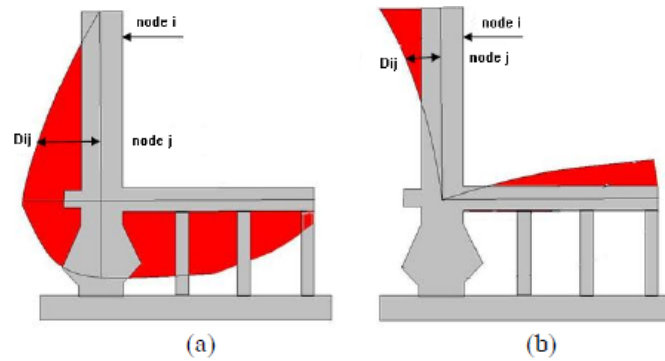


Figure 9.36: Response of reaction wall-floor assembly due to unit force (a) stress (b) displacement [Rai et al., 2014]

Table 9.5: Maximum reactions at the column bases (MRF planar model)

Reaction type	Maximum value	Node	Total value
Vertical F_z	860 kN	n031	2405 kN
Horizontal F_x	563 kN	n011	-1794 kN
Bending moment M_y	-1607 kNm	n031	-6385 kNm

Table 9.6: Maximum reactions at the column bases (CBF planar model)

Reaction type	Maximum value	Node	Total value
Vertical (compression) F_z	1636 kN	n031	2371 kN
Vertical (tension) F_z	-157 kN	n021	N/A
Horizontal F_x	-685 kN	n021	-669 kN

10 Discussion

This chapter contains the discussion of the entire work. It contains the most important aspects of the problem statement previously stated in section 1.5.

Choice of Prototype structure

The first step was to choose a suitable Prototype structure that will reflect the dimension of the future RWSF and will yield conservative results for the choice of actuators. To avoid torsion and thereby complication in the analysis, the structure was chosen as regular both in height and elevation. A product for the slab was proposed (figure 10.2) which ensures a rigid behaviour in xy plane and functions as a diaphragm. In this way an equal distribution of the lateral load on each frame is achieved.

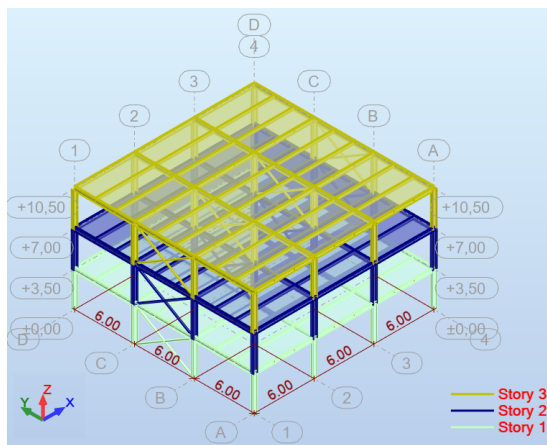


Figure 10.1: Prototype structure

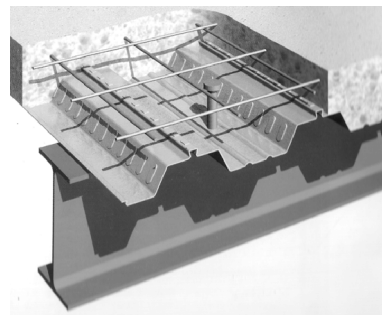


Figure 10.2: Slab solution: trapezoidal sheeting with concrete [Ganesh et al., 2005]

From so many lateral load restraining systems (LLRS) to choose from, decision was made to use the two most common for steel structures or namely the Moment Resisting Frame (MRF) and the Concentrically Braced Frame (CBF). Both of them are incorporated in the Prototype - each stabilizing it laterally in the corresponding direction - x for MRF and y for CBF. In this way more diverse results are obtained since MRF and CBF have different load-deflection characteristics. It is needless to say that the more types of LLRS and materials are examined, the closer one would reach to the necessary actuators capacity and stroke for the RWSF facility. However, as a Thesis delimitation, it is decided to limit the investigation to the aforementioned steel LLRS.

Prototype linear analysis

The linear analysis is performed on a spatial model in Autodesk Robot [2021] using the Modal Response Spectrum Analysis (MRSA) according to EN1998-1 [2004]. This method is chosen because of its reliability and wide range of use within the earthquake community. Furthermore it incorporates modal analysis which helps understand the structural behaviour and response. Since the prototype structure is regular both in height and elevation it was possible to perform the MRSA on two separate planar models. However, it was decided to add a third dimension (spatial model) and provide all necessary structural elements so that it would be possible to test the entire Prototype in the future RWSF facility.

A brief sensitivity study (figure 10.3) has been carried out to choose which response spectra from EN1998-1-BGNA [2012] provides the most conservative result (i.e largest forces) for the Prototype structure. It was concluded that soil type *C/E* and response spectra 1 yield the largest spectral acceleration (i.e. forces) given the dominant periods of the Prototype in each orthogonal direction. It should be noted that more conservative results could be obtained by using a response spectrum from other national annexes to EN1998-1 [2004] (such as Italian) or even artificially an generated one.

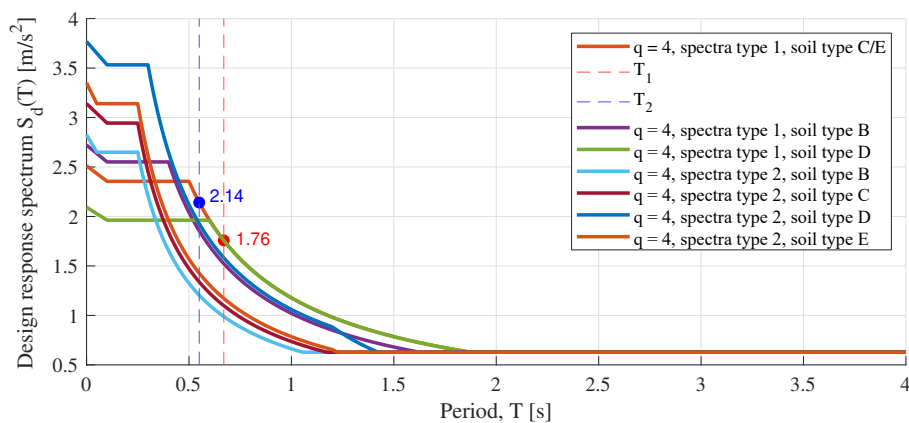


Figure 10.3: Sensitivity study on how soil and spectra types from EN1998-1-BGNA [2012] influence the response of the Prototype structure in its two dominant mode shapes - 1 and 2. $a_g = 0.32g$ and $q = 4$

The results produced from the linear numerical model were verified using a range of analytical methods and their conformity to the criteria set in EN1998-1 [2004] were proven with MATLAB generated graphs.

Prototype design

It is well known that structures designed to resist earthquake rely on energy dissipation through inelastic (ductile) behaviour. In EN1998-1 [2004] there are three ductility classes - low (DCL), medium (DCM) and high (DCH). Designing the Prototype in DCL would result in larger base shear but smaller displacement since it would dissipate energy only through elastic behaviour (i.e. larger elements are needed). For DCH this is vice versa since energy dissipation would happen through inelastic behaviour which is much more efficient. To have the best of both worlds when it comes to choosing actuator stroke and capacity, the prototype is designed in DCM by using a behaviour factor of $q = 4$ during the MRSA. According to EN1998-1 [2004] working with DCM requires following the capacity design rules. A long iterative procedure has been performed to choose cross sections for the MRF and CBF which conform to all capacity design criteria set in EN1998-1 [2004] which aim at obtaining appropriate ductile properties of the structure.

During the design, it was concluded that the MRF beam segment close to the column has out of plane stability problems which would interfere with the development of the targeted plastic mechanism in the MRF. Therefore, a proposal was suggested which would ensure the lateral stability of this beam segment as shown in figure 10.4 below.

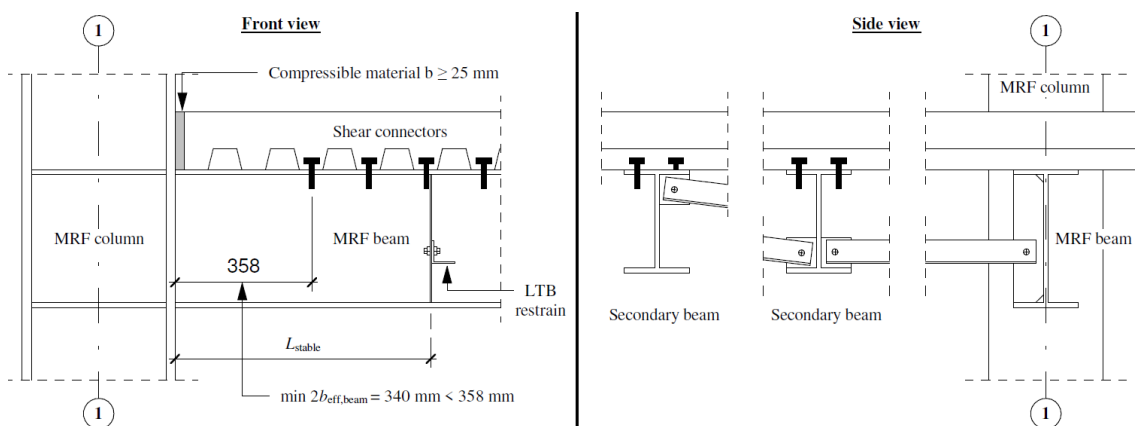


Figure 10.4: Example sketch of the solution proposed for stabilizing laterally the MRF beam segment close the column

Furthermore, a solution on preliminary design level (sketches) was proposed for each joint in the Prototype structure in subsection 2.6.

Prototype non-linear analysis

The non-linear analysis on the Prototype was performed using the non-linear static (Pushover) analysis in SeismoStruct [2022]. This method concluded to be the most suitable since it can be reproduced by a RWSF experiment. Its most important aspects are discussed below.

Constitutive model

The used constitutive model for the steel is bilinear with kinematic strain hardening. This model is simple and not computationally intensive, however its main limitation is that it assumes fracture when the ultimate strain is reached. In reality the material can develop more strain before reaching fractures which means that its behaviour after reaching the ultimate strain (stress) is not reflected. This results in uncertainty in the *CN* displacement obtained from the Pushover analysis. This can be avoided by the use of more detailed constitutive models, however that requires further experimental studies to determine the necessary material modelling parameters. Given the lack of information for the material parameters the chosen constitutive model is a viable option due to its simplicity and accuracy.

Non-linear computational model

The non-linear computational model accounts only for material and geometrical ($P - \Delta$ effects) non-linearity. It does not account for the development of local effects which might happen before the fracture in the material is reached. These effects include, among all failure in joints (welds, bolts, plates) local buckling and many more. This means that local failure in certain zones might happen before an element fractures causing local instability and different response from the one recorded numerically. All of this is well understood and accepted since numerical modelling has its limitations.

Modelling the CBF diagonals

The CBF planar model is modelled with active tensile (T) and inactive compressive (C) diagonals. In order to accurately represent the buckling behaviour and degradation of the C ones requires a lot more work and research which could be a project of its own. This is why the modelling of the C diagonals is not included in the Thesis delimitation. Their presence would have increased the stiffness of the CBF planar model and therefore contributed to the development of higher base shear.

Prototype non-linear response

Looking at figure 10.5 it is easy to see that the MRF provides both larger base shear and *CN* displacement which are both used to choose actuator parameters. However, the CBF provides larger reaction forces as seen in table 9.6 and as previously discussed in section 9.4 their value is vital for the design of the future RWSF facility. It should be noted that in many numerical simulations collapse is assumed when 20% of the capacity (base shear) is left. However, as seen in figure 10.5 it is decided to 'push' the MRF and CBF until numerical instability or structural collapse is reached. This is done to achieve larger *CN* displacement which would correspond to necessity for larger actuator stroke.

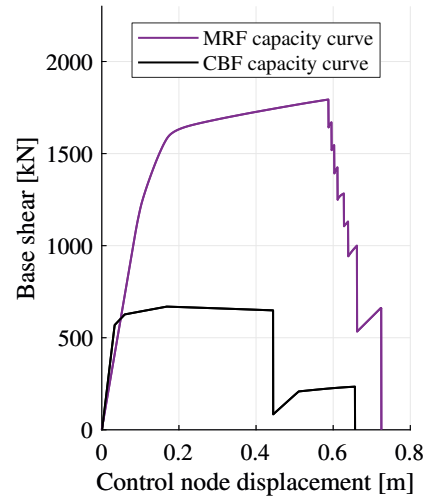


Figure 10.5: MRF and CBF pushover curves

Figures 10.6 to 10.9 illustrate the response of both linear the and non-linear models in terms of the maximum base shear and storey displacements (*CN* displacement). As expected, the non-linear models provide larger values for both the base shear and displacement since the inelastic properties of the structure are utilized. This goes to prove how much elastic design underestimates the load-bearing capacity of structures.

The difference between the base shear obtained for the linear and non-linear MRF models is a lot more significant to that compared to the CBF. This is explained with the fact the the CBF non-linear model has its compressive diagonals as inactive which reduces significantly its stiffness and thereby storey shear.

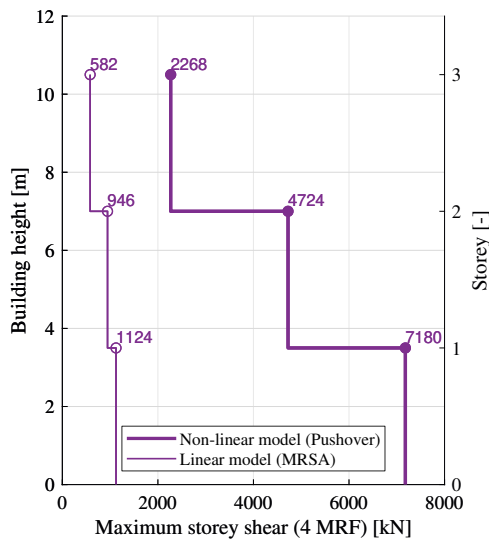


Figure 10.6: Storey shear forces for 4 MRF: linear and non-linear models

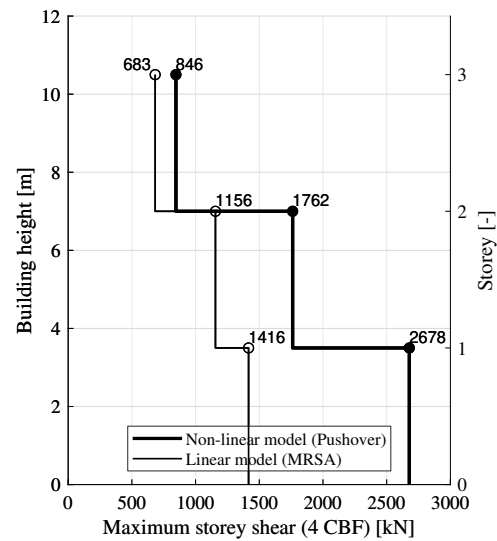


Figure 10.7: Storey shear forces for 4 CBF: linear and non-linear models

Looking at figures 10.8 and 10.9, it is visible that the displacement curve changes significantly when collapse in the non-linear model is reached. This is explained with the redistribution of forces caused by the inelastic behaviour. Both the MRF and CBF storey displacements produced by the non-linear model are notably higher from the linear one from which can be concluded that they exhibit a very ductile behaviour.

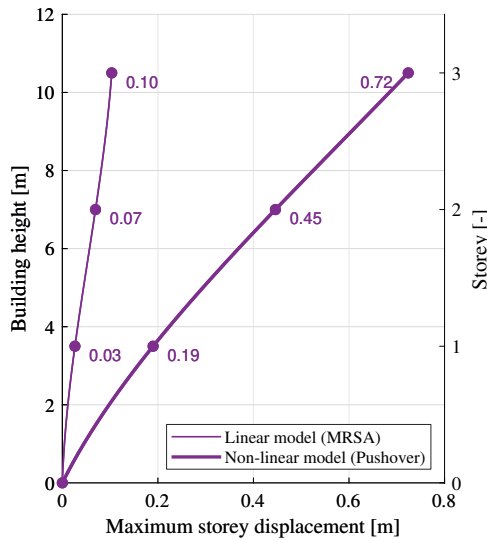


Figure 10.8: Maximum storey displacements: linear and non-linear MRF models

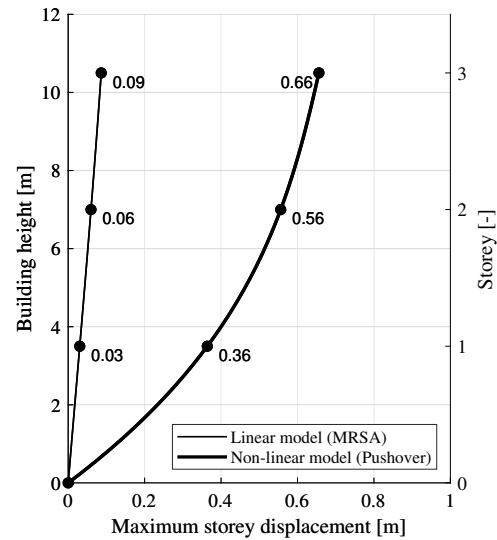


Figure 10.9: Maximum storey displacements: linear and non-linear CBF models

The pushover analysis is an exceptional tool for verifying the yielding and collapse mechanism of structures. In case of the Prototype a certain plastic mechanisms has been targeted by the capacity design performed earlier in chapter 6. For the MRF this is the weak beam - strong column concept which is achieved looking in figures 10.10 and 10.11 below. For CBF the desired plastic mechanism consist of the the gradual plastification of the tensile diagonals on each storey starting from *D1*, and as seen in figures 9.25 to 9.27 it is also achieved. The results from the Pushover analysis can be used to conclude that the capacity design on the Prototype structure has been correctly executed for both the MRF and CBF.

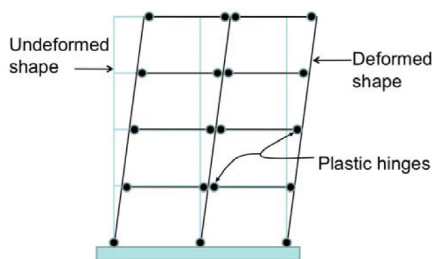


Figure 10.10: Strong column - weak beam concept [Hamburger and Malley, 2016]

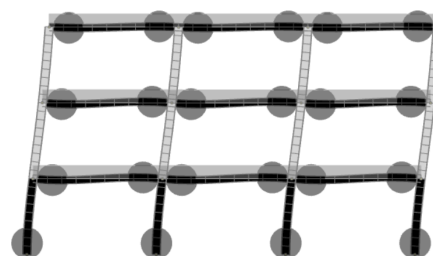


Figure 10.11: Full plastic mechanism developed in MRF (Y6)

Choice of actuator parameters

The two most important parameters for choosing actuators are the stroke - how far it can move and capacity - how much load it can apply. By looking at the maximum storey force and displacement (section 9.4) a net value for the necessary actuator capacity and stroke is obtained and summarized in table 10.1.

Table 10.1: Net values for necessary actuator capacity and stroke

Capacity	Stroke
614 kN	0.59 m-0.89 m

A very important aspect for the choice of actuators is ensuring that they do not saturate as suggested by Pierre Pegon (responsible for ELSA Reaction Wall) during one of the discussions the author had with him. Over-saturation is a phenomenon that happens when device capabilities of a controlled apparatus are reached. This causes it not to behave as commanded which leads to wrong results during an experiment. To avoid that phenomenon, the net values in table 10.1 must be provided with sufficient provision. An educated guess would be to increase both the net values for the capacity and stroke by 20 % to 30 %. However, this strongly depends on many factors the main of which is the type of chosen actuator. The capacity of the actuator also reflects the maximum force applied on to the RWSF. Therefore, choosing more capable actuators require thicker reaction wall since it must remain elastic. Furthermore, the reaction wall and strong floor are normally designed as one entity which means that not only forces from the actuators must be considered but also the reaction forces from the Prototype structure documented in tables 9.5 and 9.6.

Next steps

Since the designed MRF and CBF exhibit a very ductile behaviour (large displacement and not so large base shear), the author recommends investigating the response of at least one more LLRS designed with low dissipative behaviour (i.e. DCL). In this way the ductility of the structure will be reduced which would mean that higher base shear will be obtained and therefore larger actuator capacity would be concluded. This can be a steel MRF with $q < 2$ (i.e DCL) or even a RC shear wall.

The report contains a proposal on a preliminary design stage for a full scaled 3D prototype. The author suggest to use the suggested Prototype and recreate the pushover simulation during a RWSF experiment. The results from the non linear analysis can then be experimentally verified and even used for calibrating the apparatus and devices in the future RWSF facility.

Bibliography

- Autodesk Robot, 2021.** Autodesk Robot. *Robot Structural Analysis Professional*, 2021.
- Bisch et al., 2011.** P. Bisch, E.Carvalho, H.Degee, P.Fajfar, M. Fardis, P. Franchin, M. Kreslin, A. Pecker, P. Pinto, A. Plumier, H. Somja and G. Tsionis. *Eurocode 8: Seismic Design of Buildings Worked examples*. ISBN: 978-92-79-23068-4, Paperback. European Commission Joint Research Center, 2011.
- Chopra and la Llera, 1996.** Anil K. Chopra and Juan C. De la Llera. *Accidental and natural torsion in earthquake response and design of buildings*. Eleventh World Conference on Earthquake Engineering, Paper No. 2006, 15, 1996.
- Damkilde, 2019.** Lars Damkilde. *Introduction to Structural Dynamics*, 2019.
- ECCS, 2018.** ECCS. *Equaljoints PLUS Volume with information brochures for 4 seismically qualified joints*, 2018.
- EN1990, 2007.** EN1990. *Eurocode - Basis of structural design*, 2007.
- EN1991-1-1, 2002.** EN1991-1-1. *Eurocode 1 - Actions on structures - Part 1-1: General actions - Densities, self-weight, imposed loads for buildings*, 2002.
- EN1991-1-3, 2003.** EN1991-1-3. *Eurocode 1 - Actions on structures - Part 1-3: General actions - Snow loads*, 2003.
- EN1993-1-1, 2007.** EN1993-1-1. *Eurocode 3: Design of steel structures. Part 1-1: General rules and rules for buildings*, 2007.
- EN1993-1-5, 2006.** EN1993-1-5. *Eurocode 3 - Design of steel structures - Part 1-5: Plated structural elements*, 2006.
- EN1998-1, 2004.** EN1998-1. *Eurocode 8: Design of structures for earthquake resistance. Part 1: General rules, seismic actions and rules for buildings*, 2004.
- EN1998-1-BGNA, 2012.** EN1998-1-BGNA. *Bulgarian National Annex to Eurocode 8: Design of structures for earthquake resistance. Part 1: General rules, seismic actions and rules for buildings*, 2012.
- GA et al., 2014.** Sabau GA, Poljansek M, Taucer F, Pegon P, Molina Ruiz FJ, Tirelli D, Viacoz B, Stratan A, Dubina D and Ioan Chesoa A. *SEISMIC ENGINEERING RESEARCH INFRASTRUCTURES FOR EUROPEAN SYNERGIES. Full-scale experimental validation of a dual eccentrically braced frame with removable links (DUAREM)*, 2014.
- Ganesh et al., 10 2005.** Mohan Ganesh, Akhil Upadhyay and S. Kaushik. *Simplified Design of Composite Slabs Using Slip Block Test*. *Journal of Advanced Concrete Technology - J ADV CONCR TECHNOL*, 3, 403–412, 2005. doi: 10.3151/jact.3.403.

- Georgiev, 2021.** Tzvetan Georgiev. *Lecture 6.1 - Design of Moment Resisting Frames according to EN 1998-1*, 2021.
- Hamburger and Malley, 2016.** Ronald O. Hamburger and James O. Malley. *Seismic Design of Steel Special Moment Frames. A Guide for Practicing Engineers*. NIST GCR 16-917-41, Digital. National Institute of Standards and Technology. U.S. Department of Commerce, 2016.
- Jiménez et al., 2003.** M.-J Jiménez, D. Giardini and G. Grünthal. *The ESC-SESAME unified hazard model for the European-Mediterranean region*. *EMSC/CSEM Newsletter* 19, 2-4., 2003.
- Khoso and Naqash, 03 2014.** Salim Khoso and Muhammad Naqash. *An Overview on the Seismic Design of Braced Frames*. *American Journal of Civil Engineering* 04/2014; 2(2):41-47. DOI:10.11648/j.ajce.20140202.15, 2, 41–4715, 2014. doi: 10.11648/j.ajce.20140202.15.
- Landolfo, 2022.** Raffaele Landolfo. *European seismic prequalification of steel beam-to-column joints: EQUALJOINTS and EQUALJOINTS-Plus projects*. *Journal of Constructional Steel Research*, 192, 107238, 2022. ISSN 0143-974X. doi: <https://doi.org/10.1016/j.jcsr.2022.107238>. URL <https://www.sciencedirect.com/science/article/pii/S0143974X22001109>.
- Marabi, 2016.** Bahram Marabi. *A NUMERICAL AND ANALYTICAL STUDY ON OPTIMIZATION AND EFFICIENCY OF STRUCTURAL FORMS BY TWO-OUTRIGGER IN TALL BUILDINGS*, 2016.
- Marazzi et al., 04 2011.** Francesco Marazzi, Ioannis Politopoulos and Alberto Pavese. *An overview of seismic testing needs in Europe: Towards a new advanced experimental facility*. *Bulletin of Earthquake Engineering*, 9, 623–640, 2011. doi: 10.1007/s10518-010-9212-8.
- MECHS, 2018.** MECHS. *MECHS SERIES WEBINAR: HYBRID SIMULATION 101*, 2018.
- METECNO, 1961.** METECNO. <https://www.metecno.com/index.php/en/1>, 1961.
- Minkov, 2022.** Boris Minkov. *Practical Placement Report - Seismic Analysis and Design of steel-concrete structure*. Link: <https://www.researchgate.net/publication/357901843>, 2022.
- Nielsen, 2009.** Jannie Nielsen. *Probabilistic analysis of the robustness of earthquake resistant steel structures*, 2009.
- Peres et al., 2016.** Rita Peres, José Castro and Rita Bento. *An extension of an improved forced based design procedure for 3D steel structures*. *N/A*, 22(4), 1115–1140, 2016. ISSN N/A. doi: 10.12989/scs.2016.22.5.1115.
- Rai et al., 2014.** Durgesh C Rai, Sudhir K Jain, Murty CVR and Dipanshu Bansal. *CONSTRUCTION AND LOAD RATING OF LARGE CAPACITY REACTION FLOOR-WALL ASSEMBLY FOR LATERAL LOAD TESTING AT IIT KANPUR*, 2014.
- SeismoStruct, 2022.** SeismoStruct. *Award-winning Finite Elements package capable of predicting the large displacement behaviour of space frames under static or dynamic loading, taking into account both geometric nonlinearities* Read more at: <https://seismosoft.com/product/seismostruct/>, 2022.

SERIES, 2013. SERIES. *Seismic Engineering Research Infrastructure for European Synergies*, 2013.

Spacone et al., 2010. Enrico Spacone, Mourad Belgasmia and Aleksander Urbanski. *Seismic Evaluation of Constructions: Nonlinear Frame Analysis Procedures in ZSOIL*, 2010.

Vigh et al., 08 2017. László Vigh, Ádám Zsarnóczy and Tamás Balogh. *Eurocode conforming design of BRBF – Part I: Proposal for codification*. *Journal of Constructional Steel Research*, 135, 265–276, 2017. doi: 10.1016/j.jcsr.2017.04.010.

Yun and Gardner, 06 2017. Xiang Yun and Leroy Gardner. *Stress-strain curves for hot-rolled steels*. *Journal of Constructional Steel Research*, 133, 36–46, 2017. doi: 10.1016/j.jcsr.2017.01.024.



Appendix

A	Prototype	115
A.1	Steel properties	
A.2	Characteristic loads and actions	
B	Linear computational model	123
B.1	Member and node numbers	
B.2	Member definition - design parameters	
B.3	Load cases and combinations	
B.4	Quality assurance (QA)	
C	Non-linear computational model	135
C.1	Member and node numbers	
C.2	Vertical (gravity) loads	
C.3	Lateral (incremental) loads	
C.4	Quality assurance (QA)	
D	Modal Response Spectrum Analysis	141
D.1	Theory	
D.2	Basic period check using the Rayleigh quotient	
D.3	Sensitivity study: choice of response spectrum	
D.4	Base shear quality assurance	
D.5	Prototype sensitivity to second order effects	
D.6	Prototype damage limitation	
E	Pushover analysis	151
E.1	Theory	
F	Prototype Capacity Design	155
F.1	CBF	
F.2	MRF	
G	Thesis contract	161

A Prototype

This appendix contains a summary of the material properties used for the Prototype and the characteristic loads and actions applied on it.

A.1 Steel properties

A.1.1 Linear constitutive model

Table A.1: Linear constitutive model: steel material properties

Material	Yield strength f_{yk} [MPa]	Young's modulus E [MPa]	Poisson's ratio ν [-]	Shear modulus G [MPa]	Standard [-]
S235 JR	235	210000	0.3	81000.00	EN 10025-2
S275 JR	275	210000	0.3	81000.00	EN 10025-2
S460 N/NL	460	210000	0.3	81000.00	EN 10025-3

A.1.2 Non-linear constitutive model

Table A.2: Non-linear constitutive model: steel material properties

Material	Yield strength f_y [MPa]	Young's modulus E [MPa]	E_p [MPa]	Poisson's ratio ν [-]	Shear modulus G [MPa]
S235 JR	305.50	210000	2100	0.3	81000.00
S275 JR	343.75	210000	2100	0.3	81000.00
S460 N/NL	440.00	210000	2100	0.3	81000.00

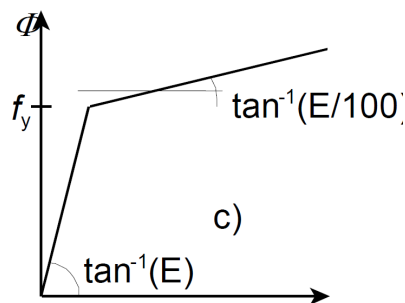


Figure A.1: Bi-linear stress-strain curve with strain hardening [EN1993-1-5, 2006]

A.2 Characteristic loads and actions

A.2.1 Trapezoidal sheet HI-BOND A55/P600

The used properties and load capacity is for a sheet thickness of 1.2 mm and is marked with red.

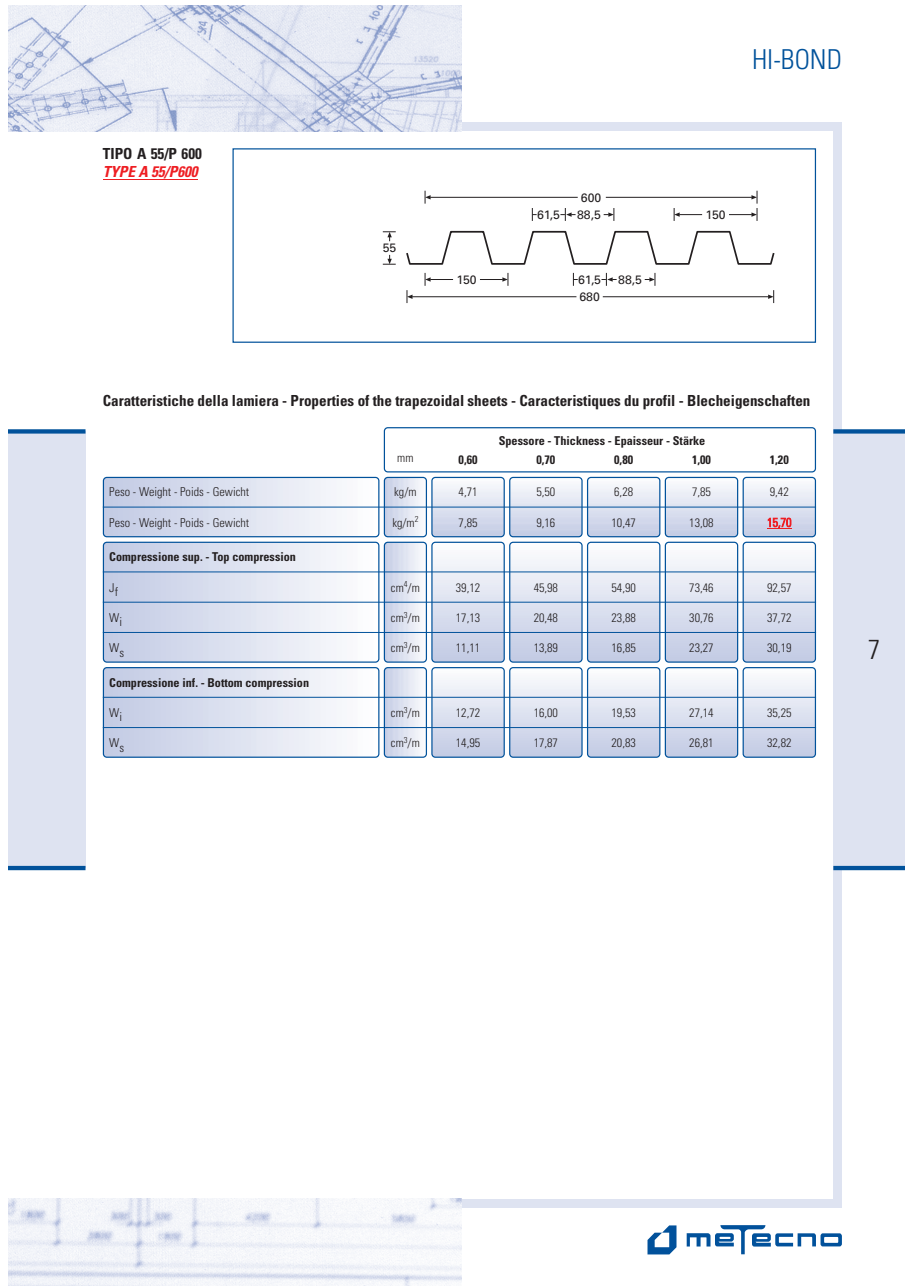
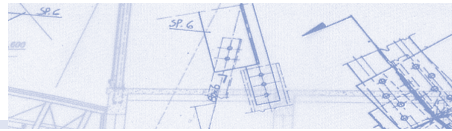


Figure A.2: HI-BOND A55/P600 properties

HI-BOND



TIPO A 55/P 600
TYPE A 55/P 600

Carico massimo uniformemente distribuito in da.N/m², freccia ≤ l/200
 Maximum load in da.N/m², deflection ≤ l/200
 Charge uniformement repartie en da.N/m², flèche ≤ l/200
 Gleichmäßig verteilte belastung in da.N/m², durchbiegung ≤ l/200

Spess. Thick. Epais. Dicke mm	J cm ⁴ /m	Wp cm ³ /m	Wn cm ³ /m	Distanza fra gli appoggi in metri - Span in meters - Entr'axe des solives - Spannweite in Metern																		
				1,00	1,25	1,50	1,75	2,00	2,25	2,50	2,75	3,00	3,25	3,50	3,75	4,00	4,25	4,50	4,75	5,00	5,25	5,50
0,60	39,12	11,11	12,72	1467	939	652	479	367	277	202	152	117	92	74	60	49	41	35				
0,70	45,98	13,89	16,00	1833	1173	815	599	458	326	238	179	138	108	87	70	58	48	41	35			
0,80	54,90	16,85	19,53	2224	1423	989	726	554	389	284	213	164	129	103	84	69	58	49	41	35		
1,00	73,46	23,27	26,81	3072	1966	1365	1003	742	521	380	285	220	173	138	113	93	77	65	55	47	41	36
1,20	92,57	30,19	32,82	3985	2550	1771	1301	968	656	479	360	277	218	174	142	117	97	82	70	60	52	45

Spess. Thick. Epais. Dicke mm	J cm ⁴ /m	Wp cm ³ /m	Wn cm ³ /m	Distanza fra gli appoggi in metri - Span in meters - Entr'axe des solives - Spannweite in Metern																		
				1,00	1,25	1,50	1,75	2,00	2,25	2,50	2,75	3,00	3,25	3,50	3,75	4,00	4,25	4,50	4,75	5,00	5,25	5,50
0,60	39,12	11,11	12,72	1679	1075	746	548	420	332	269	222	187	159	137	119	105	93	83	73	62		
0,70	45,98	13,89	16,00	2112	1352	939	690	528	417	338	219	235	200	172	150	132	117	101	85	73	63	
0,80	54,90	16,85	19,53	2578	1650	1146	842	644	509	412	341	286	244	210	183	161	142	120	102	88	76	66
1,00	73,46	23,27	26,81	3539	2265	1156	1156	885	699	566	468	393	335	289	252	221	191	137	137	117	101	88
1,20	92,57	30,19	32,82	4332	2773	1925	1415	1083	856	693	573	481	410	354	308	271	240	202	172	148	127	111

Spess. Thick. Epais. Dicke mm	J cm ⁴ /m	Wp cm ³ /m	Wn cm ³ /m	Distanza fra gli appoggi in metri - Span in meters - Entr'axe des solives - Spannweite in Metern																		
				1,00	1,25	1,50	1,75	2,00	2,25	2,50	2,75	3,00	3,25	3,50	3,75	4,00	4,25	4,50	4,75	5,00	5,25	5,50
0,60	39,12	11,11	12,72	2099	1343	933	685	525	415	336	278	221	174	139	113	93	78	66	56	48		
0,70	45,98	13,89	16,00	2640	1690	1173	862	660	521	422	337	260	204	164	133	110	91	77	65	56	48	
0,80	54,90	16,85	19,53	3222	2062	1432	1052	806	637	516	403	310	244	195	159	131	109	92	78	67	58	50
1,00	73,46	23,27	26,81	4424	2831	1966	1444	1106	874	708	539	415	327	261	213	175	146	123	105	90	77	67
1,20	92,57	30,19	32,82	5415	3466	2407	1768	1354	1070	886	679	523	412	330	268	221	184	155	132	113	98	85

I valori in colore non prevedono limitazione di freccia - Values indicated in color are calculated without deflection limitation - Les valeurs imprimées en couleur sont sans limitation de flèche - Die in Farbe angegebenen Werte sehen keine Begrenzung der Durchbiegung vor.



Figure A.3: HI-BOND A55/P600 load capacity

A.2.2 Permanent loads - kG

EN1991-1-1 [2002]

Table A.3: Structural material densities kG1/struct/

Type [-]	Value [kN/m ³]	γ_f [-]	K_{FI} [-]
Steel	77.01	1.35	1.00
Concrete	25.00	1.35	1.00

Table A.4: Slab/diaphragm kG1/struct/

Type [-]	Value [kN/m ²]	γ_f [-]	K_{FI} [-]
Corrugated steel sheeting A55-P600 G5 (t=1,2mm)	0.15	1.35	1.00
55 mm RC cast between sheeting	0.69	1.35	1.00
95 mm RC cast above sheeting	2.37	1.35	1.00
Total	3.22		

Table A.5: Roof structure (storey 3) kG2/roof/

Type [-]	Value [kN/m ²]	γ_f [-]	K_{FI} [-]
Suspended ceiling	0.20	1.35	1.00
Bitumen	0.10	1.35	1.00
XPS insulation	0.06	1.35	1.00
Electrical and water installations	0.15	1.35	1.00
RC for slope	1.90	1.35	1.00
Total	2.41		

Table A.6: Floor structure (stories 1 and 2) kG3/floor/

Type [-]	Value [kN/m ²]	γ_f [-]	K_{FI} [-]
Light walls and partitions	1.20	1.35	1.00
Granite tiles flooring	1.15	1.35	1.00
Suspended ceiling	0.20	1.35	1.00
Electrical and water installations	0.15	1.35	1.00
Total	2.70		

Table A.7: Non-load-bearing external wall kG4/wall/

Type [-]	Value [kN/m ²]	γ_f [-]	K_{FI} [-]
Facade elements	0.40	1.35	1.00
Insulation	0.10	1.35	1.00
Glass	0.50	1.35	1.00
Total	1.00		

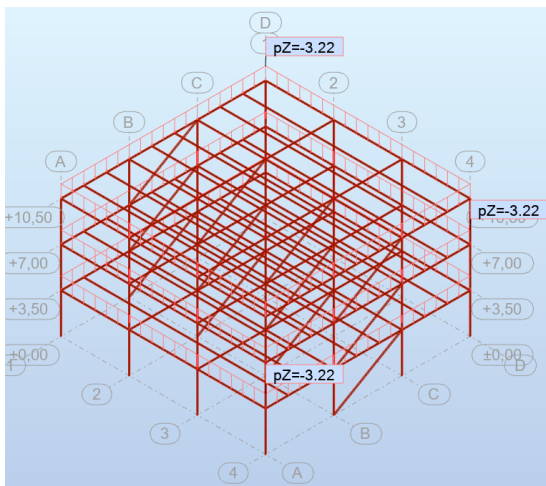


Figure A.4: kG1 applied in Robot

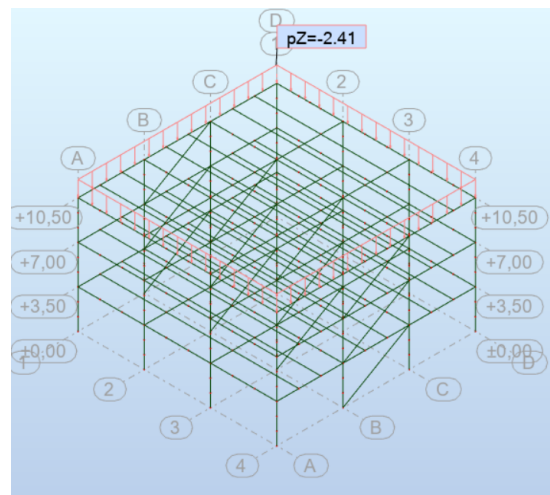


Figure A.5: kG2 applied in Robot

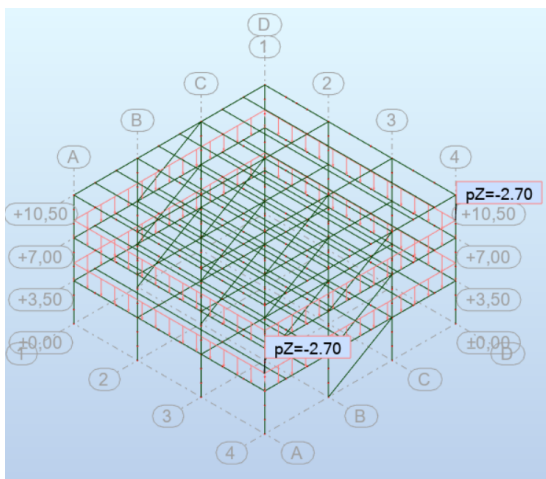


Figure A.6: kG3 applied in Robot

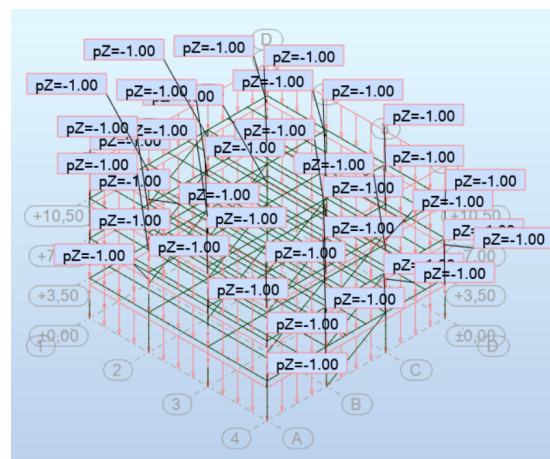


Figure A.7: kG4 applied in Robot

A.2.3 Imposed loads - kQ

EN1991-1-1 [2002]

Table A.8: Imposed load on the roof (storey 3) **kQ1/roof/**

Type [-]	Value [kN/m ²]	γ_f [-]	K_{FI} [-]
Category H	0.40	1.50	1.00

Table A.9: Roofs **kQ2/live/**

Type [-]	Value [kN/m ²]	γ_f [-]	K_{FI} [-]
Category B	3.00	1.50	1.00

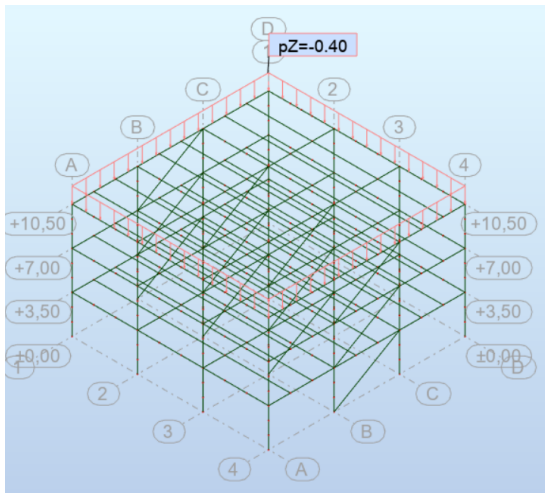


Figure A.8: kQ1 applied in Robot

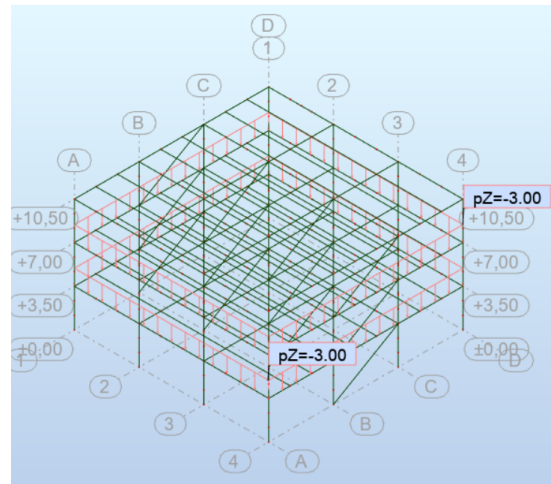


Figure A.9: kQ2 applied in Robot

A.2.4 Variable actions - kS1

EN1991-1-3 [2003]

The characteristic value for the snow load on the roof is calculated using (A.1) below. The parameters shown in table A.10 are chosen based on the most common snow scenario in Bulgaria after a discussion with the company supervisor.

Table A.10: Terms used for calculating the snow load on the roof

Snow on the ground S_k [kN/m ²]	Exposure coeff. C_e [-]	Thermal coeff. C_t [-]	Snow load shape coeff. μ_i [-]	γ_f [-]	K_{FI} [-]
1.28	1.0	1.0	0.8	1.5	1.0

$$s_c = \mu_i C_e C_t S_k = 1.02 \text{ kN/m}^2 \quad (\text{A.1})$$

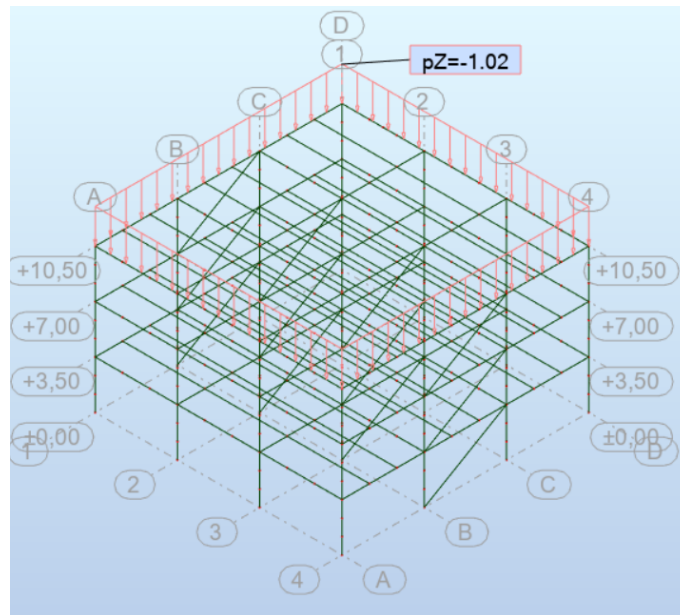


Figure A.10: kS1 applied in Robot

B Linear computational model

The linear computational model used for performing the MRSA is executed in Autodesk Robot [2021] with educational license from AAU. The .RTD file can be provided by request. This appendix contain all the vital information for verification and description of the model.

B.1 Member and node numbers

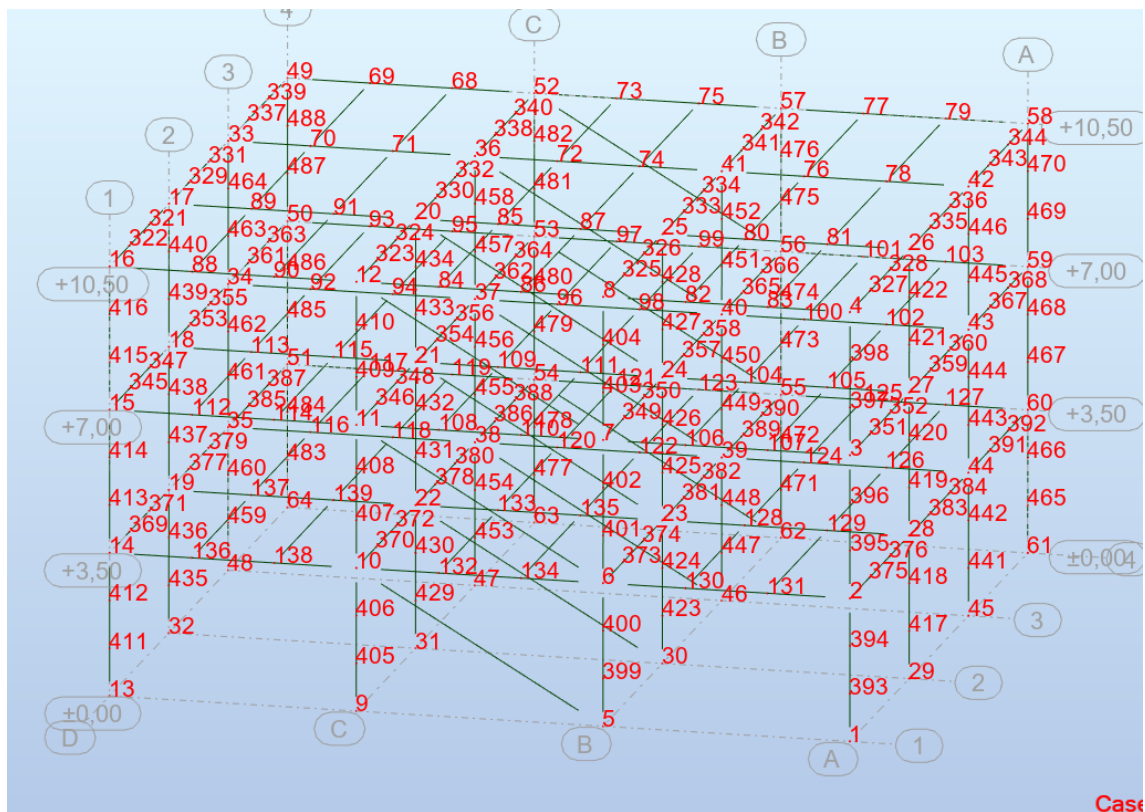


Figure B.1: Node numbers

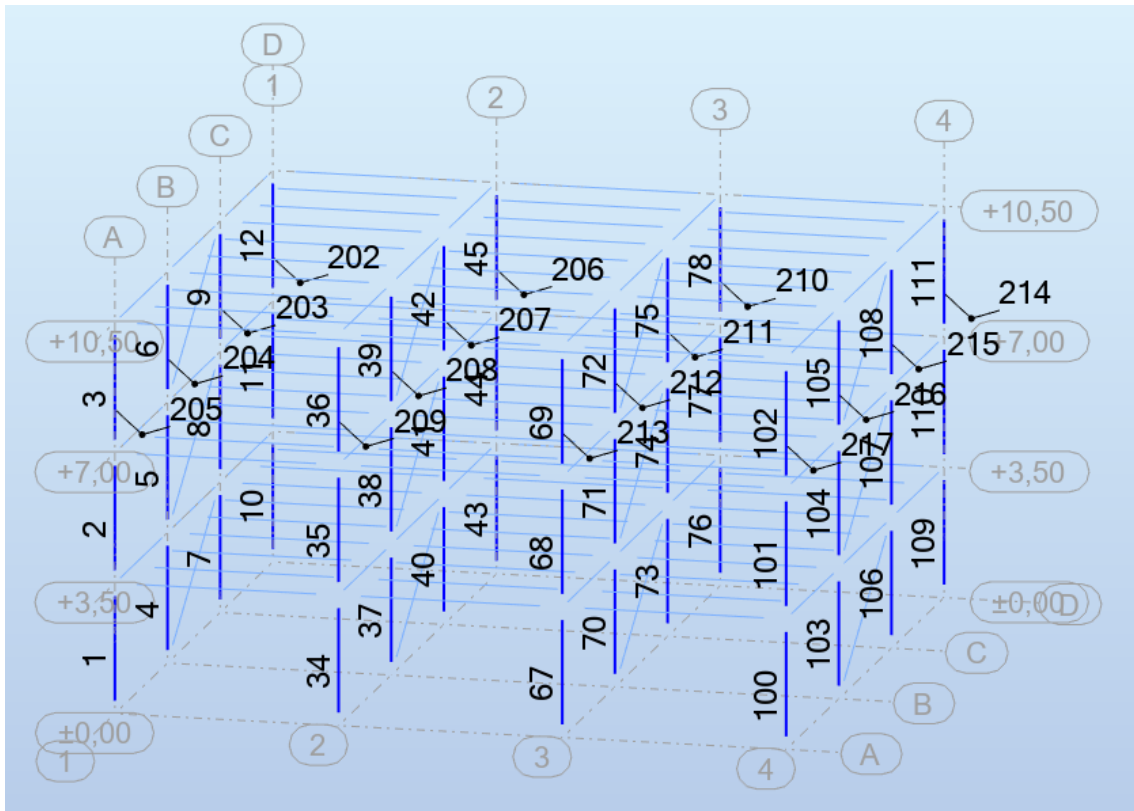


Figure B.2: Member numbers: columns

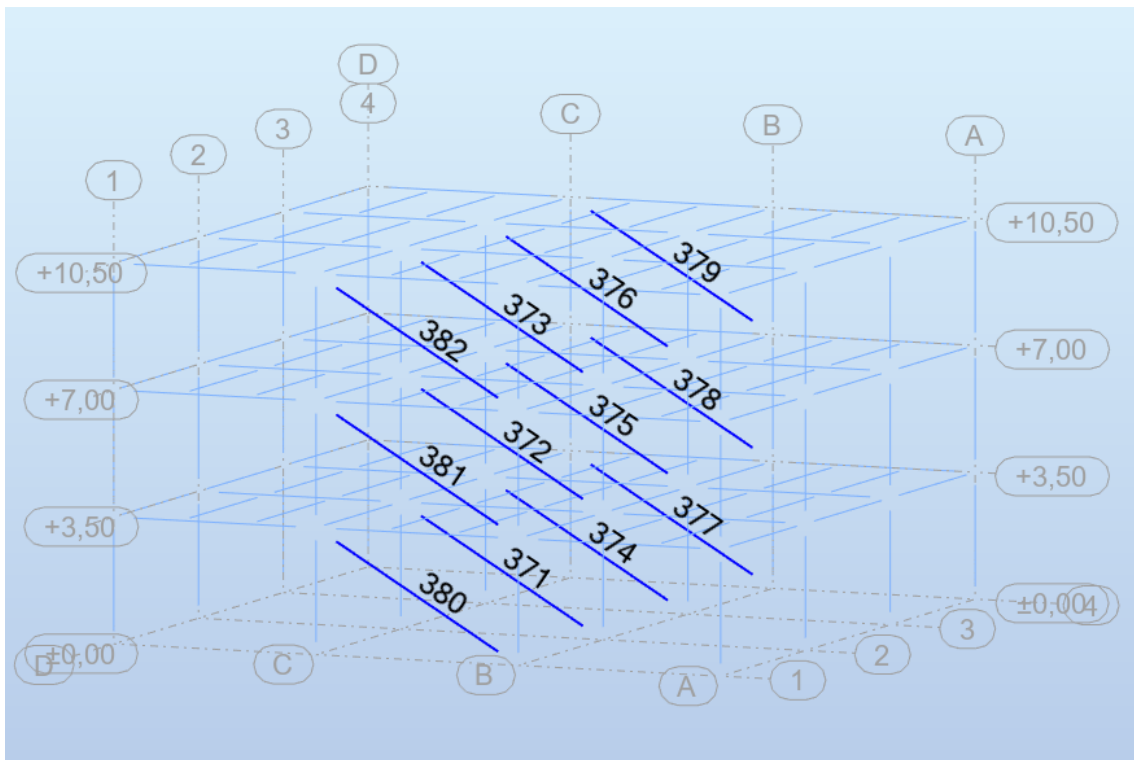


Figure B.3: Member numbers: diagonals

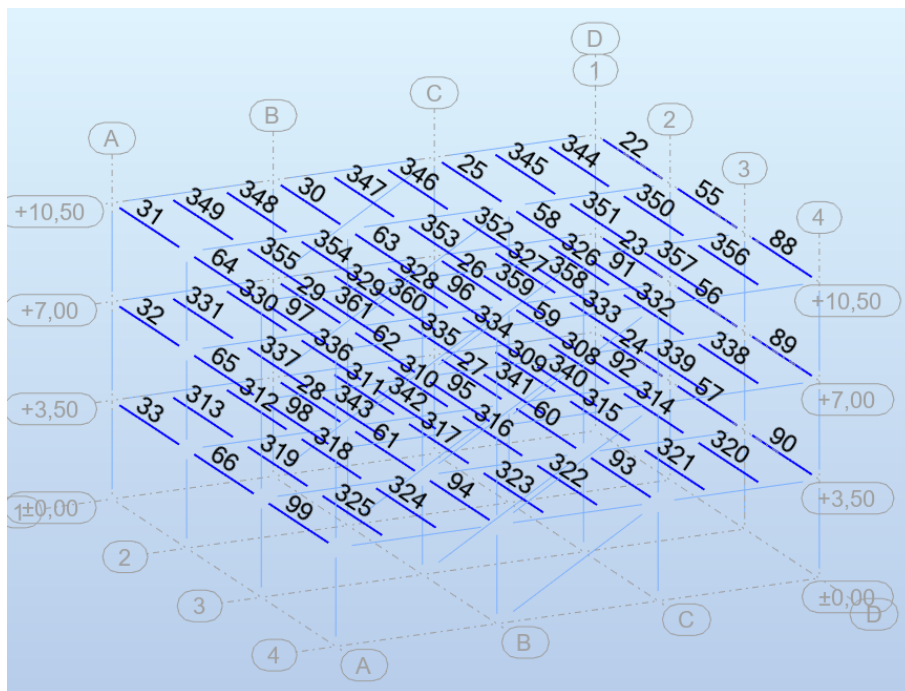


Figure B.4: Member numbers: beams in *x*-direction

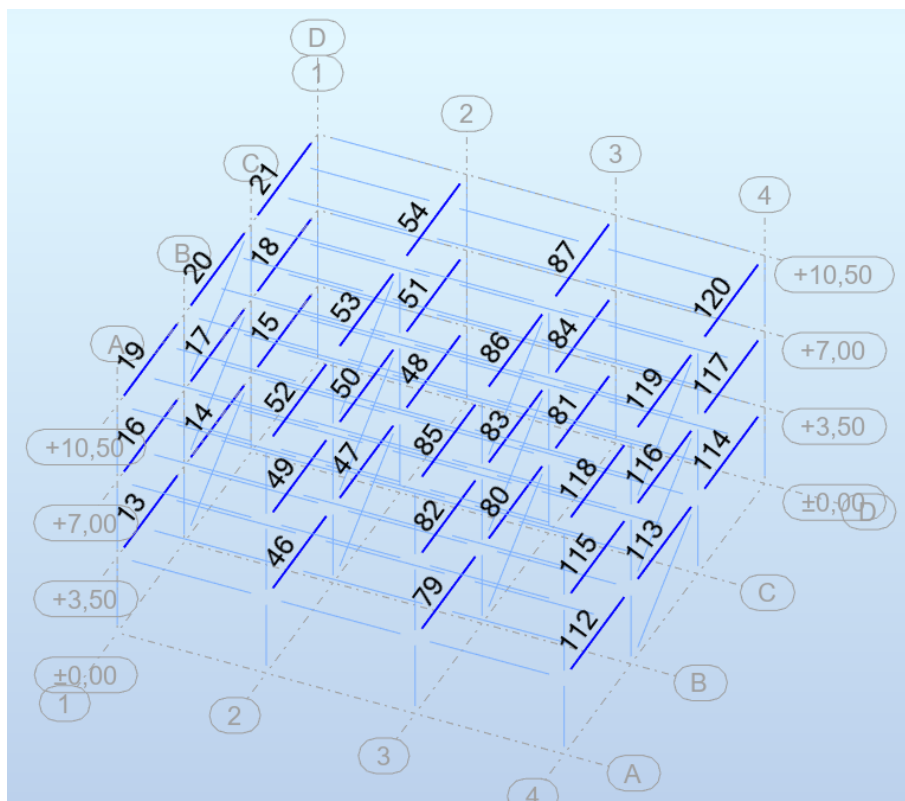


Figure B.5: Member numbers: beams in *y*-direction

B.2 Member definition - design parameters

Five different member types are defined and grouped in Autodesk Robot [2021] as shown in figure B.6 below. Their parameters (buckling length, LTB, load parameters) are defined according to the boundary conditions discussed in section 2.6. The way they these parameters are defined in Autodesk Robot [2021] are shown in figures B.7 to B.11 on the following page.

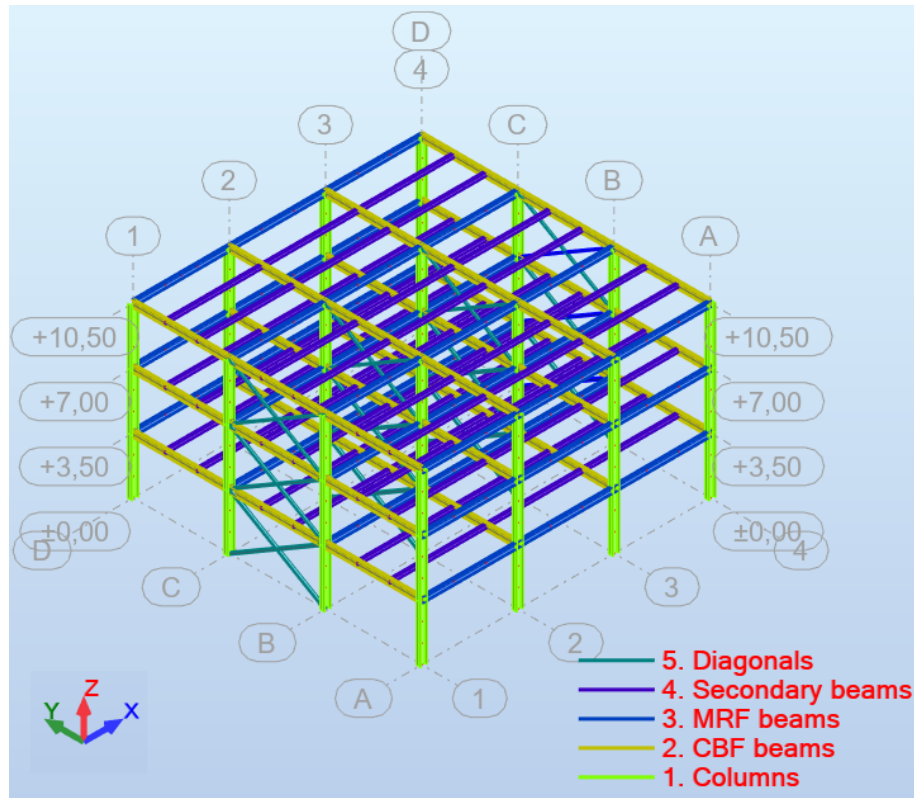


Figure B.6: Members by type

Member type: 5. Diagonals	
Buckling (y axis)	
Member length ly:	Member length lz:
<input type="radio"/> Real	<input type="radio"/> Real
<input checked="" type="radio"/> Coefficient 1,00	<input checked="" type="radio"/> Coefficient 1,00
Buckling length coeff. y:	Buckling length coeff. z:
1,00 <input checked="" type="checkbox"/> Sway	1,00 <input checked="" type="checkbox"/> Sway
Buckling curve y: c	Buckling curve z: c

Figure B.7: 5. Diagonals: Member definition - parameters according to EN1993-1-1 [2007]

Member type: 1. Columns

Buckling (y axis) Member length ly: Real Coefficient 3,50 m

Buckling (z axis) Member length lz: Real Coefficient 3,50 m

Buckling length coeff. y: 1,00 Non-sway

Buckling length coeff. z: 1,00 Non-sway

Buckling curve y: auto

Buckling curve z: auto

Flexural-torsional buckling

Lateral buckling parameters

Lateral buckling

Load level: Upper flange Lower flange

Lcr = lo Lcr = lo

Critical moment: Auto User

Load parameters Load type: My: Mz:

Lateral buckling curve: auto

Figure B.8: 1. Columns: Member definition - parameters according to EN1993-1-1 [2007]

Member type: 2. CBF beams

Buckling (y axis) Member length ly: Real Coefficient 1,00 m

Buckling (z axis) Member length lz: Real Coefficient 2,00 m

Buckling length coeff. y: 1,00 Non-sway

Buckling length coeff. z: 1,00 Non-sway

Buckling curve y: auto

Buckling curve z: auto

Flexural-torsional buckling

Lateral buckling parameters

Lateral buckling

Load level: Upper flange Lower flange

Lcr = lo Lcr = lo

Critical moment: Auto User

Load parameters Load type: My: Mz:

Lateral buckling curve: auto

Figure B.9: 2. CBF beams: Member definition - parameters according to EN1993-1-1 [2007]

Member type: 3. MRF beams

Buckling (y axis) Member length ly: Real Coefficient 1,00 m

Buckling (z axis) Member length lz: Real Coefficient 1,00 m

Buckling length coeff. y: 1,00 Non-sway

Buckling length coeff. z: 1,00 Non-sway

Buckling curve y: auto

Buckling curve z: auto

Flexural-torsional buckling

Lateral buckling parameters

Lateral buckling

Load level: Upper flange Lower flange

None Lcr = lo

Critical moment: Auto User

Load parameters Load type: My: Mz:

Lateral buckling curve: auto

Figure B.10: 3. MRF beams: Member definition - parameters according to EN1993-1-1 [2007]

Member type: 4. Secondary beams

Buckling (y axis) Member length ly: Real Coefficient 1,00 m

Buckling (z axis) Member length lz: Real Coefficient 1,00 m

Buckling length coeff. y: 1,00 Non-sway

Buckling length coeff. z: 1,00 Non-sway

Buckling curve y: auto

Buckling curve z: auto

Flexural-torsional buckling

Lateral buckling parameters

Lateral buckling

Load level: Upper flange Lower flange

None Lcr = lo

Critical moment: Auto User

Load parameters Load type: My: Mz:

Lateral buckling curve: auto

Figure B.11: 4. Secondary beams: Member definition - parameters according to EN1993-1-1 [2007]

B.3 Load cases and combinations

- The load cases are defined in accordance to Appendix A.2 and are shown in figure B.12 below.
- The ULS combinations are shown in figure B.13
- The SLS combinations are shown in figure B.14
- The seismic load cases and combination are not shown here - please refer to chapter 7.

List of defined cases:		
No.	Case name	Nature
→ 1	kG1/struct/	Structural
2	kG2/roof/	Structural
3	kG3/floor/	Structural
4	kG4/wall/	Structural
21	kS1/snow/	snow
22	kQ1/live/	Category H
23	kQ2/live/	Category B

Figure B.12: Applied load cases in Robot

Nr.	Name	Selfweight	Snow	Imposed load	
			Normal	Roof	Floor
		1+2+3+4	21	22	23
		kG/dead/	kS1/snow/	kQ1/live/	kQ2/live/
201	ULS01	1,35			
202	ULS02	1,35	1,05	1,50	1,05
203	ULS03	1,35	1,05	0,90	1,50
204	ULS04	1,35	1,50		
205	ULS05	1,35	1,50	0,81	1,05

Figure B.13: Applied ULS combinations according to EN1990 [2007] (STR/GEO) (Group B)

Nr.	Name	Selfweight	Snow	Imposed load	
			Normal	Roof	Floor
		1+2+3+4	21	22	23
		kG/dead/	kS1/snow/	kQ1/live/	kQ2/live/
301	SLS01	1,00			
302	SLS02	1,00	0,70	1,00	0,70
303	SLS03	1,00	0,70	0,60	1,00
304	SLS04	1,00	1,00		
305	SLS05	1,00	1,00	0,60	0,70

Figure B.14: Applied SLS combinations according to EN1990 [2007] eq 6.14b

B.4 Quality assurance (QA)

The QA of the computational model is performed by carefully investigating the distribution of the internal forces and displacements. They are shown in figures B.15 to B.23 and their titles are based on the notation shown in figure B.15. The member types can be seen in figure B.6 and load cases - in figure B.12.

Please note that the internal force diagrams are based on a local coordinate system and they are not in the correct scale.

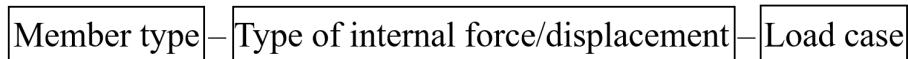


Figure B.15: Notation for the QA figures

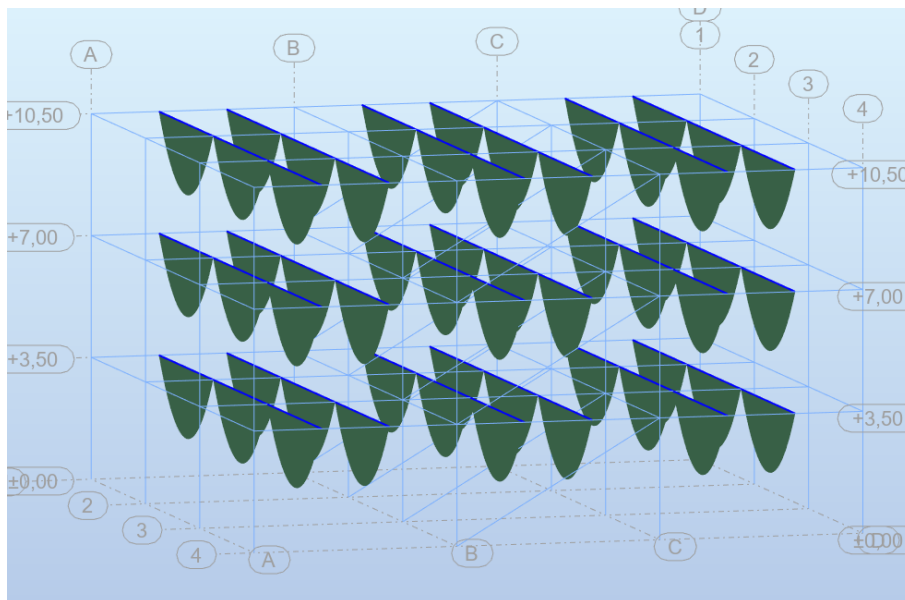


Figure B.16: 4. Secondary beams - MY - 1:kG1/struct/

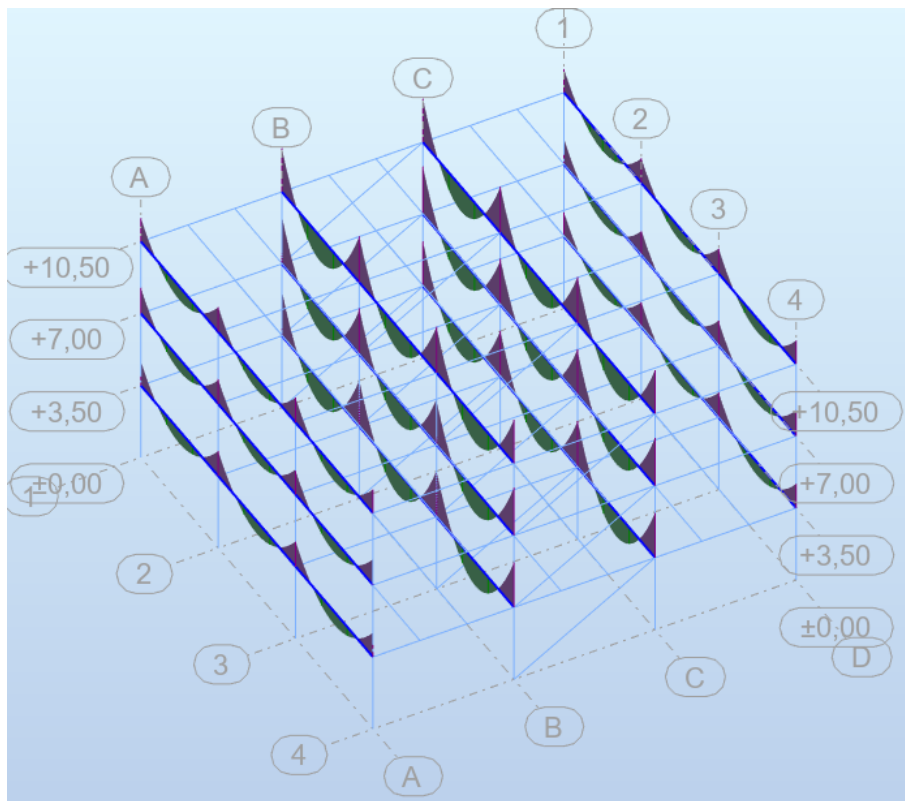


Figure B.17: 3.MRF beams - MY - 1:kG1/struct/

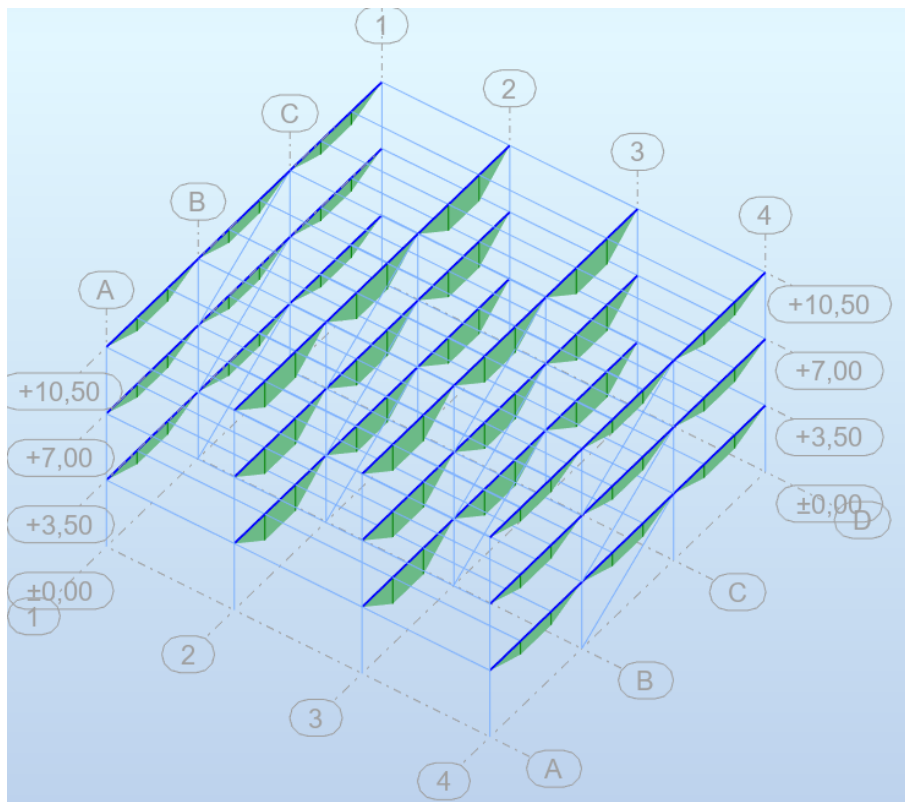


Figure B.18: 2.CBF beams - MY - 1:kG1/struct/

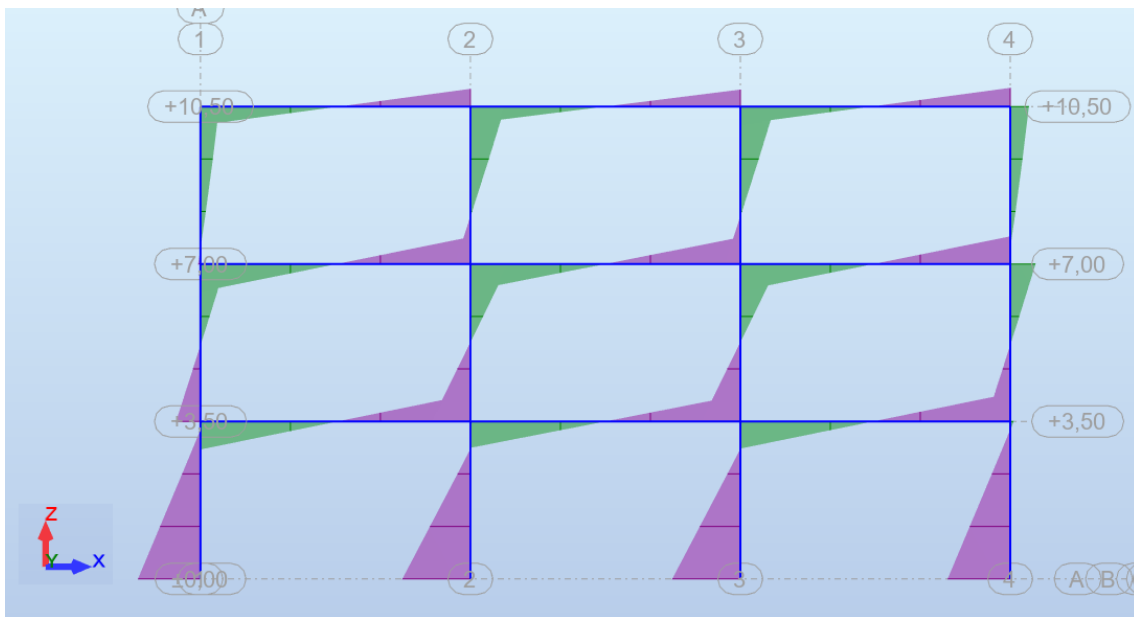


Figure B.19: 1.Column + 3.MRF beams - *MY* - 25:Seismic EC8 Direction X, Mode 1

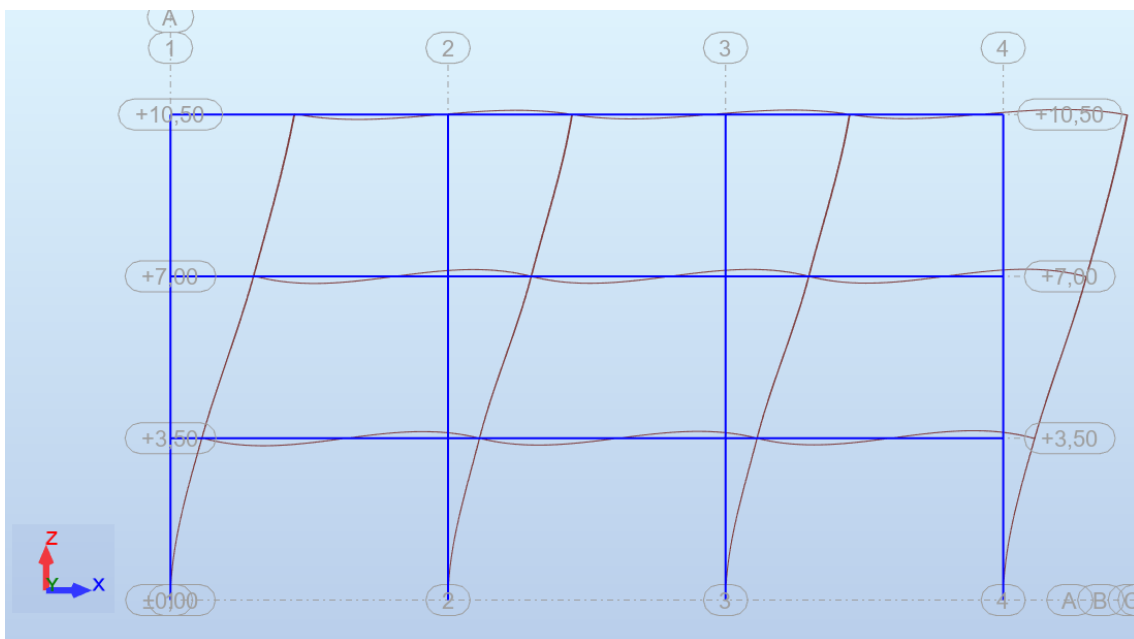


Figure B.20: 1.Column + 3.MRF beams - *DEFORMATION* - 25:Seismic EC8 Direction X, Mode 1

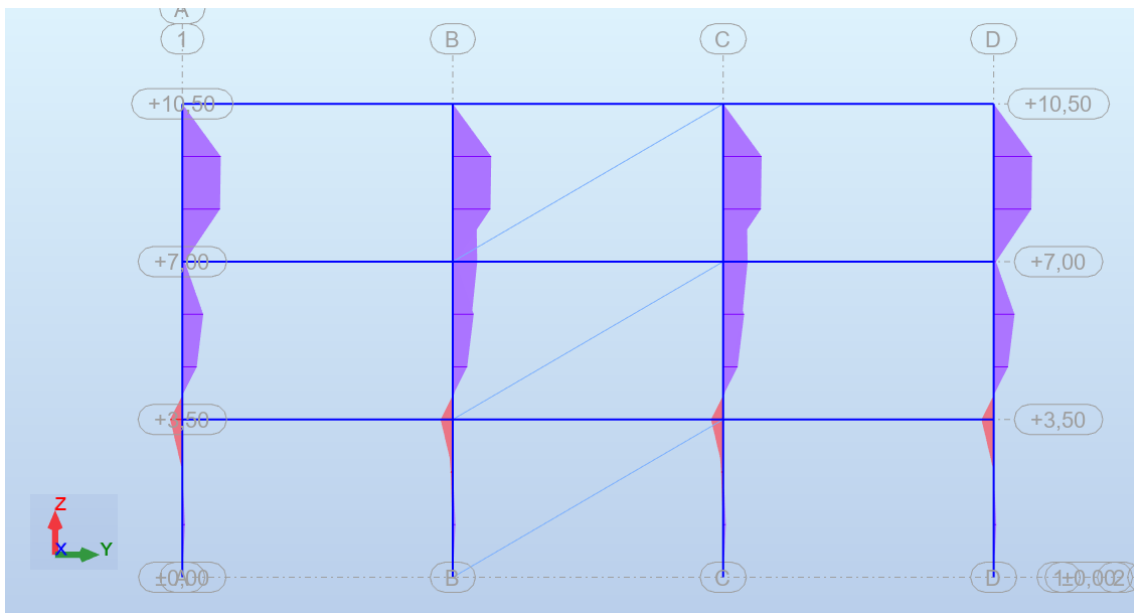


Figure B.21: 1.Columns + 2.CBF beams - *MZ* - 26:Seismic EC8 Direction Y, Mode 2

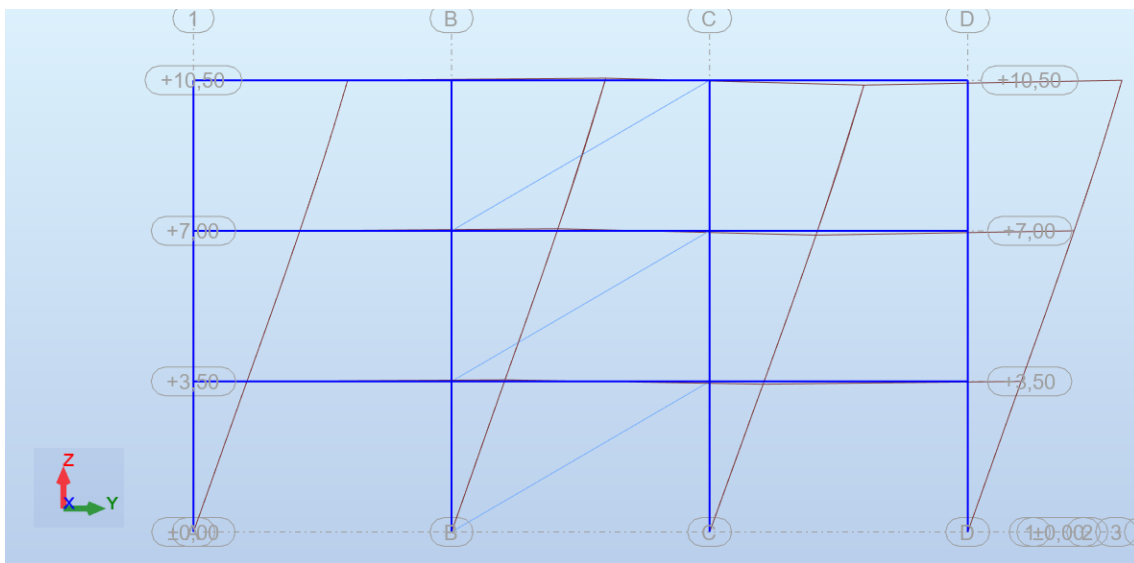


Figure B.22: 1.Columns + 2.CBF beams - *DEFLECTION* - 26:Seismic EC8 Direction Y, Mode 2

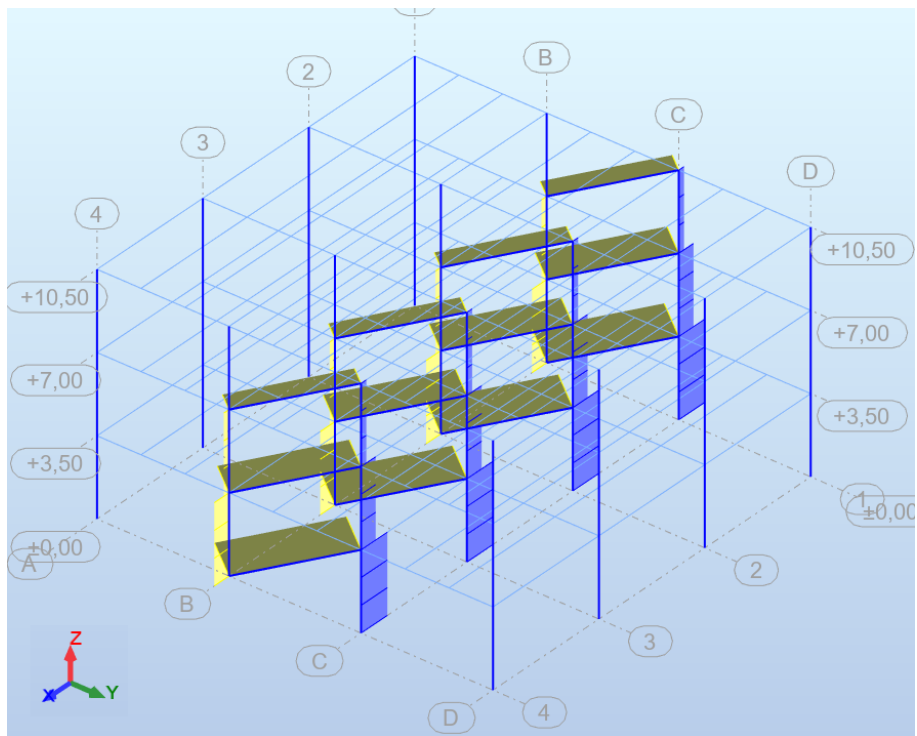


Figure B.23: 1.Columns + 5.Diagonals - FX - 26:Seismic EC8 Direction Y, Mode 2

C Non-linear computational model

The non-linear computational model used for performing the Pushover analysis is executed in SeismoStruct [2022] with educational license from AAU. The .SPF file can be provided by request. This appendix contains the applied vertical and lateral loads on the two planar models (MRF and CBF) and their quality assurance. The node and member numbers are shown as well.

C.1 Member and node numbers

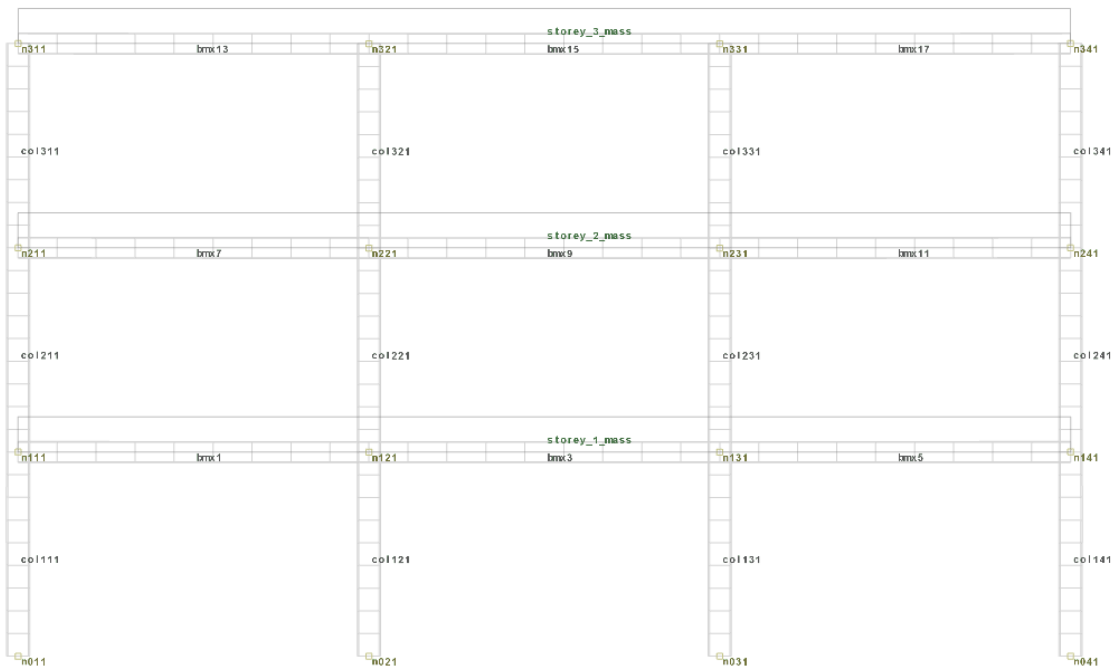


Figure C.1: Member and node numbers in MRF planar model in SeismoStruct

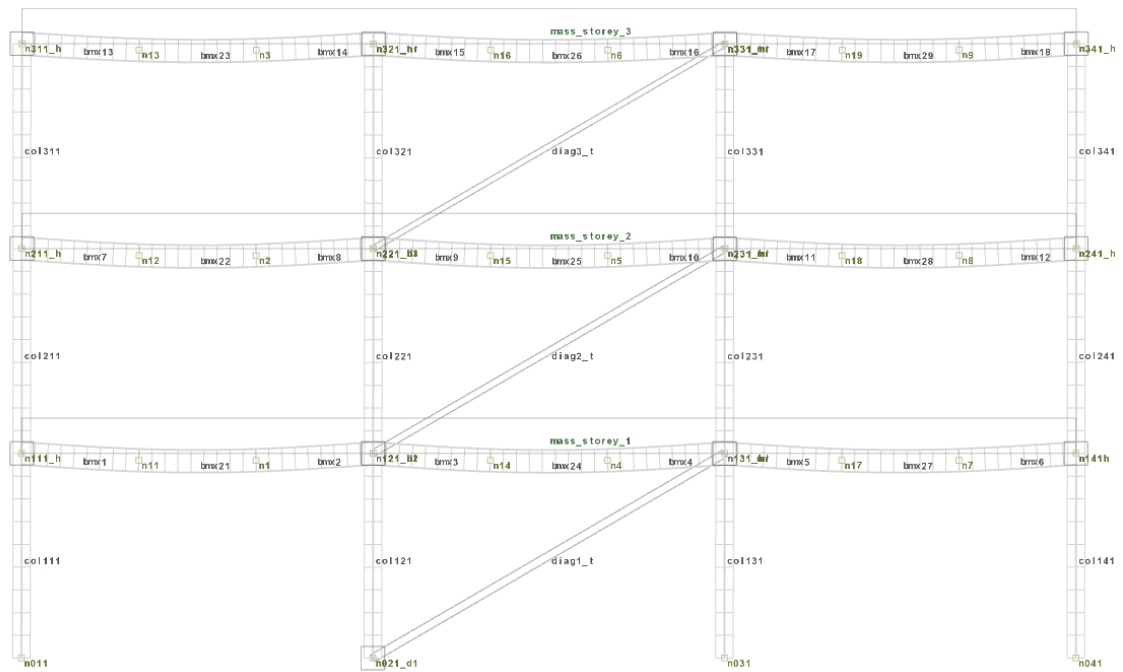


Figure C.2: Member and node numbers in CBF planar model in SeismoStruct

C.2 Vertical (gravity) loads

C.2.1 MRF



Figure C.3: Vertical (gravity) loads applied on the 2D MRF model in SeismoStruct [2022]. NOTE: self-weight of elements is automatic and not included here!

C.2.2 CBF



Figure C.4: Vertical (gravity) loads applied on the 2D CBF model in SeismoStruct [2022]. NOTE: self-weight of elements is automatic and not included here!

C.3 Lateral (incremental) loads

C.3.1 MRF

Table C.1: Method 1: mass proportional incremental load distribution (MRF)

Storey	Mass	Incremental load
i	m_i	$F_1^i = m_i$
-	[t]	[kN]
1	265	265
2	265	265
3	245	245

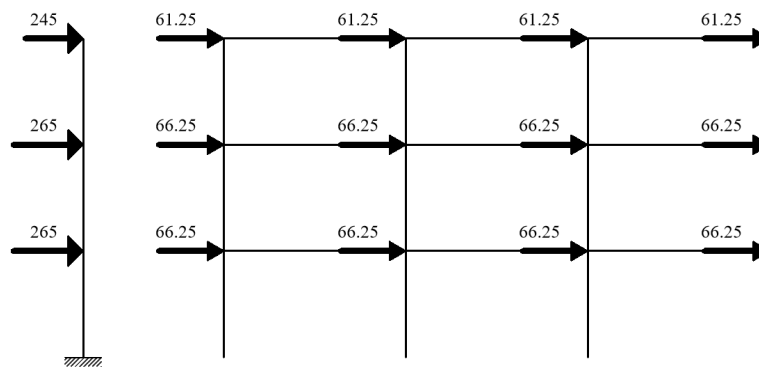


Figure C.5: Method 1: mass proportional incremental load distribution in the 2D MRF model in SeismoStruct [2022]

Table C.2: Method 2: incremental load distribution based on mode shape 1 (MRF)

Storey	Mass	Modal displ.	Normalized displ.	Incremental load
i	m_i	d_{m1}^i	Φ_1^i	$F_2^i = m_i \Phi_1^i$
-	[t]	[mm]	[-]	[kN]
1	265	0.42	0.25	66.25
2	265	1.12	0.67	177.55
3	245	1.67	1.00	245.00

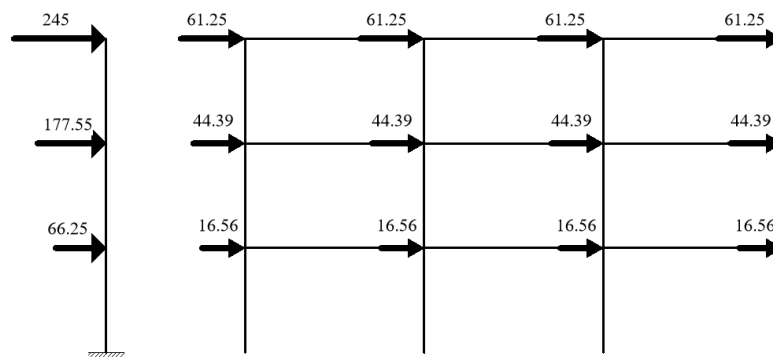


Figure C.6: Method 2: mode shape 1 proportional incremental load distribution in the 2D MRF model in SeismoStruct [2022]

C.3.2 CBF

Table C.3: Method 1: mass proportional incremental load distribution (CBF)

Storey	Mass	Incremental load
i	m_i	$F_1^i = m_i$
-	[t]	[kN]
1	265	265
2	265	265
3	245	245

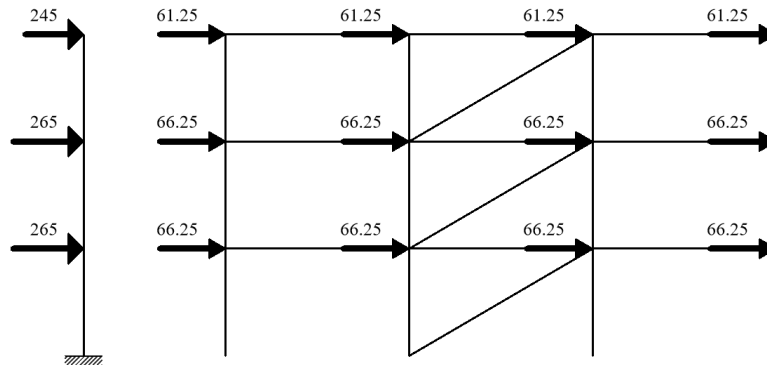


Figure C.7: Method 1: mass proportional incremental load distribution in the 2D CBF model in SeismoStruct [2022]

Table C.4: Method 2: incremental load distribution based on mode shape 2 (CBF)

Storey	Mass	Modal displ.	Normalized displ.	Incremental load
i	m_i	d_{m2}^i	Φ_2^i	$F_2^i = m_i \Phi_2^i$
-	[t]	[mm]	[-]	[kN]
1	265	0.56	0.35	92.75
2	265	1.11	0.69	182.85
3	245	1.61	1.00	245.00

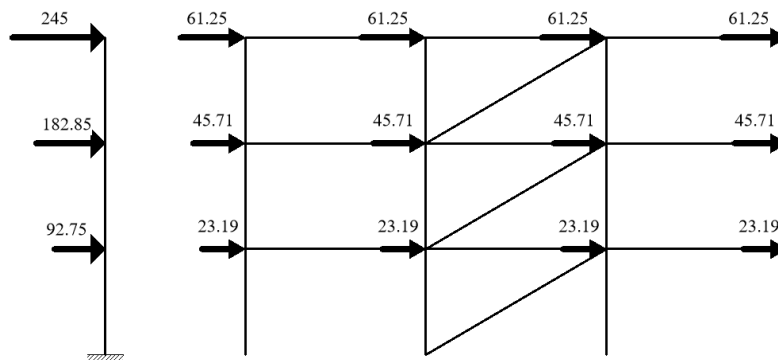


Figure C.8: Method 2: mode shape 2 proportional incremental load distribution in the 2D CBF model in SeismoStruct [2022]

C.4 Quality assurance (QA)

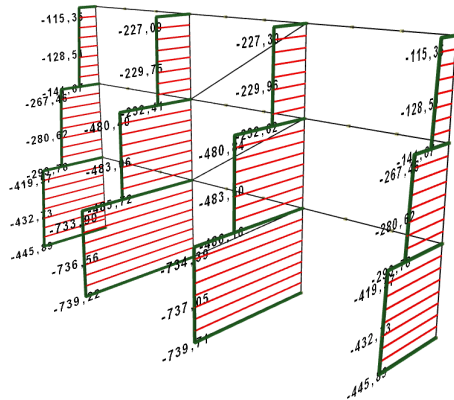


Figure C.9: Axial force diagrams in columns from seismic mass load combination [SeismoStruct, 2022]. Load factor = 0

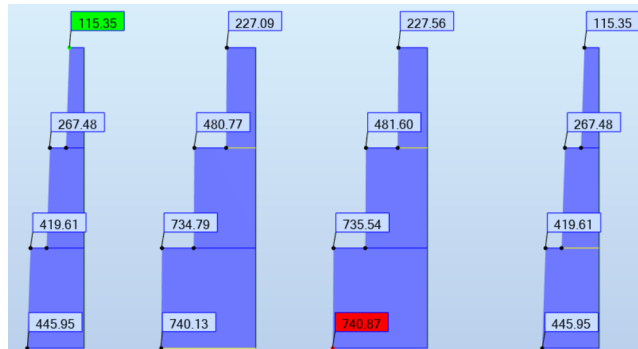


Figure C.10: Axial force diagrams in columns from seismic mass load combination [Autodesk Robot, 2021]

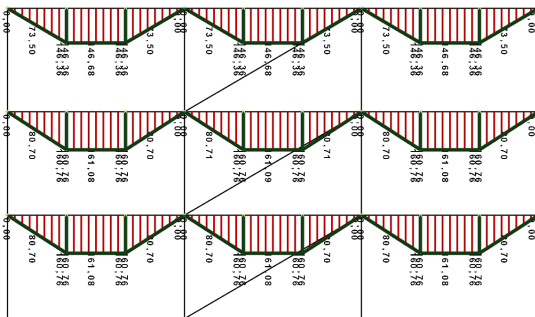


Figure C.11: Bending moment diagrams in CBF beams from seismic mass load combination [SeismoStruct, 2022]. Load factor = 0

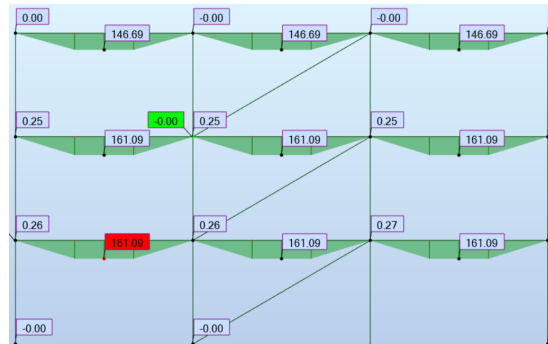


Figure C.12: Bending moment diagrams in CBF beams from seismic mass load combination [Autodesk Robot, 2021]

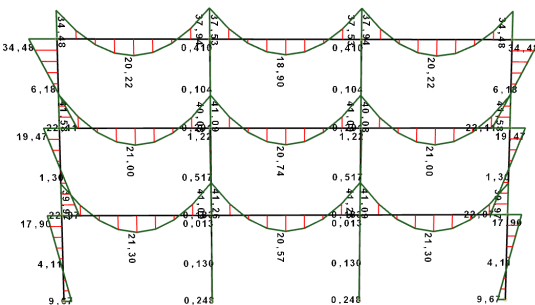


Figure C.13: Bending moment diagrams in MRF beams from seismic mass load combination [SeismoStruct, 2022]. Load factor = 0

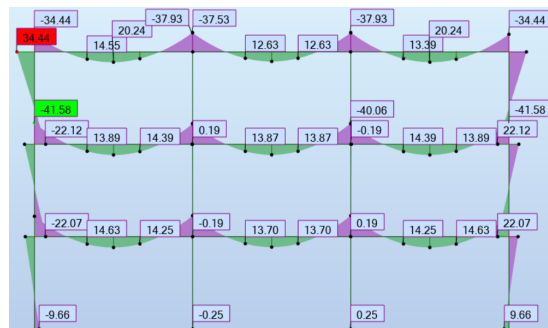


Figure C.14: Bending moment diagrams in MRF beams from seismic mass load combination [Autodesk Robot, 2021]

D Modal Response Spectrum Analysis

This appendix accompanies section 4.2 of the report in D.1 and chapter 5 in D.2 to D.6.

D.1 Theory

D.1.1 Forming of a response spectrum

The response spectrum is formed by recording the response (maximum acceleration) of SDOF systems with different stiffness to a set of earthquake time series (seismograms) as shown in figure D.1 below. By simplifying a MDOF structure to a SDOF one can obtain the maximum response (spectral acceleration $S(T_i)$) the structure will exhibit only by determining its dominant period T_i .

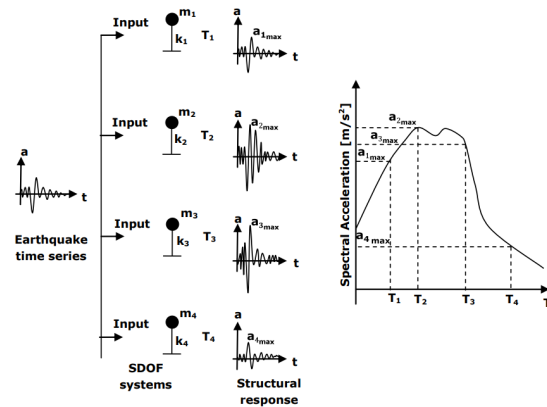


Figure D.1: Theory behind forming a response spectrum - illustrated [Nielsen, 2009]

D.1.2 Modal combination rules

The two used modal combination rules are shown in (D.1) and (D.2) below. SRSS is used to combine the response by direction and CQC - by mode shapes.

SRSS - square root of sum of squares

$$r = \sqrt{\sum_{i=1}^m r_{i,max}^2} \quad (D.1)$$

Where:

r	Response quantity (displacement, force, etc.)	[N/A]
m	Total number of investigated mode shapes	[-]

CQC - complete quadratic combination

$$r = \sqrt{\sum_{i=1}^m r_i^2 - \sum_{i=1}^m \sum_{j=1}^m \rho_{ij} r_i r_j} \quad \text{where} \quad \rho_{ij} = \frac{\xi^2 (1 - \beta_{ij})^2}{(1 - \beta_{ij})^2 + 4\xi^2 \beta_{ij}} \quad (\text{D.2})$$

Where:

r	Response quantity (displacement, force, etc.)	[N/A]
m	Total number of investigated mode shapes	[-]
ρ	Correlation coefficient taking into account the correlataion between the modes	[-]
ξ	Modal damping assumed the same for all modes	[-]
β_{ij}	Cyclic eigenfrequency ratio between mode shape i and j	[-]

D.1.3 EN1998-1 [2004] response spectrum

In EN1998-1 [2004] the response spectra is formed on the basis of what was previously discussed in Appendix D.1.1. However, it also takes into account the influence of the different parameters mentioned below:

- Soil conditions - soil type $A - E$ and soil factor S (tables below)
- Site conditions - spectra type 1 – 3 (tables below)
- Expected ground acceleration at the site a_g (D.3)
- Structural damping - most often taken as 5% for which $\eta = 1$ in (D.3).
- Behaviour factor q - the larger it is the more the design response spectra (D.7) is reduced from the elastic one - discussed in more detail in section 4.4.1.

Spectra parameters

Table D.1: Type 1 elastic response spectrum parameters [EN1998-1-BGNA, 2012]

Ground type	Soil factor S	Spectral periods		
		T_B	T_C	T_D
[–]	[–]	[s]	[s]	[s]
A	1	0.1	0.3	2.0
B	1.3	0.1	0.4	2.0
C	1.2	0.1	0.5	2.0
D	1.0	0.1	0.6	2.0
E	1.2	0.1	0.5	2.0

Table D.2: Type 2 elastic response spectrum parameters [EN1998-1-BGNA, 2012]

Ground type	Soil factor S	Spectral periods		
		T_B	T_C	T_D
[–]	[–]	[s]	[s]	[s]
A	1.00	0.05	0.25	1.20
B	1.35	0.05	0.25	1.20
C	1.50	0.10	0.25	1.20
D	1.80	0.10	0.30	1.20
E	1.60	0.05	0.25	1.20

Table D.3: Type 3 elastic response spectrum parameters [EN1998-1-BGNA, 2012]

Ground type	Soil factor S	Spectral periods		
		T_B	T_C	T_D
[–]	[–]	[s]	[s]	[s]
ALL	1.0	0.2	1.0	2.0

Horizontal elastic response spectra formulae

$$0 \leq T \leq T_B : \quad S_e(T) = a_g S \left(1 + \frac{T}{T_B} (\eta 2.5 - 1) \right) \quad (\text{D.3})$$

$$T_B \leq T \leq T_C : \quad S_e(T) = a_g S \eta 2.5 \quad (\text{D.4})$$

$$T_C \leq T \leq T_D : \quad S_e(T) = a_g S \eta 2.5 \left(\frac{T_C}{T} \right) \quad (\text{D.5})$$

$$T_D \leq T \leq 4s : \quad S_e(T) = a_g S \eta 2.5 \left(\frac{T_C T_D}{T^2} \right) \quad (\text{D.6})$$

where:

$S_e(T)$ is the elastic response spectrum

T is the vibration period of a linear single-degree-of-freedom system

a_g is the design ground acceleration on a given ground type. For the prototype structure it is $a_g = \gamma a_{gR} = 0.32 \text{ g}$ (see subsection 5.4.2)

T_B is the lower limit of the period of the constant spectral acceleration branch (tables D.1 to D.3)

T_C is the upper limit of the period of the constant spectral acceleration branch (tables D.1 to D.3)

T_D is the value defining the beginning of the constant displacement response range of the spectrum (tables D.1 to D.3)

S is the soil factor (tables D.1 to D.3)

η is the damping correction factor with a reference value of $\eta = 1$ for 5% viscous damping

Horizontal design response spectra formulae

$$0 \leq T \leq T_B : \quad S_d(T) = a_g S \left(\frac{2}{3} + \frac{T}{T_B} \left(\frac{2.5}{q} - \frac{2}{3} \right) \right) \quad (\text{D.7})$$

$$T_B \leq T \leq T_C : \quad S_d(T) = a_g S \left(\frac{2.5}{q} \right) \quad (\text{D.8})$$

$$T_C \leq T \leq T_D : \quad S_d(T) = \text{MAX} \left(a_g S \frac{2.5 T_C}{q T} ; \beta a_g \right) \quad (\text{D.9})$$

$$T_D \leq T : \quad S_d(T) = \text{MAX} \left(a_g S \frac{2.5 T_C T_D}{q T^2} ; \beta a_g \right) \quad (\text{D.10})$$

where:

a_g, S, T_C, T_D are defined in subsection D.1.3 above and their values shown in tables D.1 to D.3

$S_d(T)$ is the design spectrum

q is the behaviour factor

β is the lower bound factor for the horizontal design spectrum recommended as 0.2

D.2 Basic period check using the Rayleigh quotient

As previously mentioned the Rayleigh quotient is the ratio between the elastic and kinetic energies as shown in (D.11).

$$\omega^2 = \frac{E_{Elastic}}{E_{Kinetic}} \implies T = 2\pi \sqrt{\frac{E_{Kinetic}}{E_{Elastic}}} = 2\pi \sqrt{\frac{\sum_{i=1}^3 (m_i d_i^2)}{\sum_{i=1}^3 (F_i d_i)}} \quad (D.11)$$

Equation (D.11) above can be extended for each orthogonal direction with i being the storey number as shown in (D.12) below. The used values are shown in table D.4 and illustrated in figure D.2. It is decided to use a triangular distribution for defining the fictional force F_i .

$$T_1 = 2\pi \sqrt{\frac{\sum_{i=1}^3 (m_i d_{i,x}^2)}{\sum_{i=1}^3 (F_{i,x} d_{i,x})}} = 0.68 \text{ s} \quad \text{and} \quad T_2 = 2\pi \sqrt{\frac{\sum_{j=1}^m (m_j d_{j,y}^2)}{\sum_{i=1}^3 (F_{i,y} d_{i,y})}} = 0.57 \text{ s} \quad (D.12)$$

Table D.4: Rayleigh method: calculation parameters

Storey	Mass	Fictional force	Storey displacement	
i	m_i	$F_{i,x} = F_{i,y}$	$d_{i,x}$	$d_{i,y}$
	[t]	[kN]	[m]	[m]
3	245	1000	0.048	0.032
2	265	670	0.032	0.022
1	265	330	0.012	0.011

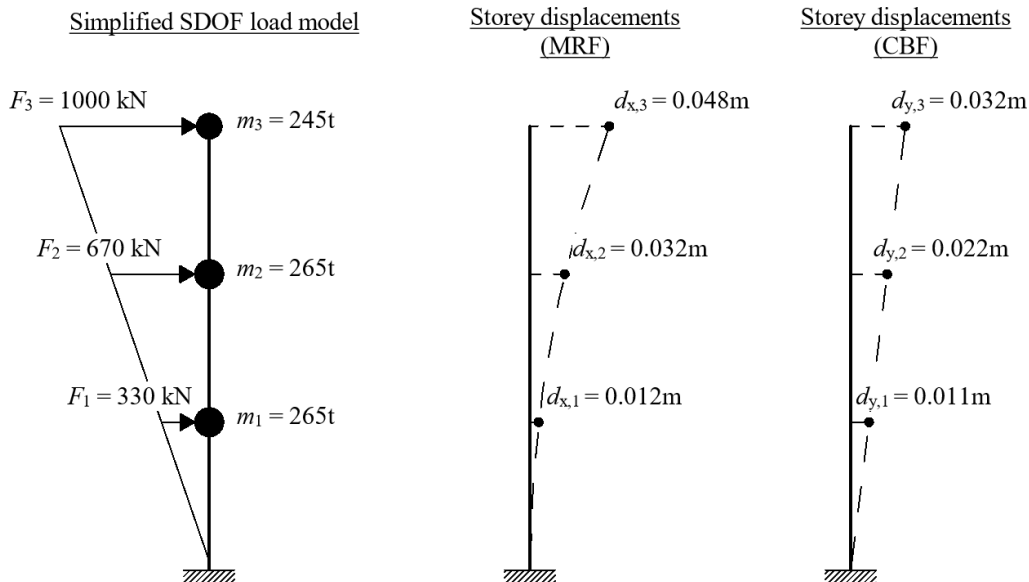


Figure D.2: Rayleigh method: distribution of fictional static forces on floors and corresponding response of MRF and CBF

D.3 Sensitivity study: choice of response spectrum

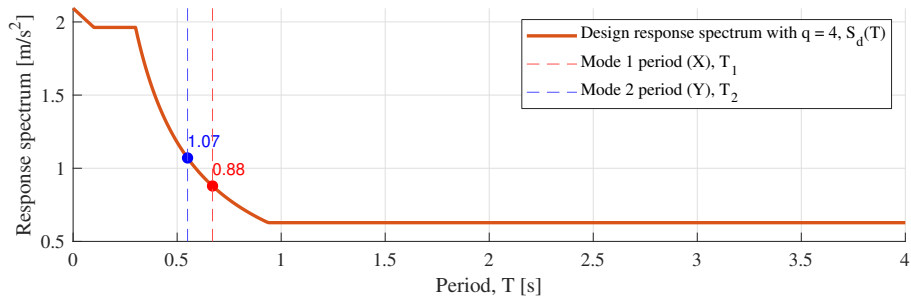


Figure D.3: Design horizontal response spectra. Type 1 and ground type A.

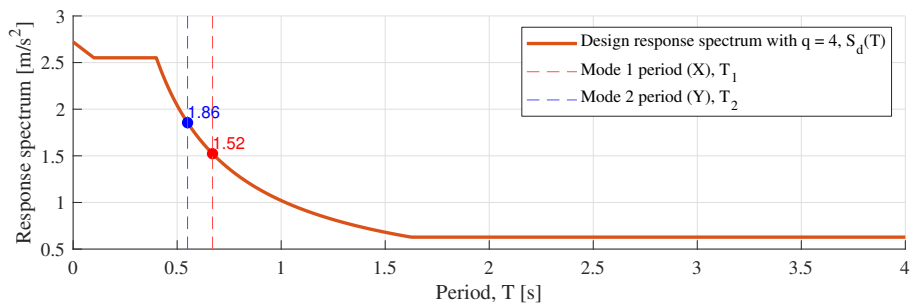


Figure D.4: Design horizontal response spectra. Type 1 and ground type B.

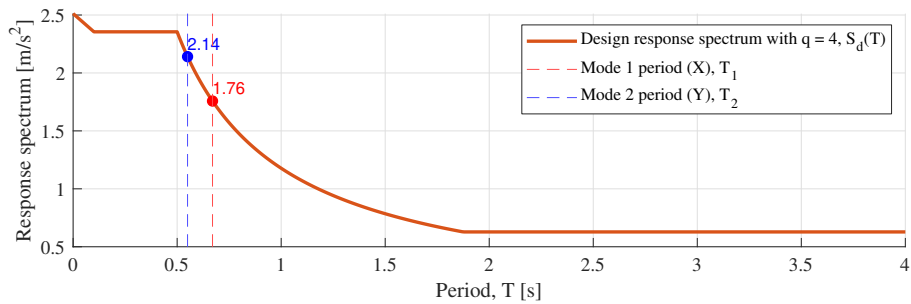


Figure D.5: Design horizontal response spectra. Type 1 and ground type C,E.

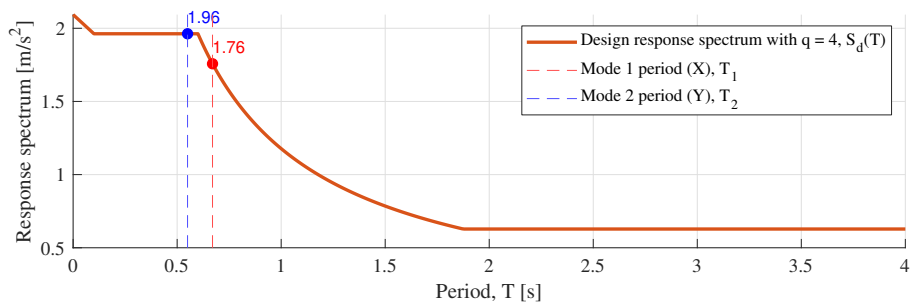


Figure D.6: Design horizontal response spectra. Type 1 and ground type D.

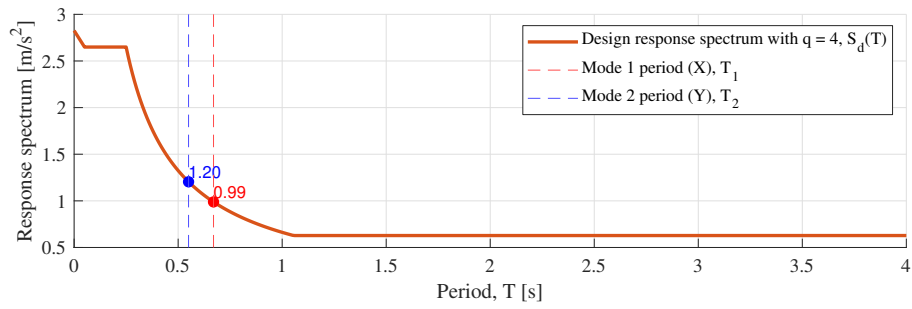


Figure D.7: Design horizontal response spectra. Type 2 and ground type B.

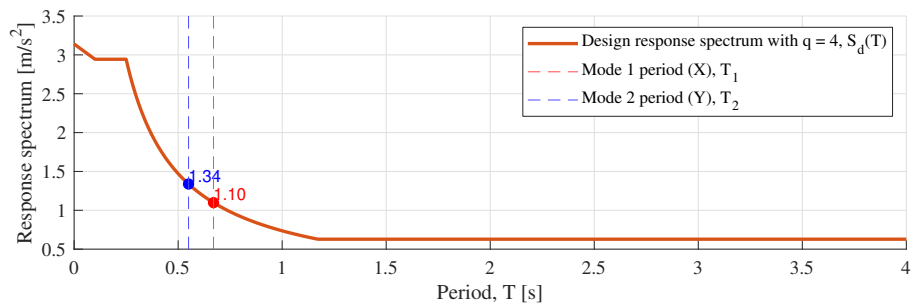


Figure D.8: Design horizontal response spectra. Type 2 and ground type C.

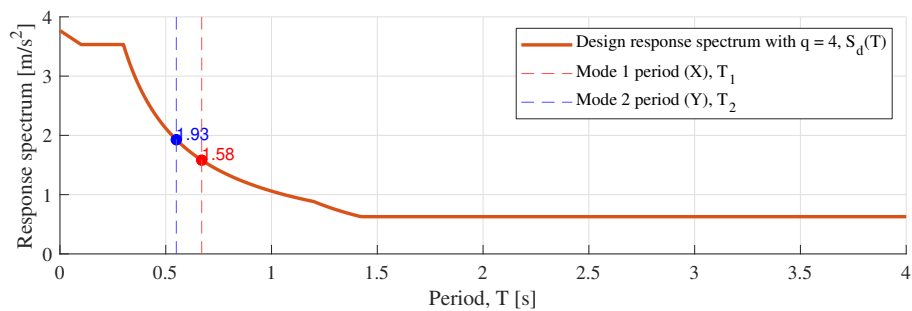


Figure D.9: Design horizontal response spectra. Type 2 and ground type D.

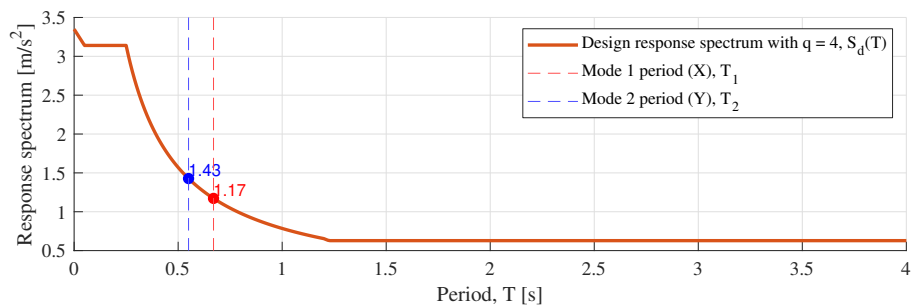


Figure D.10: Design horizontal response spectra. Type 2 and ground type E.

D.4 Base shear quality assurance

The lower and upper bounds of the base shear are calculated in (D.14) below.

Base shear upper and lower boundaries according to Bisch et al. [2011]

$$F_{b,x,LB} = \frac{m_{eff,x,1}}{m_{dyn}} S_d(T_1) m_{dyn} \leq F_{b,x} \leq F_{b,x,UB} = S_d(T_1) m_{dyn} \quad (D.13)$$

$$F_{b,y,LB} = \frac{m_{eff,y,2}}{m_{dyn}} S_d(T_2) m_{dyn} \leq F_{b,y} \leq F_{b,y,UB} = S_d(T_2) m_{dyn} \quad (D.14)$$

Where:

$\frac{m_{eff}}{m_{dyn}}$	Mass participation ratio shown in table 5.6	[-]
m_{dyn}	Total dynamic mass as shown in (5.1)	[kg]
T_1	Eigenperiod of mode shape 1 (dominant in x)	[s]
T_2	Eigenperiod of mode shape 2 (dominant in y)	[s]
$S_d(T_i)$	Design spectrum (D.15)	[m/s ²]
F_b	Base shear shown in figures 5.10 and 5.10	[kN]

As discussed in subsection 5.4.3 response spectrum type 1 and soil type C/E is used with $T_C = 0.1$ s and $T_D = 2.0$ s (see table D.1). This means that $S_d(T)$ is calculated according to (D.9) since $T_1 = 0.67$ s and $T_2 = 0.55$ s.

$$.S_d(T_1) = 1.76 \text{ m/s}^2 \quad S_d(T_2) = 2.14 \text{ m/s}^2 \quad (D.15)$$

The total seismic mass is $m_{dyn} = 775$ t (5.1). The mass participation ratio for mode 1 and 2 is defined as 79.90 % and 85.45 % respectively (table 5.6). Using these values the upper and lower bounds of the base shear is calculated and summarized table D.5 below.

Table D.5: Check of base shear

Direction	Lower bound $F_{b,LB} = S_d(T_i) m_{eff}$ [kN]	Calculated F_b [kN]	Upper bound $F_{b,UB} = S_d(T_i) m_{dyn}$ [kN]
X	1088	1124	1362
Y	1416	1416	1659

D.5 Prototype sensitivity to second order effects

Parameters		Storey 1	Storey 2	Storey 3	Unit	Reference	
Calculation input	Design interstorey drift UX	d_{rx}	26,41	43,00	34,00	mm	Case 25 Mode 1, q=4
	Design interstorey drift UY	d_{ry}	30,28	29,44	26,81	mm	Case 26 Mode 2, q=4
	Dynamic mass on and above the given storey	m_{dyn}	7601	5198	2599	kN	Case 101:mass
	Seismic shear on the storey in x-dir	$V_{tot,x}$	1124	946	582	kN	Case 25 Mode 1
	Seismic shear on the storey in y-dir	$V_{tot,y}$	1416	1156	683	kN	Case 26 Mode 2
General building info	Interstorey height	h	3500	3500	3500	mm	Robot model
	Reduction coefficient (class 2)	v	0,5	0,5	0,5	-	Assumption

Figure D.11: Calculation parameters for the EC8-1 checks shown in figures D.12 and D.13

Parameters		Storey 1	Storey 2	Storey 3	Reference
Buildings with weak (soft) NSE attached to the structure	$d_{rx} v \leq 0,005 h$	75%	123%	97%	EC8-1, 4.4.3.2 (4.31)
	$d_{ry} v \leq 0,005 h$	87%	84%	77%	
Buildings with ductile NSE	$d_{rx} v \leq 0,0075 h$	50%	82%	65%	EC8-1, 4.4.3.2 (4.32)
	$d_{ry} v \leq 0,0075 h$	58%	56%	51%	
Buildings without NSE	$d_{rx} v \leq 0,010 h$	38%	61%	49%	EC8-1, 4.4.3.2 (4.33)
	$d_{ry} v \leq 0,010 h$	43%	42%	38%	

Figure D.12: Sensitivity to second order effects check according to EC8-1

D.6 Prototype damage limitation

Parameters		Storey 1	Storey 2	Storey 3	Reference
x-direction (MRF)	$\theta_x = (m_{dyn} / V_{tot,x}) (d_{rx} / h)$	0,051	0,067	0,043	EC8-1, 4.4.2.2(2) (4.28) $\theta \leq 0,1$
y-direction (CBF)	$\theta_y = (m_{dyn} / V_{tot,y}) (d_{ry} / h)$	0,046	0,038	0,029	

Figure D.13: Damage limitation check according to EC8-1 (see also figure D.11)

E Pushover analysis

This Appendix contains the details about the theory behind the Pushover analysis. It accompanies section 4.3 of the report.

E.1 Theory

The Pushover analysis works by monotonically increasing a set of static lateral forces on a non-linear numerical model with constant gravity loads. With increase of lateral loading, the response of the structure can be visualized through a capacity curve (top displacement - base shear).

As a first step a lateral load distribution type must be chosen. According to EN1998-1 [2004] the following two types must be studied and the one that yields the most conservative result for the given investigation must be used (see also figure E.1):

1. Mass proportional (uniform) load distribution. This distribution assumes constant acceleration along the structure height which means that the lateral loads are proportional to the mass on each storey i . The force is obtained as $F_1^i = m_i$.
2. Modal load distribution assumes acceleration which is proportional to the fundamental mode shape m . In this case the normalized displacement Φ_m^i from the modal analysis of mode shape m is used to obtain the lateral force as $F_2^i = m_i \Phi_m^i$.

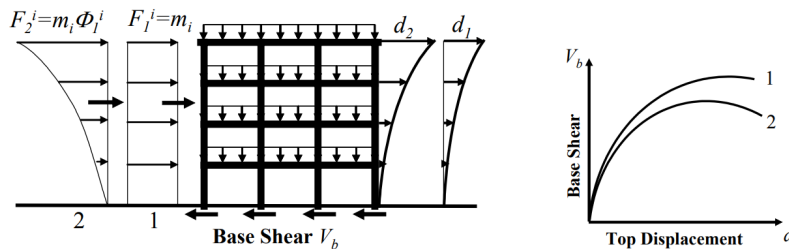


Figure E.1: Load distributions methods according to EN1998-1 [2004] and the corresponding pushover response curves [Spacone et al., 2010]

This method is developed further in EN1998-1 [2004] by equating the MDOF response to one of a SDOF system. This is done in order to determine the necessary demands of the structure by later equating it to the demand curve. However, in the Thesis, these demands are not relevant since only the raw structural response is investigated and used to choose the capacity and stroke of the actuators. Nevertheless, for a better overview it was decided to show the response of the equivalent SDOF system in a pushover curve in the report. This is why the theory for acquiring the parameters for the SDOF equivalent response is briefly described on the following page.

As previously mentioned, the response of the structure must be simplified to the response of an equivalent SDOF system which can then be used to acquire its target displacement d_t^* . For this purpose a transformation factor Γ is defined as shown in figure E.2 and used to obtain the force and displacement of the equivalent SDOF system - F^* and d^* respectively.

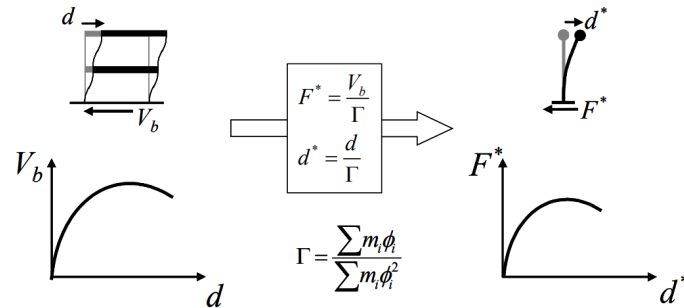


Figure E.2: Transforming the pushover curve to SDOF response [Spacone et al., 2010]

The idealised elasto-perfectly plastic force-displacement relationship for the SDOF system is determined using the equal energy method as shown in figure E.3 below. This means that the stiffness (slope) of the initial (elastic) part of the curve is determined so that the areas under the actual and idealised force-deformation curves are equal. From there the yield displacement of the idealised SDOF system d_y^* can be determined as shown in (E.1) below:

$$d_y^* = 2 \left(d_m^* - \frac{E_m^*}{F_y^*} \right) \tag{E.1}$$

Where F_y^* represents the ultimate strength of the SDOF system and is equal to the base shear at which the plastic mechanism A is formed (i.e. $\max F_b$) and E_m^* - the deformation energy up to the formation of the plastic mechanism.

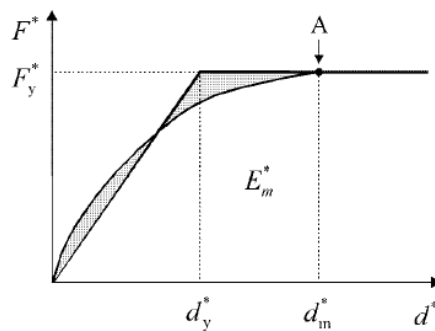


Figure E.3: Idealised elasto - perfectly plastic force-displacement relationship of the SDOF system. [EN1998-1, 2004]

One can then estimate the initial elastic period of the idealised system as show in (E.2) below

$$T^* = 2\pi \sqrt{\frac{m^* d_y^*}{F_y^*}} \tag{E.2}$$

The target displacement of the SDOF system can then be calculated as shown in (E.3) and (E.4) below. The equations are illustrated in figure E.4

$$d_t^* = S_e \left(\frac{T^*}{2\pi} \right)^2 \quad \text{for} \quad T^* \geq T_C \quad (\text{E.3})$$

$$d_t^* = S_e \left(\frac{T^*}{2\pi} \right)^2 \frac{1}{q_u} \left(1 + (q_u - 1) \frac{T_C}{T^*} \right) \quad \text{for} \quad T^* < T_C \quad (\text{E.4})$$

where $q_u = \frac{S_e(T^*)m^*}{F_y^*}$ and $m^* = \sum_{i=1}^{n_{storeys}} m_i \Phi_i$

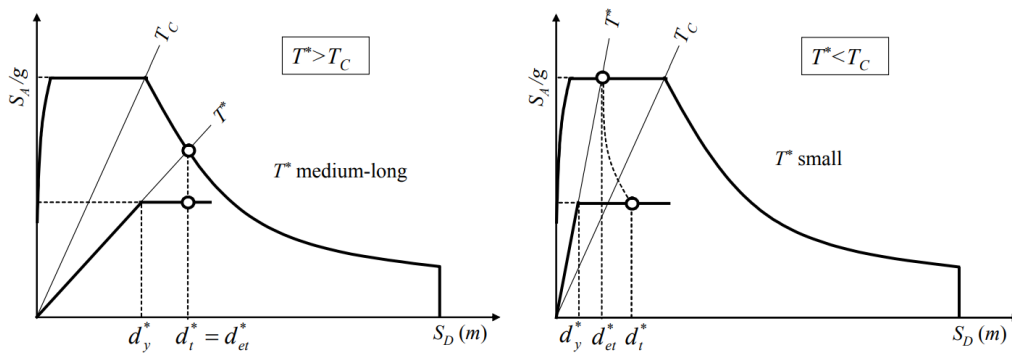


Figure E.4: Transforming Pushover curve into SDOF response [Spacone et al., 2010]

The target displacement can be obtained for the pushover curve (MDOF space) by multiplying the SDOF displacement d_t^* with the transformation factor Γ defined in figure E.2.

F Prototype Capacity Design

This Appendix accompanies chapter 6 of the report. It contains the detail calculations behind the CD rules for CBF and MRF rules set in EN1998-1 [2004] and EN1993-1-1 [2007].

F.1 CBF

This part of the Appendix accompanies section 6.1 of the report. A short summary of its content is provided below:

- **Subsection F.1.1** contains general information for the material properties, used safety factors and the general cross sectional geometry of the CBF diagonals.
- **Subsection F.1.2** contains the calculation behind all necessary checks for CBF according to EC8-1. It also includes the calculated factor for verifying the non-dissipative CBF columns and beams (CD combinations).

F.1.1 General

Parameter		Storey 1 CFSHS 140x4	Storey 2 CFSHS 120x4	Storey 3 CFSHS 100x3	Unit	Reference
Young's modulus	$E =$	21000000,00	21000000,00	21000000,00	N/cm ²	RSA
Characteristic yield strength	$f_y =$	23500,00	23500,00	23500,00	N/cm ²	RSA
Overstrength factor	$\gamma_{ov} =$	1,25			-	EC8-1, 6.2(3)
Material correction factor	$\varepsilon = \sqrt{(23500 / f_y)} =$	1,00	1,00	1,00	-	EC3-1, 6.3.1.3 (6.50)

Figure F.1: Material properties and safety factors

Parameter		Storey 1 CFSHS 140x4	Storey 2 CFSHS 120x4	Storey 3 CFSHS 100x3	Unit	Reference
Second moment of area	$I_z =$	652,00	402,00	177,00	cm ⁴	http://eurocode.b
Radius of gyration	$i_z =$	5,52	4,71	3,94	cm	g/sections/sec-lib.html
Cross sectional area	$A =$	21,30	18,10	11,40	cm ²	lib.html
Buckling length	$L_{cr} =$	695,00	695,00	695,00	cm	RSA

Figure F.2: General geometry

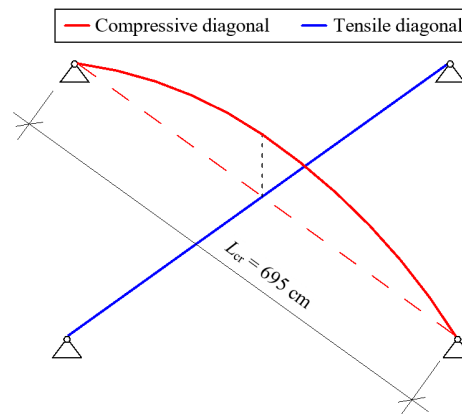


Figure F.3: Design principle used for determining L_{cr}

F.1.2 Calculation

Parameter		Storey 1 CFSHS 140x4	Storey 2 CFSHS 120x4	Storey 3 CFSHS 100x3	Unit	Reference
Elastic critical force	$N_{cr} = (\pi^2 EI_z) / L_{cr}^2 =$	279767,35	172494,59	75949,11	N	EC3-1, 6.3.1.2 (6.49)
Non-dimensional slenderness	$\lambda = \sqrt{(Af_y / N_{cr})} =$	1,34	1,57	1,88	-	
Slenderness 1	$\lambda_1 = 93,9\epsilon =$	93,90	93,90	93,90	-	
Max. allowed radius of gyration	$i_{z,max} = L_{cr} / 1,3\lambda_1 =$	5,69	5,69	5,69	cm	EC3-1, 6.3.1.3 (6.50)
Min. allowed radius of gyration	$i_{z,min} = L_{cr} / 2\lambda_1 =$	3,70	3,70	3,70	cm	
Overstrength for diagonals	$\Omega_i = N_{pl,Rd} / N_{Ed,tension,max} =$	1,18	1,16	1,30	-	RSA + EC8-1, 6.7.4 (6.12)
Angle of tensile diagonals for each seismic direction	$\alpha_1 =$	30,30	30,30	30,30	deg	EC8-1, 6.7.1 (6.11)
	$\alpha_2 =$	30,30	30,30	30,30	deg	
Areas of horizontal projections of the cross sections of the tensile diagonals for each seismic	$A^+ = A \cos(\alpha_1) =$	18,39	15,63	9,84	cm ²	EC8-1, 6.7.1 (6.11)
	$A^- = A \cos(\alpha_2) =$	18,39	15,63	9,84	cm ²	
Load deflection characteristics requirement	$ A^+ - A^- / (A^+ + A^-) \leq 0,05$	TRUE	TRUE	TRUE		EC8-1, 6.7.1 (6.11)
Slenderness requirement	$1,3 < \lambda \leq 2,0$	TRUE	TRUE	TRUE		EC8-1, 6.7.3(1)
	$i_{z,min} < i_z < i_{z,max}$	TRUE	TRUE	TRUE		
Homogeneous dissipative behaviour requirement	$max(\Omega_i) \leq 1,25 min(\Omega_i)$	TRUE				EC8-1, 6.7.3 (8)
Factor for multiplying axial seismic forces on columns and beams	$1,1 \gamma_{ov} min(\Omega_i) =$	1,60				

Figure F.4: Calculation and check of EC8-1 CBF design requirements

F.2 MRF

This part of the Appendix accompanies section 6.2 of the report. A short summary of its content is provided below:

- **Subsection F.2.1** contains general information for the material properties, used safety factors and the general cross sectional geometry of the MRF beams and columns.
- **Subsection F.2.2** contains the check for the beam's plastic moment, axial and shear resistances.
- **Subsection F.2.3** contains the check for the lateral stability of the beam segment.
- **Subsection F.2.4** contains the SCWB check.
- **Subsection F.2.5** contains the check for the column's plastic shear resistance.
- **Subsection F.2.6** contains the panel zone check.
- **Subsection F.2.7** contains the calculated factor for verifying the non-dissipative MRF columns (CD combinations).

F.2.1 General

Parameter		Beams IPE 360	Columns HEB400	Unit	Reference
Young's modulus	$E =$	210000,00	210000,00	N/mm ²	RSA
Characteristic yield strength	$f_y =$	235,00	460,00	N/mm ²	
Characteristic yield strength of the web	$f_{yw} =$	235,00	460,00	N/mm ²	Depends on the thickness
Characteristic yield strength of the flange	$f_{yf} =$	235,00	440,00	N/mm ²	
Material correction factor	$\varepsilon = \sqrt{(235 / f_y)} =$	1,00	0,71	-	EC3-1, 6.3.1.3 (6.50)
Overstrength factor	$\gamma_{ov} =$		1,25	-	EC8-1, 6.2(3)
Partial safety factor for resistance of members to instability assessed by member checks	$\gamma_{M1} =$		1,05	-	EC3-1 BGNA, NA.2.14, 6.1
Partial safety factor for resistance of cross sections whatever the class is	$\gamma_{M0} =$		1,05	-	

Figure F.5: Material properties and safety factors

Parameter		Beams IPE 360	Columns HEB400	Unit	Reference
Plastic moment of inertia	$W_{pl} =$	1020000,00	3240000,00	mm ³	http://eurocode.bg/sections/section-lib.html
Torsion constant	$I_t =$	375000,00	3570000,00	mm ⁴	
Radius of gyration	$i_z =$	37,90	74,00	mm	
Cross sectional area	$A =$	7270,00	19800,00	mm ²	
Cross sectional height	$h; d =$	360,00	400,00	mm	
Cross sectional width	$b =$	170,00	300,00	mm	
Radius	$r =$	18,00	27,00	mm	
Flange thickness	$t_f =$	12,70	24,00	mm	
Web thickness	$t_w =$	8,00	13,50	mm	
Mid web-web distance (moment arm)	$z =$	347,30	N/A	mm	
Shear area only for I and H sections	$A_v =$	3510,80	7020,00	mm ²	EC3-1, 6.2.6 (6.18)

Figure F.6: General cross sectional geometry

F.2.2 Beam plastic capacity

Parameter		Beams IPE 360	Unit	Reference
Total length	$L =$	6,00	m	RSA
Distance between the plastic hinges	$L_h =$	5,60	m	Assumption
Effective width (distance between secondary beams)	$d_f =$	2,00	m	RSA
Dynamic mass in seismic combination (planar load)	$mass = G_k + \psi_2 Q_k =$	8,02	kN/m ²	
Plastic moment resistance	$M_{pl,Rd,b} =$	239,70	kNm	EC3-1, 6.2.5 (6.13)
Plastic moment resistance in end section A	$M_{pl,Rd,A} =$	239,70	kNm	
Plastic moment resistance in end section B	$M_{pl,Rd,B} =$	239,70	kNm	
Plastic axial resistance	$N_{pl,Rd,b} =$	1627,10	kN	EC3-1, 6.2.3 (6.6)
Plastic shear resistance	$V_{pl,Rd,b} =$	453,65	kN	EC3-1, 6.2.6 (6.18)
Design bending moment	$M_{Ed,b} =$	121,26	kNm	Combo 404 non CD
Design axial force	$N_{Ed,b} =$	0,00	kN	
Design shear due to application of the plastic moments at section A and B	$V_{EdM} = (M_{pl,Rd,A} + M_{pl,Rd,B}) / L_h =$	85,61	kN	EC8-1, 6.6.2(2)
Design shear only due to the dynamic mass	$V_{Ed,G} = (mass \cdot d_f \cdot L_h) / 2 =$	44,91	kN	
Total design shear taking into account plastic moment distribution	$V_{Ed,b} = V_{Ed,G} + V_{EdM} =$	130,52	kN	
Checking beam plastic moment resistance	$M_{Ed,b} / M_{pl,Rd,b} \leq 1,0$	51%		EC8-1, 6.6.2(2) (6.2)
Checking beam plastic axial resistance	$N_{Ed,b} / N_{pl,Rd,b} \leq 0,15$	0%		EC8-1, 6.6.2(2) (6.3)
Checking beam plastic shear resistance	$V_{Ed,b} / V_{pl,Rd,b} \leq 0,5$	29%		EC8-1, 6.6.2(2) (6.4) + (6.5)

Figure F.7: Beam plastic moment, axial and shear capacity check

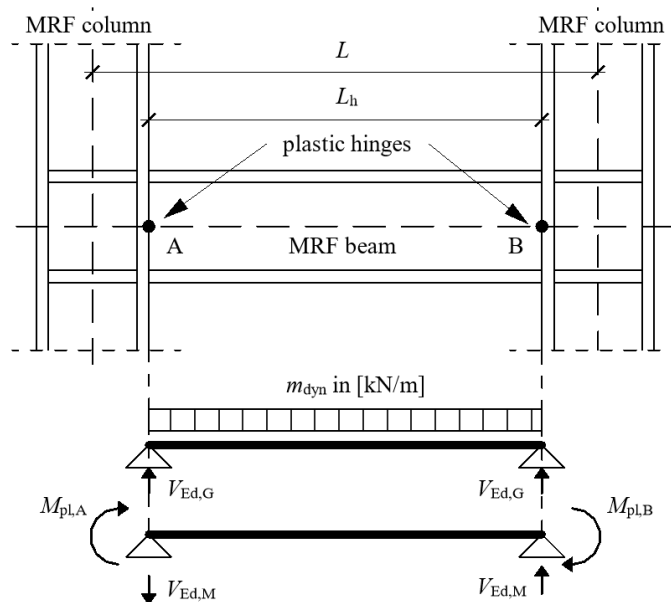


Figure F.8: Determining the design shear when the MRF beam plastifies at its both ends

F.2.3 Beam segment lateral stability

The beam segment is concluded as not being laterally stable. Please refer back to subsection 6.2.1 for the design measurements undertaken towards its stabilization.

Parameter		Beams IPE 360	Unit	Reference
Plastic moment resistance	$M_{pl,Rd} =$	239,70	kNm	RSA
Minimum design existing moment	$M_{Ed,min} =$	64,94	kNm	Combo 404 non CD
Ratio of end moments in beam	$\psi = M_{Ed,min} / M_{pl,Rd} =$	0,27	-	EC3-1, 6.3.5.3 (6.68)
Stable beam length	$L_{stable} =$	1,86	m	
LTB length (distance between lateral supports)	$L_{LTB} =$	5,60	m	Assumption
Checking if L_{stable} can be determined according to (6.68)	$h / t_f \leq 40\epsilon$	TRUE		EC8-1, 4.4.2.3(4) (4.29)
Verification of stable length of segment	$L_{stable} \geq L_{LTB}$	FALSE		

Figure F.9: Beam segment lateral stability check

F.2.4 SCWB concept

Parameter		Beams IPE 360	Columns HEB400	Unit	Reference
Minimum moment resistance of the beam	$\Sigma M_{Rb} =$	479,4	N/A	kNm	EC3-1, 6.2.5 (6.13)
Minimum moment resistance of the column	$\Sigma M_{Rc} =$	N/A	2980,8	kNm	
Checking SCWB criteria	$\Sigma M_{Rc} \geq 1,3 \Sigma M_{Rb}$	21%			EC8-1, 4.4.2.3(4) (4.29)

Figure F.10: SCWB check

F.2.5 Column plastic shear capacity

Parameter		Columns HEB400	Unit	Reference
Plastic shear resistance	$V_{pl,Rd,c} =$	1775,60	kN	EC3-1, 6.2.6 (6.18)
Design shear	$V_{Ed,c} =$	130,26	kN	Combo 705 CD
Checking if the column shear force will reduce its plastic loadbearing capacity	$V_{Ed,c} / V_{pl,Rd,c} \leq 0,5$	7%		EC8-1, 6.6.3(4) (6.7)

Figure F.11: Column plastic shear capacity check

F.2.6 Panel zone

Parameter	Beams IPE 360	Columns HEB400	Unit	Reference
Beam web free height (excl. flange)	$z; b_s =$	334,6	N/A	mm
Column web free height (excl. flange)	$h_w; d_s =$	N/A	352	mm
Shear force in BOT column	$V_{c1,Ed} =$	N/A	0	kN
Shear force in TOP column	$V_{c2,Ed} =$	N/A	0	kN
Plastic moment resistance in R beam	$M_{b1,pl,Rd} =$	239,7	N/A	kNm
Plastic moment resistance in L beam	$M_{b2,pl,Rd} =$	-239,7	N/A	kNm
Shear force in panel zone	$V_{wp,Ed} = (M_{b1,pl,Rd} - M_{b2,pl,Rd})/z - (V_{c1,Ed} - V_{c2,Ed})/2 =$	1380,36	kN	EC3-1-8, 6.2.5 (5.3)
Plastic shear resistance in panel zone excl. transverse stiffeners contribution	$V_{wp,Rd} = (0,9 f_{yw,c} A_v) / (\sqrt{3} \gamma_{M0}) =$	1598,04	kN	EC3-1-8, 6.2.6.1 (6.8)
Conservative shear buckling factor up to grade S460	$\eta =$	1,20	-	EC3-1-5, 5.1(2)
Buckling resistance of the panel zone excl. flange contribution and using reduction factor from general conservative buckling mode (η) instead of the specific one for the web (χ_w)	$V_{wb,Rd} = (\eta f_{yw,c} h_w t_w) / (\sqrt{3} \gamma_{M1}) =$	1442,33	kN	EC3-1-5, 5.2 (5.2)
Check to see if formulas 6.2.6.1(2) to (14) can be used	$d/t_w \leq 69\epsilon$	TRUE		EC8-1, 6.2.6.1(1)
Recommended panel thickness	$t_w > (b_s + d_s) / 90$	TRUE		Design practice
Checking panel shear resistance in plastic stage	$V_{wp,Ed} / V_{wp,Rd} \leq 1,0$	86%		EC8-1, 6.6.3(6) (6.8)
Checking panel shear buckling	$V_{wp,Ed} < V_{wb,Rd}$	96%		EC8-1, 6.6.3(7) (6.9)

Figure F.12: Panel zone check

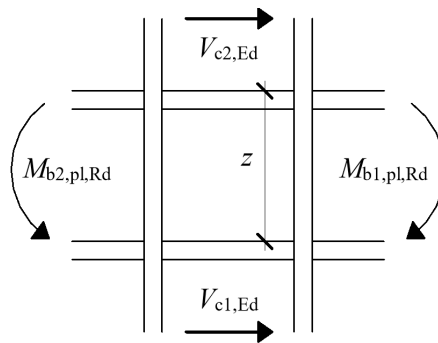


Figure F.13: Determining the shear force in the panel zone $V_{wp,Ed}$

F.2.7 Column verification

Parameter	Beams IPE 360	Unit	Reference
Maximum moment in the beam in a seismic situation	$M_{Ed,max,b} =$	121,26	kNm
System overstrength	$\min(\Omega_i) = M_{pl,Rd,b} / M_{Ed,max,b} =$	1,98	-
Factor for multiplying internal seismic forces on columns	$1,1 \gamma_{ov} \min(\Omega_i) =$	2,72	EC8-1, 6.6.3(1) (6.6)

Figure F.14: Column verification factor

G Thesis contract

This chapter contains the Thesis Contract between all involved parties and description of the topic.



Specialekontrakt – Institut for Byggeri, by og miljø

Application for Thesis Contract – Department of the Built Environment

Kontrakt (Kandidat eller Diplomingeniør)/ Type of thesis (Master or Bachelor of Engineering):

Master of Science

Studerende/Student

Navn/Name: **Boris Borisov Minkov**

Studienummer/Student number: **20200889**

Email: **bminko20@student.aau.dk**

Uddannelse/Programme: **MSc Civil and Structural Engineering**

Vejledere/Project Supervisors

Navn/Name: **Lars Damkilde**

Underskrift/Signature:

Navn/Name:

Underskrift/Signature:

Virksomhedskontakt (hvis relevant) /Company Contact Person (if relevant).

Navn/Name: **Tzvetan Georgiev**

Underskrift/Signature:

Email: **Tzv.Georgiev@irconltd.com**

Speciale/afgangsprojekt/Thesis/Project

Titel på speciale eller afgangprojekt/Project Title: **Choice of actuators for a new RWSF facility**

Startdato/Starting: **01.02.2022**

Deadline: **09.06.2022**

ECTS: **30**



Projektbeskrivelse/Project Description:

Introduction

The RWSF (Reaction Wall – Strong floor) is an experimental facility for performing quasi-static tests of isolated lateral load resisting systems or entire structures. The main advantage of a RWSF is the avoidance of size reduction since specimen dimension can in general be larger than on a shaking table. This averts scaling errors which are very problematic when simulating an earthquake.

Such a facility is to be built in Bulgaria with an aim of providing a solid experimental base to be used for research and education purposes. It will not only create development opportunities for future and present Bulgarian Structural Engineers but will also play a major role for the advancement of Seismic Engineering in the Balkan Peninsula – one of Europe's most active regions in geodynamical aspect.

Process

The first step is to study seismic testing facilities (shake table, reaction wall etc.) and gather inspiration and knowledge. Example of such is ELSA's (European Laboratory for Structural Assessment) which is the largest of its kind in EU. The advantages and disadvantages of each facility type is to be investigated.

A sophisticated feasibility study is needed to determine the suitable actuator(s). This is done by investigating suitable types of experimental set ups (structures) that reflect best the size and material of future test specimens. For this purpose, appropriate structures are aligned with the Company Contact Person and at least two lateral load resisting systems (ex. concentrically braced steel frame and a moment resisting steel frame) are investigated. The Modal Response Spectrum Linear Analysis (EC8) is used to determine the size of their structural members.

Once the suitable test specimens (structures) have been designed, the non-linear Pushover analysis is used to simulate a quasi-static RWSF experiment and obtain their capacity curve. The results (deformation, base shear, etc.) are investigated and compared so that the necessary actuator specifications (stroke length, capacity etc.) can be concluded. Moreover, reactions are provided for the future elastic design of the RWSF facility.

Delimitation

Since a RWSF facility is not available for an experiment during the Thesis period, only numerical and analytical investigations are undertaken. The resulted FE model can in future be experimentally verified and recalibrated if the numerical and experimental results at the actuators differ.

Plan for vejledning og laboratoriarbejde/Plan for Thesis Supervision and Lab Work:

1. Supervision with Company Contact Person: weekly basis
2. Supervision with Project Supervisor: monthly basis

Godkendt af Studieleder/Approved by Head of Studies

Dato/Date

Underskrift/Signature

Lene Faber Ussing